

Alma Mater Studiorum - Università di Bologna

DOTTORATO DI RICERCA IN
GEOFISICA

Ciclo 34

Settore Concorsuale: 02/C1 - ASTRONOMIA, ASTROFISICA, FISICA DELLA TERRA E DEI PIANETI

Settore Scientifico Disciplinare: FIS/06 - FISICA PER IL SISTEMA TERRA E IL MEZZO CIRCUMTERRESTRE

CLIMATE VARIABILITY IN AN EARTH SYSTEM MODEL OF INTERMEDIATE COMPLEXITY: FROM INTERANNUAL TO CENTENNIAL TIMESCALES

Presentata da: Michela Angeloni

Coordinatore Dottorato

Nadia Pinardi

Supervisore

Jost Diedrich Graf Von Hardenberg

Co-supervisore

Maria Elina Belardinelli

Esame finale anno 2022

Abstract

This thesis explores the climate mean state and climate variability reproduced by atmosphere-ocean coupled configurations of the Planet Simulator (PlaSim), an Earth-system Model of Intermediate Complexity (EMIC). In particular, the sensitivity to variations in oceanic parameters is explored in three atmosphere-ocean coupled configurations: using a simple mixed-layer (ML) ocean at two horizontal resolutions (T21 - 600 km and T42 - 300 km) or a more complex dynamical ocean, the Large Scale Geostrophic (LSG) ocean, at T21 atmospheric horizontal resolution. Sensitivity experiments allow to identify a reference oceanic diffusion coefficient in the ML ocean and a vertical oceanic diffusion profile in LSG, which ensure a simulated climate in good agreement with the present climate. For each model configuration, the Equilibrium Climate Sensitivity (ECS) is estimated from simulations with an increased CO₂ concentration compared to pre-industrial simulations. The resulting ECS values are higher than values estimated in other EMICs or models of the Coupled Intercomparison Project Phase 5 (CMIP5) and Phase 6 (CMIP6), especially in the PlaSim-ML configurations. An important role is found to be played by the sea ice area in pre-industrial and future simulations but also by the details of oceanic heat transport parameterization. The climate variability of the model is then explored on different timescales, from the centennial to the interannual one. In the first case, the mechanism that in PlaSim-LSG generates regular oscillations of the Atlantic Meridional Overturning Circulation (AMOC), which have a multicentennial period and represent one of the three regimes that can be assumed by the AMOC in the model, is investigated. Analysis of the oscillations has suggested that the mechanism is based on a feedback due to changes in Arctic sea ice cover and consequent changes in salinity in that area, which after some decades spread in the North Atlantic and affect the AMOC. Interannual variability is explored instead by analysing the extra-tropical atmospheric response, with a focus on the North Atlantic sector, to symmetric sea surface temperature forcings simulating strong El Niño and La Niña events. While the response to La Niña is very weak and not statistically significant, the model realistically reproduces the pattern of sea level pressure and geopotential height characteristic of El Niño, although with weaker amplitude than other more complex models. The PlaSim EMIC, although it has some limitations associated with the simplicity of some of its parameterizations, has the great advantage of reduced computational times and necessary resources with respect to Global Climate Models (GCMs) and Earth System Models (ESMs). By showing the capability of the model to represent a realistic climate mean state with appropriately tuned oceanic parameters and by contributing to our understanding of the mechanisms affecting its climate sensitivity and

its variability at different timescales, this study provides a basis for using this model in a wide range of climate study applications, in the spirit of the EMICs.

Contents

List of Figures	5
List of Tables	11
Introduction	13
1 Earth-system Models of Intermediate Complexity	17
2 The Planet Simulator EMIC	23
2.1 The Planet Simulator model with a mixed-layer ocean	23
2.2 The Large Scale Geostrophic ocean circulation model	24
2.3 Coupling the PlaSim model with LSG	25
3 Tuning of oceanic parameters	27
3.1 Mixed-layer ocean horizontal diffusion	29
3.2 Large Scale Geostrophic ocean vertical diffusion	30
3.3 Exploration of atmospheric and oceanic parameters to reduce the Southern Ocean bias	32
3.3.1 Oceanic horizontal diffusion coefficient	33
3.3.2 Sea ice albedo parameter	35
3.3.3 Cloud albedo parameter	36
3.3.4 Prescribed cloud properties	38
3.4 Concluding remarks	39
4 Model climate	41
4.1 Poleward heat transport	41
4.2 Simulated climate	42
4.3 Energy balance	45
4.4 Historical runs and future projections	46
5 Equilibrium climate sensitivity	49
5.1 The Gregory method	49
5.2 The role of sea ice and ocean heat transport	52
5.3 Concluding remarks	56

6	Atlantic MOC variability	57
6.1	AMOC regimes in PlaSim-LSG	57
6.2	AMOC oscillations in paleoclimate data and model simulations	58
6.3	AMOC oscillations in PlaSim-LSG	60
6.4	Concluding remarks	68
7	The ENSO teleconnection to the North Atlantic	71
7.1	The leading mode of variability in the North Atlantic: the NAO	71
7.2	The leading mode of variability of the tropical ocean-atmosphere system: the ENSO phenomenon	76
7.3	The impact of ENSO on the Northern Hemisphere	77
7.4	Late-winter North Atlantic response to ENSO in PlaSim . . .	80
7.5	Concluding remarks	87
	Conclusions	89
	Bibliography	95

List of Figures

1	Histogram of the number of simulated years with PlaSim during the PhD period.	16
1.1	Definition of the models spectrum in terms of a 3-dimensional space: integration, i.e. number of components of the Earth system explicitly described in the model, number of processes explicitly described, and detail of description of processes (Claussen et al., 2002).	17
1.2	Structure of an EMIC (Claussen et al., 2000).	19
1.3	Main features of the EMICs assessed in the IPCC AR5 (IPCC, 2013), including components and complexity of the models (higher complexity is indicated by darker colour shading). . .	19
1.4	Time series of the anomalies in annual and global mean surface temperature for different observations (thick black lines), single EMIC simulations (thin lines) and multi-model mean (thick red line). All anomalies are differences from the 1961–1990 (yellow shading) time-mean of each individual time series (IPCC, 2013).	21
3.1	Zonal mean of near-surface air temperature which is obtained using the default (red lines) and the tuned (black lines) horizontal diffusion coefficients in the ML ocean, with the T21 (left) and T42 resolution (right). The ERA-Interim values are the black dashed lines. Anomalies with respect to ERA-Interim are shown in the inner boxes	29
3.2	Vertical diffusion profiles in PlaSim-LSG and maximum of the AMOC between 46-66°N and below 700 m (top). Zonal mean of near-surface air temperature and sea ice cover (anomalies with respect to ERA-Interim reanalysis and HadISST observations are in the inner boxes) for different vertical diffusion profiles in the LSG ocean. Reanalysis and observations are represented by black dashed lines.	31

3.3	Horizontal diffusion profiles in PlaSim-LSG and maximum of the AMOC between 46-66°N and below 700 m (top). Zonal mean of near-surface air temperature and sea ice cover (anomalies with respect to ERA-Interim reanalysis and HadISST observations are in the inner boxes) for different horizontal diffusion profiles in the LSG ocean. Reanalysis and observations are represented by black dashed lines.	34
3.4	Anomalies of shortwave (top) and longwave (bottom) components of radiative flux at the surface, computed with respect to the CERES EBAF dataset.	35
3.5	Relationship between global mean of near-surface air temperature and <i>albsea</i> (albedo for free ocean) in PlaSim-LSG (left). Zonal mean of near-surface air temperature for different values of <i>albsea</i>	36
3.6	Relationship between global mean of near-surface air temperature and <i>tswr1</i> (tuning of cloud albedo in spectral range 1) in PlaSim-LSG (left). Zonal mean of near-surface air temperature for different values of <i>tswr1</i>	37
3.7	Distribution of low (levels 7-10), medium (levels 5-6) and high (levels 1-4) clouds in PlaSim-LSG.	38
3.8	Zonal mean of near-surface air temperature for different parameterization of the effect of clouds on shortwave radiation.	38
4.1	Zonally-averaged annual mean oceanic and atmospheric heat transport as a function of latitude for reference (dashed lines) and tuned (colored solid lines) coupled configurations of PlaSim. The reference configuration of PlaSim-ML is the original version with default horizontal diffusion coefficient, the reference configuration of PlaSim-LSG has the vertical diffusion profile suggested by Bryan and Lewis (1979). The ERA-Interim values are the black lines.	42
4.2	Difference between simulated and observed near-surface air temperature, sea surface temperature, sea ice cover, precipitation and TOA net radiation for the three selected configurations of the model: PlaSim with the ML ocean and T21 (left), PlaSim with the ML ocean and T42 (middle), PlaSim with the LSG ocean and T21 (right).	44

4.3	Near-surface air temperature anomalies relative to the 1961-1990 mean, obtained using for each of the three PlaSim configurations two different Representative Concentration Pathways, RCP 4.5 (solid line) and RCP 8.5 (dotted line). The black line represents the HadCRUT observational dataset (left). Global mean annual temperature anomalies computed with respect to the period 1961-1990, obtained from experiments using CMIP5 models for four different possible CO ₂ concentration scenarios, including RCP 4.5 and RCP 8.5 (right; image processed by Ed Hawkins, University of Reading, https://www.climate-lab-book.ac.uk).	47
5.1	Relationships between ΔF , the change in net TOA radiative flux, and ΔT , the change in global mean near-surface air temperature, after an instantaneous doubling and quadrupling of CO ₂ , using dynamic or prescribed sea ice. Data points are global and annual means simulated with PlaSim-ML T21, PlaSim-ML T42 and PlaSim-LSG T21. Lines represent ordinary least squares regression fits.	50
5.2	Radiative forcing R , climate feedback λ and equilibrium climate sensitivity ECS (in Wm ⁻² , Wm ⁻² K ⁻¹ and K, respectively) values for PlaSim-ML (T21 and T42) and for PlaSim-LSG (T21). Boxplots show the corresponding ranges of values found in CMIP5 models (Andrews et al., 2012) and estimates of ECS values from EMICs (Pfister and Stocker, 2017) and CMIP6 models (Zelinka et al., 2020).	51
5.3	Sea ice radiative forcing (see Eq. 5.2) as a function of the relative sea ice area (prescribed-ice area minus dynamic-ice area, see Table 5.1). Values are obtained by estimating the radiative forcing that should be provided to prescribed-ice experiments in order to undergo the same global mean near-surface air temperature change as in dynamic-ice experiments.	54
6.1	Different AMOC regimes in the PlaSim-LSG configuration as a function of the vertical oceanic diffusion coefficient A_v and of the atmospheric CO ₂ concentration. Filled circles indicate the presence of AMOC oscillations.	58
6.2	AMOC oscillations obtained with the PlaSim-LSG model under a certain range of parameters.	60
6.3	Time series of near-surface air temperature in the Arctic (60-90°N) and Antarctic (60-90°S) regions. The black lines represent a moving mean calculated over a sliding window of length 31 years and superimposed to the original output in grey.	61

6.4	Zonally-averaged salinity anomalies (in psu) of the Atlantic and Arctic basin for different phases of AMOC oscillations, computed as the deviation from the time mean between years 1250 and 3971 of the simulation. The stippling indicates areas where more than 80% of the oscillations agree on the sign of the change.	62
6.5	Surface salinity (in psu), sea ice cover and evaporation (in mm/day) climatology and anomalies for different phases of AMOC oscillations. The stippling indicates areas where more than 80% of the oscillations agree on the sign of the change.	64
6.6	Maximum AMOC computed between 46-66°N and below 700 m (grey line) and moving average of AMOC over a sliding window of 31 years (black line). Time versus latitude Hovmöller diagram of sea ice cover, salinity (in psu) and potential temperature anomaly (in K), averaged over the longitudinal band corresponding to the Atlantic Ocean and over the first 1000 m of depth.	65
6.7	Regression on AMOC of surface salinity anomaly (in psu), sea ice volume (in m) and cover, evaporation (in mm/day) and near-surface air temperature (K). The lag is positive when the AMOC leads.	67
6.8	Regression on AMOC low frequency first component of the top 150 m salinity (colors, in psu) at lag 0 and lagged regression of Arctic sea ice area and volume in IPSL (Jiang et al., 2021).	70
7.1	Maps in JFM using ERA-20CR (1900-2010): sea level pressure climatology and standard deviation (in hPa), sea level pressure regressed onto the NAO index (in hPa).	72
7.2	Sea level pressure climatology (in hPa) in JFM using T21 and T42 resolution, respectively (top panels). Sea level pressure difference in JFM with respect to ERA-20CR (1900-2010) (bottom panels). Stippling indicate statistically significant areas at 95% confidence level.	73
7.3	Sea level pressure standard deviation (in hPa) in JFM using T21 and T42 resolution, respectively (top panels). Difference of sea level pressure standard deviation in JFM with respect to ERA-20CR (1900-2010) (bottom panels). Stippling indicate statistically significant areas at 95% confidence level.	74
7.4	Sea level pressure regressed onto the NAO index (in hPa) in JFM in PlaSim T21 and PlaSim T42.	75
7.5	Schematic diagram showing the atmospheric and oceanic conditions along the equator in (a) La Niña, (b) normal, and (c) El Niño conditions (Hartmann, 2016).	76

7.6	Composite anomaly maps of (top) surface pressure, (middle) temperature, and (bottom) rainfall based on station data for twenty-six ENSO warm events from 1880 to 1988 (Brönnimann, 2007).	79
7.7	Results of CTL simulations with PlaSim. Maps of zonal wind (in ms^{-1}) at 200 hPa in JFM using T21 and T42 resolutions and the difference between them (top panels). Velocity potential (in $10^6 \text{ m}^2\text{s}^{-1}$) and divergent wind (in ms^{-1}) at 200 hPa (middle panels). Precipitation (in mm day^{-1} ; bottom panels). Stippling indicate statistically significant areas at 95% confidence level.	80
7.8	SST anomalies in JFM prescribed in EN and LN simulations with PlaSim.	81
7.9	Ensemble-mean precipitation (shading) and SST at 27°C (yellow line) for CTL (top), EN (middle) and LN (bottom) experiments using T21 and T42 resolutions.	82
7.10	Z200 anomalies (in m, contour lines) in EN simulations with respect to CTL simulations for different values of SST anomalies (in K, shading). The interval of contours is 20 m and non-significant values are plotted with grey contours.	83
7.11	Z200 anomalies (in m, contour lines) in LN simulations with respect to CTL simulations for different values of SST anomalies (in K, shading). The interval of contours is 20 m and non-significant values are plotted with grey contours.	84
7.12	Ensemble-mean 200-hPa Tropical Rossby Wave Source (shading), divergent wind (arrows) and Z200 (contours; interval = 30 m) anomalies for EN and LN in JFM in the EC-Earth climate model (Mezzina et al., 2021).	85
7.13	Anomalies for EN simulations with respect to CTL simulations. (Top panels) SST (in K, shading) and SLP (in hPa, contours with interval of 0.5 hPa) anomalies in JFM for T21 (left) and T42 (right) resolution. (Bottom panels) precipitation (in mm day^{-1} , shading) and geopotential height at 200 hPa (in m, contours with interval of 20 m. Stippling indicate statistically significant areas at 95% confidence level for shading, non-significant values for contours are plotted in grey.	86
7.14	Standard deviation of SLP in JFM computed over three different regions corresponding to Aleutian Low, Azores High and Icelandic Low. PlaSim CTL simulations (T21 and T42 resolution) are compared with reanalysis datasets: NOAA-20CR, ERA-20CR, ERA-Interim, NCEP/NCAR.	87

List of Tables

3.1	Vertical diffusion parameters used in PlaSim-LSG simulations. Each row indicates parameters which describe a different A_v profile, corresponding respectively to the red, yellow, green and black lines shown in Fig. 3.2.	30
3.2	Horizontal diffusion parameters used in PlaSim-LSG simulations. Each row indicates parameters which describe a different A_h profile, corresponding respectively to the blue, black, red, yellow, purple and green lines shown in Fig. 3.3.	33
4.1	Observational and reanalysis datasets used in this paper.	43
4.2	TOA and surface energy fluxes in Wm^{-2} . Latent heat flux also includes the snow contribution. Precipitation-evaporation (P-E) imbalance is reported as latent heat.	45
5.1	Key values derived from simulations performed using the tuned configurations of PlaSim (defined in Chapter 3) and four different CO_2 level increase factor: climate feedback parameter λ_d , radiative forcing R_d , equilibrium temperature ΔT_d^{eq} , pre-industrial (I_d^{PI}) and final (I_d) sea ice area at equilibrium for the dynamic-ice simulations; climate feedback parameter λ_p , radiative forcing R_p , equilibrium temperature ΔT_p^{eq} and sea ice area for the prescribed-ice simulations; sea ice feedback parameter λ_i , computed as the difference between λ_d and λ_p . The reported uncertainties are standard deviations.	50

Introduction

The climate system responds to natural and anthropogenic forcing in a complex way, because the different components of the climate system interact with each other in a non-linear way and through feedback mechanisms. The natural and anthropogenic forcing is responsible for climate variability, which consists of variations in the mean state and other statistics of the climate on spatial and temporal scales beyond that of weather events. When changes persist for an extended period, typically decades or longer, the phenomenon of climate change is considered. The importance of climate change has increased with the realization that human activities can change the climate and they are in turn affected by it. The Fifth Assessment Report (AR5) of Intergovernmental Panel on Climate Change (IPCC, 2013) asserts that the warming of the climate system is unequivocal: the atmosphere and ocean have warmed, the amounts of snow and ice have diminished, the sea level has risen, the concentration of greenhouse gases have increased. Furthermore, a large fraction of anthropogenic climate change resulting from CO₂ emissions is irreversible on long timescales. The rate and magnitude of global climate change are investigated by examining the Earth's energy budget, temperature change and climate feedbacks. The planetary energy budget is fundamental to understand changes of the climate system, because natural and anthropogenic substances and processes that alter the energy budget are drivers of climate change. The variation in energy fluxes is defined as radiative forcing: it indicates an uptake of energy by the climate system in the last centuries, mainly due to an increase of the atmospheric concentration of CO₂. On the other hand, one of the main measures of temperature change is the equilibrium climate sensitivity (ECS), defined as the change in global mean surface temperature at equilibrium that is caused by a doubling of the atmospheric CO₂ concentration. Despite not directly predicting actual warming because the climate system has not reached an equilibrium state, ECS has become a fundamental number for quantifying global warming.

Understanding the physical laws and processes governing the climate system and climate change results from combining observations and model simulations. Numerical global climate models differ in the number of spatial dimensions, in the level of explicit representation of physical, chemical and biological processes and in the number of empirical parameterizations,

constituting a hierarchy of models. Climate research has led to a notable improvement of numerical models, that now reproduce observed temperature patterns and trends, including the rapid warming since the mid-20th century (IPCC, 2013). In the middle of this hierarchy, we find Earth-system Models of Intermediate Complexity (EMICs), which are global models including most of the components and processes of the Earth system, in a simplified and parameterized form. The main advantages of these models with respect to the more complex Global Climate Models (GCMs) and Earth System Models (ESMs) are a low computational time due to the relatively coarse resolution and simpler parameterizations, allowing sometimes a better understanding of the mechanisms at work.

The Planet Simulator (PlaSim) is an EMIC developed at the University of Hamburg (Lunkeit et al., 2011; Fraedrich et al., 2005) which had several applications in the study of the climate system in the last decades. For example, it has been used to explore past conditions of the Earth such as the snowball Earth (Micheels and Montenari, 2008) or the Permian climate (Roscher et al., 2011), to analyse specific processes of the climate system using an Aquaplanet configuration (Dahms et al., 2011; Hertwig et al., 2015), to investigate the Earth’s global energy budget (Fraedrich and Lunkeit, 2008) or exoplanets (Kilic et al., 2017). The oceanic component of the model can be represented by a simple mixed-layer (ML) model (Lunkeit et al., 2011) or by a more complex, fully 3D dynamical oceanic model, the Large Scale Geostrophic (LSG) model (Maier-Reimer et al., 1993). The PlaSim-LSG coupled model has mainly been used in Aquaplanet or paleoclimatic configurations (Dahms et al., 2012; Hertwig et al., 2015; Andres and Tarasov, 2019). PlaSim has been developed to be run mainly at two different horizontal spectral resolutions, T21 and T42, corresponding to about 600 km and 300 km. Despite several applications, the guidelines currently available in the literature regarding the use of some PlaSim configurations are incomplete. A tuning exercise for the atmospheric component has been recently performed (Lyu et al., 2018), but some studies involving the tuning of oceanic parameters, the assessment of the model climatology and energy balance, and the estimate of its equilibrium climate sensitivity (ECS) are still missing and they could be of considerable importance for future applications in the framework of climate variability and climate change. For example, the model in the configuration with the ML ocean allows to activate, as an alternative to the well-explored flux correction, a horizontal diffusion in the ocean, which determines the heat transport from the equator to the poles. However, the default value for this parameter is not appropriate to ensure a correct temperature distribution in the model, and therefore a tuning of this oceanic parameter that can be a reference for future developments has been performed in this thesis. Also the PlaSim-LSG configuration has been little explored in the literature and the default value for vertical oceanic diffusion coefficient leads to a collapse of the Atlantic Meridional Overturning Circulation (AMOC) after

about 150 years of simulation. Again, I have analysed the role of this oceanic parameter and determined an optimal value to obtain a realistic climate. All these observations indicate the need to document the role of some model parameters and to highlight its strengths and weaknesses, which is an essential information for anyone who plans to use PlaSim as a research tool.

The aim of this PhD thesis is to provide an overall view of the characteristics of the Planet Simulator in three different configurations, PlaSim-ML T21, PlaSim-ML T42 and PlaSim-LSG T21, to give a solid basis for further developments of the model and its future applications in the study of the Earth's climate system. This PhD thesis profits from the results which I obtained during my Master's thesis, in which I performed a preliminary model tuning and partially explored its ECS. This thesis is organized as follows. Chapter 1 introduces EMICs within the models spectrum and illustrates their numerous applications. Chapter 2 describes the different components of PlaSim, the characteristics of the two oceanic models and their coupling with the atmospheric component. Chapter 3 presents the tuning of oceanic parameters in the three model configurations explored. Furthermore, it discusses the role of some atmospheric features, such as albedo, ozone concentration and cloud cover. In Chapter 4 the simulated climate is evaluated, including an assessment of the energy balance of the model. After setting the oceanic parameters based on tuning, in Chapter 5 the model configurations are analysed from the point of view of the ECS, which is a measure of the model's response to an increase in anthropogenic forcing. The technique used here is the same as that applied to compute the ECS in models belonging to the Coupled Models Intercomparison Project (CMIP), the Gregory method (Gregory et al., 2004). The tuning of PlaSim-LSG T21 has revealed three different regimes of the AMOC. In particular, the regime characterized by an intermediate intensity presents multicentennial fluctuations of AMOC. These oscillations, which resemble Dansgaard-Oeschger events (although they show a different period; Dansgaard et al. (1993)), have been recently observed in other climate models (Peltier and Vettoretti, 2014; Jiang et al., 2021; Döscher et al., 2021) and are still under investigation. Chapter 6 analyses the AMOC oscillations in PlaSim and explores possible underlying mechanisms, highlighting similarities and differences with other AMOC fluctuations discussed in the literature. Finally, Chapter 7 has been developed in the framework of a collaboration with the Group of Meteorology at Universitat de Barcelona, where I carried out a period abroad required in my PhD programme. This chapter explores the extra-tropical response to ENSO teleconnection in Atmospheric Model Intercomparison Project (AMIP) experiments performed with PlaSim. The aim of this chapter is to present one of the several applications of the model and to determine its ability to reproduce a phenomenon which is generally explored in more complex climate models. One of the main advantages of PlaSim that I have experienced during the development of

this thesis work is its low computational cost: using the lower resolution (T21), the model is able to simulate one year in two and a half minutes on a single computing core. Thanks to this short computational time, it has been possible to carry out numerous simulations with PlaSim, most of them lasting hundreds or thousands of years, with the aim of investigating in detail as many model aspects as possible. This has allowed to simulate about 235000 model years during my PhD, with peaks corresponding to the tuning and the ECS experiments, as shown in Fig. 1. I also have contributed to some technical changes in the model code, aimed at improving several aspects related for example to the use of the namelists and the storage of outputs.

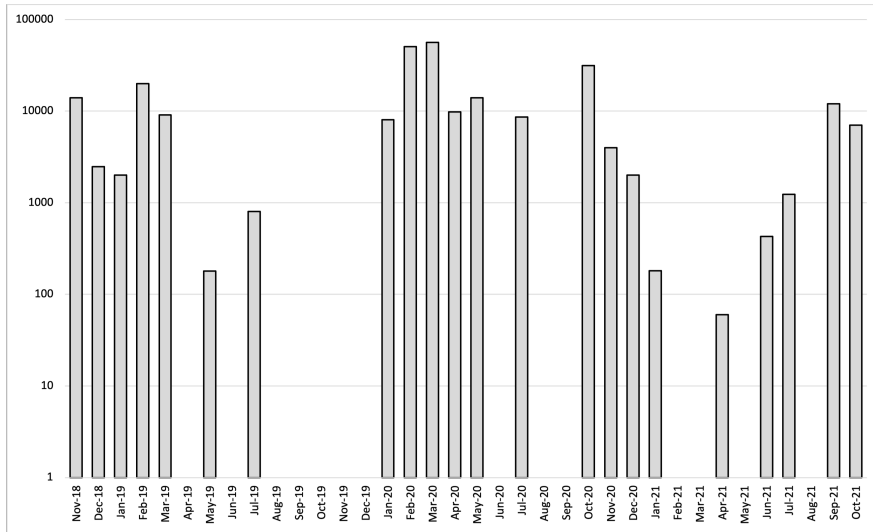


Figure 1: Histogram of the number of simulated years with PlaSim during the PhD period.

Chapter 1

Earth-system Models of Intermediate Complexity

The elements of the geosphere and biosphere have been first modelled separately and only later have been put together to form the first comprehensive coupled models, which include a description of the atmosphere and ocean, as well as biological and geochemical processes. The main limitations of these Earth System Models (ESMs) are the high computational cost and their complexity. On the other hand, the simplified conceptual models can be applied to a large number of climate studies and do not have the limit of computational cost, but they do not contain many processes and feedbacks that play a fundamental role in the climate system (Claussen et al., 2000). To bridge the gap between these two types of climate models, the first prototypes of Earth-system Models of Intermediate Complexity (EMICs) have been developed since the 1980s.

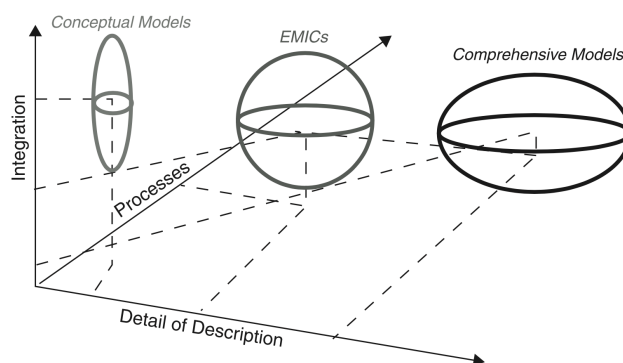


Figure 1.1: Definition of the models spectrum in terms of a 3-dimensional space: integration, i.e. number of components of the Earth system explicitly described in the model, number of processes explicitly described, and detail of description of processes (Claussen et al., 2002).

They describe the components of the Earth system and their interactions but in a reduced form compared to comprehensive models. The relative simplicity and the high number of parameterizations in the EMICs allow to simulate tens of thousands of years with low computational costs and with more realistic results than the conceptual models. But the computational advantage is not the only reason to use EMICs. Our knowledge of the climate system is still incomplete and often its description with mathematical equations is imperfect. In some fields of climate research, information about the components or processes under investigation may not be detailed enough to use a GCM. For example, paleoclimatic studies are often characterized by inadequate knowledge of the land-ice distribution and therefore the representation of associated feedbacks in a climate model is complicated. In these cases, the choice to use an EMIC, which allows a simplified representation of what we do not understand in detail, may be more appropriate than using a GCM. In addition, the removal of some of the ‘unnecessary’ complexities makes it possible to focus attention on the main mechanisms and understand them more easily, even at the cost of having a wrong representation of some feedbacks (Mcguffie and Henderson-Sellers, 2014). However, EMICs cannot be used as a substitute for comprehensive or conceptual models but rather to complement them, allowing to broaden the spectrum of climate system models, in which the different types of models are adapted to different aspects of the Earth system and together provide a complete view of it. Figure 1.1 from Claussen et al. (2002) shows the position of these three classes of models in a three-dimensional space consisting of the number of interacting components explicitly described (integration), the number of processes explicitly simulated and the detail of the description.

The development of an EMIC can originate from very different approaches, resulting in a great heterogeneity in terms of structure. All EMICs include an atmospheric module and an oceanic module, which includes a representation of sea ice. These components can be of different types and levels of complexity. Among the representations of the atmospheric component, we find statistical dynamical models, models based on the quasi-geostrophic approximation and models based on full primitive equations. The latter can be considered as coarse-resolution Global Climate Models (GCMs) (Weber, 2010). Oceanic modules can be fully three-dimensional oceanic circulation models or variations of the zonally-averaged formulation (Claussen et al., 2002). Sea ice modules are generally thermodynamic models, but may also include ice dynamics and advection. Some EMICs may also contain a module for vegetation dynamics, a module for inland ice sheets describing ice flow dynamics, or include marine and terrestrial carbon dynamics as well as atmospheric and oceanic chemistry. Their computational speed allows to analyse long-term feedbacks associated with some components of the climate system such as ice sheets and biogeochemical cycles.

The complexity of the EMICs is represented in Fig. 1.2 from Claussen et al. (2000), which presents an example of the structure of these models. Figure 1.3 shows the main features of EMICs assessed in the Fifth Assessment Report (AR5) of Intergovernmental Panel on Climate Change (IPCC, 2013), where the increasing complexity is indicated by colour shading (light to dark).

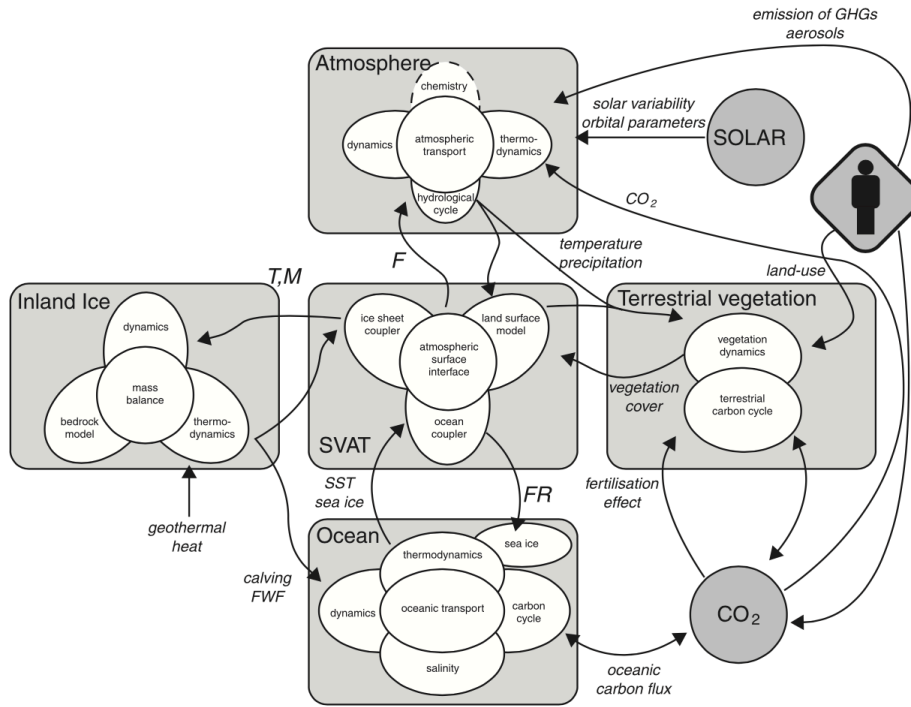


Figure 1.2: Structure of an EMIC (Claussen et al., 2000).

Model name	Country	Atmos	Ocean	Land Surface	Sea Ice	Coupling	Biosphere	Ice Sheets	Sediment & Weathering
Bern3D	Switzerland	Light	Light	Light	Light	Light	Light	Light	Light
CLIMBER2	Germany	Light	Light	Light	Light	Light	Light	Light	Light
CLIMBER3	Germany	Light	Light	Light	Light	Light	Light	Light	Light
DCESS	Denmark	Light	Light	Light	Light	Light	Light	Light	Light
FAMOUS	UK	Light	Light	Light	Light	Light	Light	Light	Light
GENIE	UK	Light	Light	Light	Light	Light	Light	Light	Light
IAP RAS CM	Russia	Light	Light	Light	Light	Light	Light	Light	Light
IGSM2	USA	Light	Light	Light	Light	Light	Light	Light	Light
LOVECLIM1.2	Netherlands	Light	Light	Light	Light	Light	Light	Light	Light
MESMO	USA	Light	Light	Light	Light	Light	Light	Light	Light
MIROC-lite	Japan	Light	Light	Light	Light	Light	Light	Light	Light
MIROC-lite-LCM	Japan	Light	Light	Light	Light	Light	Light	Light	Light
SPEEDO	Netherlands	Light	Light	Light	Light	Light	Light	Light	Light
UMD	USA	Light	Light	Light	Light	Light	Light	Light	Light
Uvic	Canada	Light	Light	Light	Light	Light	Light	Light	Light

Figure 1.3: Main features of the EMICs assessed in the IPCC AR5 (IPCC, 2013), including components and complexity of the models (higher complexity is indicated by darker colour shading).

EMICs have been developed because of the need to explore climatic variations on very different timescales, from those characterizing rapid events to the scales of glacial cycles and Milankovitch (hundreds of thousands of years). Over the years they have been applied to a wide range of climate analyses, such as the study of feedbacks in past, present and future scenarios (Eby et al., 2013), the understanding of the large-scale thermohaline circulation (Rahmstorf et al., 2005) or the future climate change due to the increased concentration of greenhouse gases (IPCC, 2013). Furthermore, EMICs are a fundamental tool for the analysis of tipping points, critical levels referred to a component or process of the Earth system and associated to abrupt and irreversible climate changes (Lenton et al., 2009). More recently, EMICs have been adapted to perform simulation of Martian (Segschneider et al., 2005) or exoplanetary atmospheres (Murante et al., 2020). Another advantage of these models is the possibility to perform large-ensemble simulations that are not feasible with more complex models, with the aim of examining the role of uncertainties in experiments (Weber, 2010). Intermediate complexity models can also be used to explore phase space or climate history in order to identify aspects of particular interest and provide guidance for more detailed analysis to be performed with more complex models. These include so-called “slice” simulations, in which generally the climate system is unrealistically assumed to be in equilibrium with external forcing (Claussen et al., 2002). Furthermore, some subcomponents are often developed and tested in the form of an EMIC and later included in a coupled GCM.

Some aspects of the EMICs have been explored and the results have been compared with historical data and other models within an intercomparison project undertaken in support of the IPCC AR5 (IPCC, 2013; Zickfeld et al., 2013; Eby et al., 2013). In general, although with some defects, the EMICs in this intercomparison well simulate the characteristics of the Earth system and the climate projections to 2300 are consistent with the results of GCMs. Figure 1.4 shows the ability of EMICs to simulate the global mean surface air temperature anomaly as a response to the 20th century forcings (IPCC, 2013). In addition, EMIC results for the equilibrium and transient response to CO₂ doubling are generally within the range of the corresponding results for model belonging to Phase 3 and Phase 5 of the CMIP. These analyses confirm that EMICs are well suited to play a complementary role to that of the other models in the spectrum, as they are very efficient in terms of running time and show a good qualitative and quantitative agreement with observations and other models. However, the large model spread suggests that continuous efforts are needed to improve the performance of these models, keeping in mind that the definition of intermediate complexity models will be continuously evolving due to fast increase in computer power.

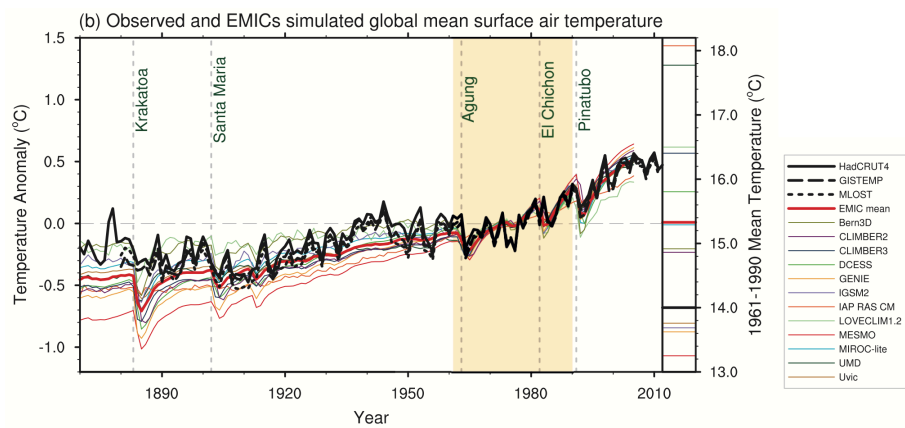


Figure 1.4: Time series of the anomalies in annual and global mean surface temperature for different observations (thick black lines), single EMIC simulations (thin lines) and multi-model mean (thick red line). All anomalies are differences from the 1961–1990 (yellow shading) time-mean of each individual time series (IPCC, 2013).

Chapter 2

The Planet Simulator EMIC

The assessment and the development of the PlaSim climate model is at the basis of this thesis work. In this chapter, the main characteristics of the model and its explored configurations are described.

2.1 The Planet Simulator model with a mixed-layer ocean

The dynamical core of PlaSim (Lunkeit et al., 2011; Fraedrich, 2012) is a simplified GCM, the Portable University Model of Atmosphere (PUMA), based on the moist primitive equations representing the conservation of momentum, mass and energy (Fraedrich et al., 2005) and using spectral methods to numerically solve them (Orszag, 1970; Eliassen et al., 1970). In the vertical, a σ -coordinate system and a finite-difference method to solve equations are used. The equations are time integrated with a leap-frog semi-implicit time stepping scheme with time filter (Hoskins and Simmons, 1975; Simmons et al., 1978; Robert, 1981; Asselin, 1972).

All subgrid unresolved processes, and their effects, are included by means of parameterizations: surface fluxes (Roeckner et al., 1992), oceanic vertical and horizontal diffusion (Roeckner et al., 1992), shortwave (Lacis and Hansen, 1974; Stephens, 1984) and longwave radiations (Sasamori, 1968; Stephens et al., 1984), moist processes (Kuo, 1974), clouds (Slingo and Slingo, 1991), dry convection are among the parameterized processes in this model.

The computation of physical processes is done on 5.6° and 2.8° longitude-latitude reduced Gaussian grids, corresponding to the two horizontal spectral resolution, T21 and T42. The model, as used in this thesis, has typically 10 atmospheric layers in the vertical up to 40 hPa and appropriate computational time steps are 45 minutes for T21 and 30 minutes for T42. Surface boundary condition data are provided from four different sources: the U.S. Geological Survey Land Surface Parameter dataset (Hagemann et al., 1999) and the GTOPO30 dataset (Tibaldi and Geleyn, 1981), MODIS satellite data (Rechid

et al., 2009) and the AMIP-II sea ice cover and sea surface temperature dataset (Taylor et al., 2000) for present day simulations of climate.

Sea surface temperatures can be simulated using a mixed-layer (ML) ocean model (Lunkeit et al., 2011) with constant thickness (the default value is 50 m). This ocean model consists of a prognostic equation for the oceanic temperature at each ocean grid point, which depends on the net atmospheric heat flux into the ocean. Ocean transport can be represented by the heat convergence at the base of the ML (a so-called Q-flux or flux correction) derived from climatology, but since the Q-flux approach may not be suitable for climate studies under conditions far from present day, I have not focused on this configuration in this thesis. Instead oceanic transports are parameterized by the addition of a horizontal diffusion term to the temperature equation:

$$\frac{\partial T_{ML}}{\partial t} = F_a + K_h \nabla^2 T_{ML} \quad (2.1)$$

where T_{ML} is the mixed-layer temperature, F_a describes the net energy exchanges with the atmosphere and K_h is a horizontal temperature diffusion coefficient (with a low starting default value of $1000 \text{ m}^2\text{s}^{-1}$, but I have tuned this value in my experiments).

The sea ice distribution can either be prescribed by climatology or simulated by a thermodynamic sea ice model based on the zero layer model by Semtner (1976), which computes the thickness of sea ice from the thermodynamic balance at the top and at the bottom of the sea ice layer. This model assumes a linear temperature gradient in the ice and prevents ice from storing heat. Sea ice is formed if the ocean temperature drops below the freezing point (set to 271.25 K) and is melted if the ocean temperature exceeds that value (Lunkeit et al., 2011).

2.2 The Large Scale Geostrophic ocean circulation model

The Large Scale Geostrophic (LSG) ocean circulation model (Maier-Reimer et al., 1993; Drijfhout et al., 1996) is based on the primitive equations in a three-dimensional system, including the momentum equation, the continuity equation describing conservation of water and salinity, the thermodynamic equation with salinity. Please see the Large Scale Geostrophic Model report, Maier-Reimer and Mikolajewicz (1992), for details. The model is based on the observation that, since for a large scale ocean circulation model developed for climate studies the characteristic spatial scales are large compared with the internal Rossby radius of deformation and the characteristic temporal scales are large compared with the periods of gravity modes and barotropic Rossby wave modes (Hasselmann, 1982), the nonlinear terms in the Navier-

Stokes equations can be neglected. Furthermore the vertical friction is neglected and the hydrostatic and the Boussinesq approximations are applied (Maier-Reimer and Mikolajewicz, 1992).

Turbulent motions are parameterized by means of a vertical oceanic diffusion coefficient, A_v , which is a rather simple function of the vertical coordinate, z (Bryan and Lewis, 1979):

$$A_v(z) = a^* + a_{\text{range}} \arctan[\lambda(z - z^*)] \quad (2.2)$$

where a^* is the vertical diffusion coefficient at a reference depth z^* , a_{range} defines the considered depth range from the surface to the bottom, and λ is the rate at which the vertical diffusion coefficient varies with depth near z^* .

A long time step of 10 days is permitted by the implicit time integration scheme. The model has two staggered $5^\circ \times 5^\circ$ horizontal grids (yielding an effective grid resolution of 3.5°), so that the variables of the model are defined on a semi-staggered E-type grid (Arakawa and Lamb, 1977). The components of horizontal velocity and the wind stress are defined on “vector points”, while potential temperature, salinity, heat and freshwater fluxes, sea-surface height, pressure and vertical velocity are defined on “scalar points”. The depth of the scalar points is usually defined as the maximum depth of the four surrounding vector points. The w-points (for the vertical component of the velocity) are vertically located between scalar points (Maier-Reimer and Mikolajewicz, 1992). By default, the number of oceanic vertical layers is 22, extending from the surface down to an oceanic depth of 6000 m. The Levitus-98 dataset (<https://www.esrl.noaa.gov/psd/data/gridded/data.nodc.woa98.html>) provides temperature and salinity initial conditions.

2.3 Coupling the PlaSim model with LSG

PlaSim and LSG are coupled through the surface fluxes of momentum, heat and fresh water. The atmospheric and oceanic grid interpolation ensures global conservation of energy and water (Fraedrich, 2012; Lorenz, 2006).

The uppermost layer of the ocean regulates heat fluxes. The ML depth of PlaSim $\Delta z_{ML}^{(Pl)}$ and the upper-layer thickness of LSG $\Delta z_{ul}^{(LSG)}$ are fixed to 50 m. Since the LSG free surface elevation (ζ) is only 1% of the LSG upper-layer thickness (50 m), ζ can be neglected.

At the beginning of each LSG time step $\Delta t^{(LSG)}$ (10 days), the average over $\Delta t^{(LSG)}$ of the PlaSim ML temperature is imposed as the temperature of the ocean upper layer $T_{ul}^{(LSG)}$,

$$T_{ul}^{(LSG)} = \overline{T_{ML}^{(Pl)}} = \left(\Delta t^{(LSG)}\right)^{-1} \int_{\Delta t^{(LSG)}} T_{ML}^{(Pl)} dt^{(Pl)} \quad (2.3)$$

A full ocean step is performed in which LSG calculates the ocean heat flux due to advective (advection, horizontal diffusion) and convective (vertical

transport, vertical diffusion, convective adjustments) processes. The resulting distribution of the upper layer temperature after $\Delta t^{(LSG)}$ determines the ocean heat flux, which is then given back to PlaSim. Equation. 2.3 is further modified to take into account small differences in the ML depth used by PlaSim and the upper layer of LSG and to correctly close the energy balance (see Lorenz (2006) for details).

Sea ice in LSG is prescribed as calculated in the ML module of PlaSim. When calculating over hundreds of years, sea ice grows unconstrained in some isolated grid-points in the Antarctic ocean. In order to avoid the consequent increase of salinity of open water in the upper layer of LSG, sea ice thickness is forced not to exceed 9 m.

Furthermore, the atmospheric wind stress and the freshwater flux (with a constant annual mean flux correction) are averaged over the coupling interval before they are transferred to the ocean.

Chapter 3

Tuning of oceanic parameters

In climate models, small-scale processes are introduced by means of parameterizations, which constitute an idealized and approximated representation of real processes. Each parameterization introduces equations and parameters, whose values are not always constrained by observations. The process by which these parameters are estimated with the aim of reducing the differences between the real world and the simulated world is called tuning. Tuning is often not properly documented when analysing the abilities of a climate model, because it is considered not interesting or a poorly justified error-compensation technique. However, it represents a fundamental part in climate modelling, as it consists of an optimization process that follows a scientific approach and can provide useful information on climate processes and model uncertainties. For example, if the value obtained by tuning for a given parameter is outside the acceptable range, model developers may consider changing the parameterization or developing a new one. One of the most comprehensive definitions of climate model tuning is that provided by Hourdin et al. (2017): “Once a model configuration is fixed, tuning consists of choosing parameter values in such a way that a certain measure of the deviation of the model output from selected observations or theory is minimized or reduced to an acceptable range”. Generally, the tuning process involves the parameterization of clouds, terrestrial albedo, ocean mixing, soil properties and vegetation. The tuning of these parameters is performed by choosing one or more model control variables, such as the global mean temperature or the net radiation balance at the top-of-atmosphere (TOA), and minimizing their difference with respect to observations. In addition to these trial-and-error approaches, which focus on few parameters at a time, there are more complex objective methods for tuning. Among these, the optimization of a cost function, which minimizes the difference between simulations and observations, or the use of a Bayesian approach, which explicitly quantifies the sources of uncertainty (Hourdin et al., 2017). The only currently available extensive tuning effort of PlaSim is represented by the article by Lyu et al. (2018),

who applied the adjoint method to calibrate the atmospheric component of the model in the configuration with prescribed sea surface temperatures (SSTs). Instead, in this thesis I have used two PlaSim configurations that contain a dynamic ocean, PlaSim-ML and PlaSim-LSG. As shown in the following paragraphs, the default values for some ocean parameters are not optimized to reproduce a realistic climate, and in the PlaSim-LSG model the AMOC collapses and climate at high latitudes is extremely cold. Therefore, a preliminary tuning of two oceanic parameters (one in the ML ocean and one in the LSG ocean), which I have found to be fundamental in reproducing the observed reference climate, has been performed. The tuning method used for PlaSim is quite simple and described below. I have performed a series of perennial simulations (with fixed atmospheric CO₂ concentration), which differ only in the value of the oceanic parameter under investigation, varied in an arbitrary range. The model takes some time to respond to the climate forcing with a change in temperature, until it reaches an equilibrium state. For each simulation, the zonal mean of near-surface air temperature at equilibrium has been compared with the same variable obtained from ERA-Interim reanalysis (Dee et al., 2011). Then the parameter value that minimizes the difference between the simulated and observed temperatures has been chosen. The choice of the CO₂ level to be used for the simulations has been based on the time period covered by the reanalysis dataset, which is 2005-2015. The CO₂ concentration measured in 2010 (central year) is about 389 ppm. The Earth’s climate is however in a transient state, where the CO₂ concentration is constantly increasing and the net imbalance at surface and at TOA is about 0.5 Wm^{-2} . If CO₂ concentration stopped increasing, the planet would warm up further, the emitted infrared radiation would increase and the net balance at TOA and surface would tend towards equilibrium, i.e. zero. Therefore, if we used the CO₂ value of 2010 for perennial simulations, the final global average temperature would be higher than that measured in that year. To compensate for this effect, I decided to use a lower CO₂ level which can be obtained from the following equation, linking the radiative forcing to the carbon dioxide concentration (see e.g. Myhre et al. (1998))

$$\Delta F = 5.35 \ln \left(\frac{C}{C_0} \right) \quad (3.1)$$

where ΔF is the radiative forcing change, C_0 is the carbon dioxide concentration in the reference year and C is the new concentration to be used for perennial climate simulations. The resulting value is about 354 ppm, which is fixed in the simulations. The tuning work of PlaSim-ML (at both resolutions) was carried out during my Master’s thesis (Angeloni, 2018) and the main results are summarized in Section 3.1. Instead, the tuning of PlaSim-LSG T21 in the version presented in this thesis was entirely carried out during my PhD.

3.1 Mixed-layer ocean horizontal diffusion

As described in Chapter 2, in the ML ocean it is possible to activate the horizontal oceanic diffusion and to modify the coefficient K_h (see Eq. 2.1) that parameterizes the oceanic motions. Using both resolutions, I have performed a 60 year long run with Plasim-ML, dynamic sea ice and horizontal oceanic diffusion, with the aim of testing the default value for the coefficient K_h , i.e. $1000 \text{ m}^2\text{s}^{-1}$ (Lunkeit et al., 2011). The model in this configuration reaches an equilibrium state after about 30 years of simulation. Figure 3.1 compares the zonal mean of near-surface air temperature for these two simulations (red lines) with the ERA-Interim reanalysis (dashed black line), showing that the simulated temperature is too cold (up to 20 K at high latitudes) and the climate of the model is unrealistic.

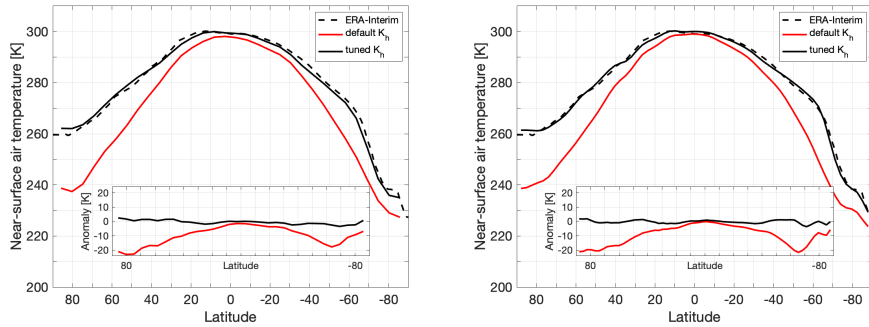


Figure 3.1: Zonal mean of near-surface air temperature which is obtained using the default (red lines) and the tuned (black lines) horizontal diffusion coefficients in the ML ocean, with the T21 (left) and T42 resolution (right). The ERA-Interim values are the black dashed lines. Anomalies with respect to ERA-Interim are shown in the inner boxes

In order to obtain a more realistic near-surface air temperature, I have performed several simulations (at both resolutions) each having a different horizontal diffusion coefficient K_h which was varied in the range from $10^3 \text{ m}^2\text{s}^{-1}$ to $10^6 \text{ m}^2\text{s}^{-1}$ (not shown). Choosing a single value of K_h for the entire globe leads to either a cold bias in the Northern Hemisphere (NH) or a warm bias in the Southern Hemisphere (SH). This suggested the use of two different diffusion coefficients, to be separately applied in the NH and SH: $K_h = 10^5 \text{ m}^2\text{s}^{-1}$ in the NH and $K_h = 10^4 \text{ m}^2\text{s}^{-1}$ in the SH when using T21; $K_h = 10^5 \text{ m}^2\text{s}^{-1}$ in the NH and $K_h = 3 \cdot 10^4 \text{ m}^2\text{s}^{-1}$ in the SH when using T42. This choice can be, to some extent, justified physically by the observed differences in meridional heat transport between the two hemispheres, particularly the strong North-South asymmetry observed in the Atlantic basin). Black solid lines in Fig. 3.1 show the results of these simulations, giving rise to a simulated zonally-averaged near-surface air temperature in very good

agreement with the reanalysis. The maximum difference between the model results and the ERA-Interim values is about 3 K.

3.2 Large Scale Geostrophic ocean vertical diffusion

The vertical oceanic diffusion coefficient in LSG ocean (see Eq. 2.2) is a parameterization of turbulent motions. In order to explore the role of this parameter, I have performed a series of 2000 year long runs with PlaSim-LSG T21, using dynamic sea ice and a fixed atmospheric CO₂ concentration. The model in this configuration reaches an equilibrium state after about 1000 years of simulation. The original version of PlaSim-LSG has by default a vertical diffusion profile with a surface value of $A_v = 0.3 \cdot 10^{-4} \text{ m}^2\text{s}^{-1}$ and a bottom value of $A_v = 2.6 \cdot 10^{-4} \text{ m}^2\text{s}^{-1}$ (see Table 3.1, run 1), which in my experiments leads to a complete shut-down of the maximum Atlantic Meridional Overturning Circulation (AMOC) (North Atlantic Deep Water) computed between 46-66°N and below 700 m (see red lines in top panels of Fig. 3.2). Using the default A_v , the simulated near-surface air temperature is too cold in the NH and too warm in the SH, with evident consequences on simulated sea ice cover (red lines in bottom panels of Fig. 3.2). I have explored other values suggested in the literature by performing other two simulations, each having a different vertical diffusion profile. For run 2, I have used the vertical diffusion coefficient profile suggested by Bryan and Lewis (1979) with a surface value of $A_v = 0.3 \cdot 10^{-4} \text{ m}^2\text{s}^{-1}$ and a bottom value of $A_v = 1.3 \cdot 10^{-4} \text{ m}^2\text{s}^{-1}$ (see Table 3.1 and yellow lines in Fig. 3.2). For run 3, I have used modified parameters which were found by Sciascia (2008) in ocean-only tuning experiments, with a surface value of $A_v = 0.8 \cdot 10^{-4} \text{ m}^2\text{s}^{-1}$ and a bottom value of $A_v = 1.3 \cdot 10^{-4} \text{ m}^2\text{s}^{-1}$ (Table 3.1 and green lines in Fig. 3.2).

Table 3.1: Vertical diffusion parameters used in PlaSim-LSG simulations. Each row indicates parameters which describe a different A_v profile, corresponding respectively to the red, yellow, green and black lines shown in Fig. 3.2.

A_v	$a^*[\text{m}^2\text{s}^{-1}]$	$a_{\text{range}}[\text{m}^2\text{s}^{-1}]$	$z^*[\text{m}]$	$\lambda[\text{m}^{-1}]$
1) default	$1.44 \cdot 10^{-4}$	$0.78 \cdot 10^{-4}$	2800	$3.6 \cdot 10^{-3}$
2) Bryan and Lewis (1979)	$0.7958 \cdot 10^{-4}$	$0.3345 \cdot 10^{-4}$	2500	$4.5 \cdot 10^{-3}$
3) Sciascia (2008)	$1.0479 \cdot 10^{-4}$	$0.1673 \cdot 10^{-4}$	2500	$4.5 \cdot 10^{-3}$
4) tuned	$0.8714 \cdot 10^{-4}$	$0.2843 \cdot 10^{-4}$	2500	$4.5 \cdot 10^{-3}$

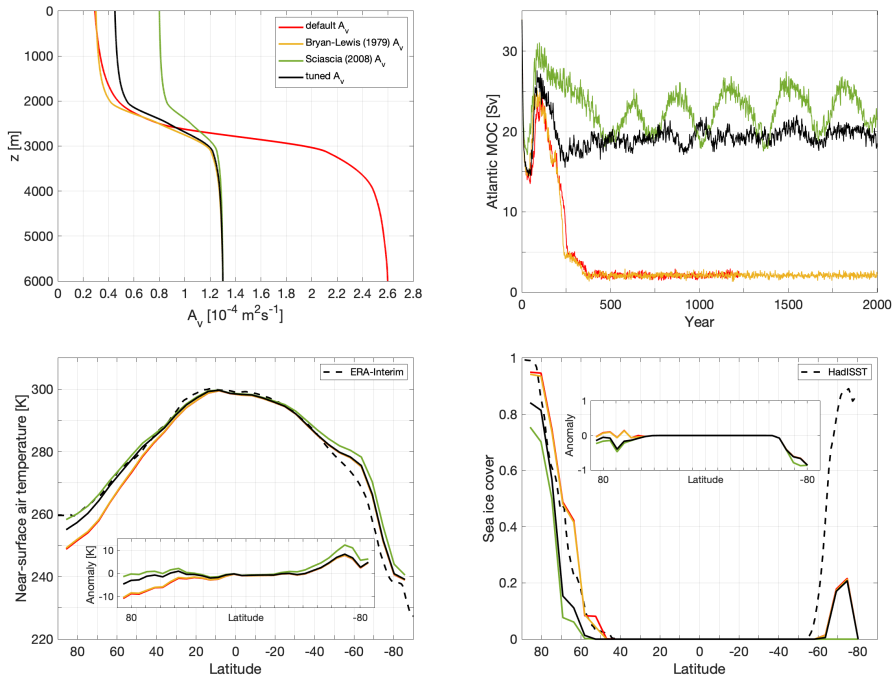


Figure 3.2: Vertical diffusion profiles in PlaSim-LSG and maximum of the AMOC between 46-66°N and below 700 m (top). Zonal mean of near-surface air temperature and sea ice cover (anomalies with respect to ERA-Interim reanalysis and HadISST observations are in the inner boxes) for different vertical diffusion profiles in the LSG ocean. Reanalysis and observations are represented by black dashed lines.

Also in this case I have extracted from the model outputs the time series of the maximum AMOC between 46-66°N and below 700 m. The thermohaline circulation collapses after about 300 years using the A_v profile 2 (Bryan and Lewis, 1979), while it is active using profile 3 (Sciascia, 2008), with values fluctuating from 17 to 27 Sv (these AMOC regimes will be discussed in Chapter 6). The corresponding zonal means of near-surface air temperature and sea ice cover (bottom panels in Fig. 3.2) show that the outputs of the model are not in good agreement with the ERA-Interim and HadISST datasets (black dashed line) using these two coefficients. In the NH, the simulated temperature is negatively biased with the profile 2 (yellow lines) due to the AMOC collapse, while using the profile 3 (green lines) the PlaSim-LSG model maintains the oceanic circulation but overestimates (up to 12 K) near-surface air temperatures from 40° to 90° in the SH.

In order to explore the contribution of the vertical diffusion at different depths and to find a better profile, I have performed simulations changing the surface and/or the bottom value of A_v (not shown). This analysis has revealed that the value of A_v in the first 2000 m of the ocean plays an important role,

while its variation below 2000 m has no significant impact. Based on these results, I have chosen a vertical diffusion profile (run 4) with a surface value of $A_v = 0.45 \cdot 10^{-4} \text{ m}^2\text{s}^{-1}$ and a bottom value of $A_v = 1.3 \cdot 10^{-4} \text{ m}^2\text{s}^{-1}$ (see Table 3.1 and solid black lines in Fig. 3.2), which is the best compromise between active AMOC (about 19 Sv) and lower temperature in the SH in order to have as much as possible sea ice. In this configuration, the zonally-averaged maximum warm bias in the Southern Ocean is 8 K.

In the attempt to reduce this bias, I have modified other parameters (within physically acceptable limits), such as the cloud albedo, the oceanic albedo and horizontal diffusion, the ozone concentration in the atmosphere, but with a negligible improvement of the resulting climate, as described in the following paragraph. Based on these results, I have concluded that the simulation with profile 4 (black lines in Fig. 3.2) best reproduces temperature estimates from reanalysis and I have chosen it for the following PlaSim-LSG runs.

3.3 Exploration of atmospheric and oceanic parameters to reduce the Southern Ocean bias

As described in Section 3.2, temperatures simulated by the PlaSim-LSG model have a good agreement with the observed values almost everywhere but not in the latitudinal band between 40° and 90°S , where temperatures are overestimated and sea ice is highly underestimated. In the PlaSim configuration with ML ocean, the ocean dynamics is parameterized in a simple way by the horizontal diffusion coefficient K_h . Different values in the two terrestrial hemispheres can be chosen for this coefficient, in order to transport the heat amount needed to obtain realistic temperatures. In the PlaSim configuration with ocean LSG, the dynamics is instead completely described by the equations and it is difficult to make changes that affect only a particular region of the Earth, in this case the one characterized by the warm bias. However, some components of the Earth system or parts of them are present only in some regions, and by changing the values of some parameters associated with these components would allow to change the climatic features mainly in that area. Therefore, I have explored the role of some atmospheric and oceanic model parameters that have a particular importance in the Southern Ocean, modifying the default value to reduce the temperature bias. Since this analysis was carried out at the same time as the tuning of the vertical oceanic diffusion coefficient A_v (see Section 3.2) and an optimal value had not yet been defined, all the studies presented in this section have been made starting from the model configuration with A_v suggested by Sciascia (2008).

3.3.1 Oceanic horizontal diffusion coefficient

Oceans are not equally distributed in the two hemispheres of the Earth: in the NH oceans cover about 60% of the surface area, while about 80% of the SH is covered by oceans (Vallis, 2011). For this reason, I have explored other oceanic parameters in addition to the vertical diffusion coefficient, in order to find a parameter with a larger impact in the SH than in the NH. The first parameter I have analysed is the horizontal diffusion coefficient A_h in LSG. Following Bryan and Lewis (1979), the depth dependence of A_h is taken to reflect the ocean’s tendency to diffuse more rapidly at the surface than at the depth:

$$A_h(z) = (A_b - S) + (A_s - A_b) e^{-0.002z} \quad (3.2)$$

where A_s and A_b are the surface and bottom values of A_h . I have introduced the parameter S to shift the A_h coefficient towards lower values while keeping the shape of the profile. The default values for these three model parameters are $A_s = 1000 \text{ m}^2\text{s}^{-1}$, $A_b = 500 \text{ m}^2\text{s}^{-1}$, $S = 0 \text{ m}^2\text{s}^{-1}$, as shown in Table 3.2 (coefficient 2).

Table 3.2: Horizontal diffusion parameters used in PlaSim-LSG simulations. Each row indicates parameters which describe a different A_h profile, corresponding respectively to the blue, black, red, yellow, purple and green lines shown in Fig. 3.3.

A_h	$A_s[\text{m}^2\text{s}^{-1}]$	$A_b[\text{m}^2\text{s}^{-1}]$	$S[\text{m}^2\text{s}^{-1}]$
1	600	500	0
2 (default)	1000	500	0
3	5000	500	0
4	1000	500	250
5	1000	500	400
6	500	500	400

The black line in Fig. 3.3 shows the results of the simulation performed with Plasim-LSG T21 keeping the default value for the horizontal diffusion coefficient. For the sake of completeness, I want to specify that the differences with respect to the green line in Fig. 3.2 are due to a different value of the cloud albedo parameter (tswr1) discussed in Subsection 3.3.3. In order to assess the impact of horizontal oceanic diffusion on the warm bias in the SH, I have performed five 2000 year long runs modifying the A_h profile (see Table 3.2 and Fig. 3.3): the coefficient sets 1 and 3 have the same value at the ocean bottom and are respectively lower and higher than the default coefficient at the surface; coefficient sets 4 and 5 have the same shape as the default coefficient but are shifted towards lower values, in an attempt to transport less heat towards the South Pole; finally, coefficient set 6 has the same small value over the whole water column. Coefficient

set 3 cannot be chosen as optimal parameter because it is associated to an AMOC that is too intense compared to literature estimates (Srokosz et al., 2012) and consequently the temperatures are higher than those obtained with the default coefficient in both hemispheres. Coefficient set 6, on the other hand, is too low and prevents the model from reaching equilibrium, as I have verified by extending the simulation by 2000 years (not shown). Due to the impossibility of determining the years at equilibrium, I have not represented the zonal mean of near-surface air temperatures and sea ice cover for coefficient set 6. Coefficient sets 1, 4 and 5 give similar results to those of the simulation with default coefficients: although the AMOC is more irregular and with larger oscillations, the zonal means are equal, with an almost total absence of sea ice in the SH. The range of values I have explored for the horizontal oceanic diffusion coefficient A_h is rather wide and this analysis shows that it does not significantly affect the temperature, so it cannot be modified to effectively reduce the warm bias in the Southern Ocean. Therefore, I have kept the default profile for A_h .

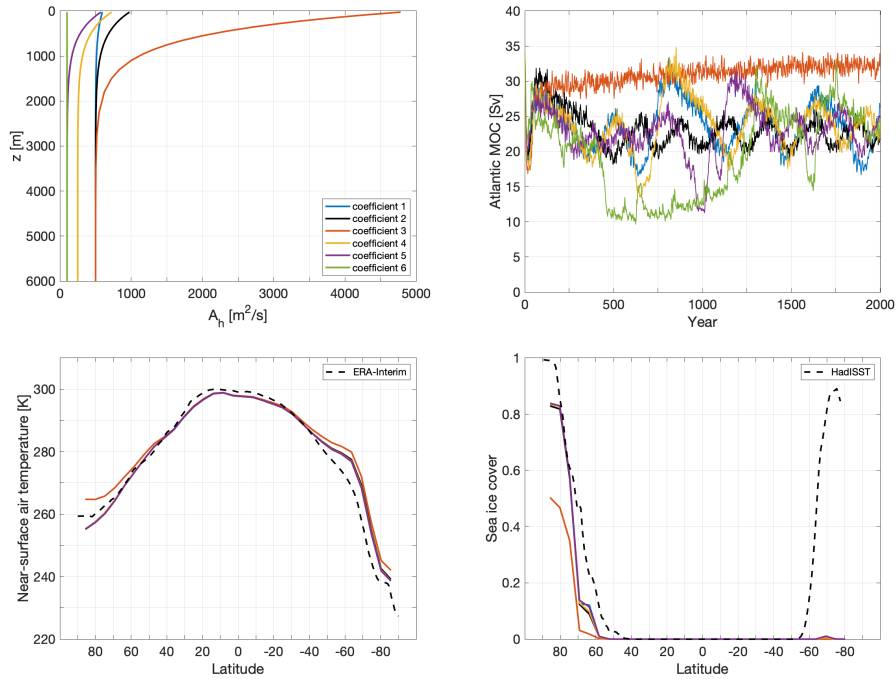


Figure 3.3: Horizontal diffusion profiles in PlaSim-LSG and maximum of the AMOC between 46-66°N and below 700 m (top). Zonal mean of near-surface air temperature and sea ice cover (anomalies with respect to ERA-Interim reanalysis and HadISST observations are in the inner boxes) for different horizontal diffusion profiles in the LSG ocean. Reanalysis and observations are represented by black dashed lines.

3.3.2 Sea ice albedo parameter

To explore the reason of high temperatures in the SH simulated in PlaSim-LSG, I have computed the anomalies at the surface of shortwave and longwave radiative components with respect to the observational dataset CERES EBAF (Loeb et al., 2018). Figure 3.4 shows a strong anomaly in the Southern Ocean in most panels: the shortwave radiation reflected at the surface is too low and the longwave radiation emitted by the surface is too high. These issues can be respectively attributed to the lack of sea ice (whose albedo is higher than ocean albedo) and to the high temperature in that region. However, other components can play an important role in determining radiative fluxes, such as the albedo of the ocean, which is ice-free in the Southern Ocean, or cloud albedo.

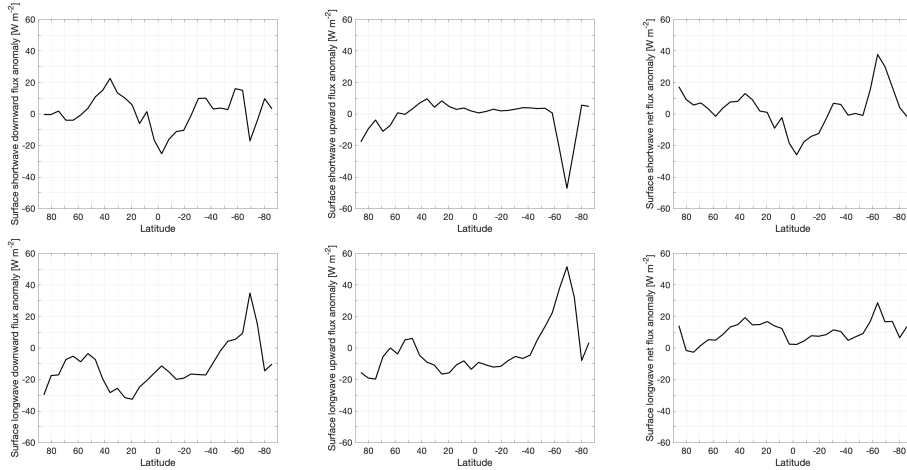


Figure 3.4: Anomalies of shortwave (top) and longwave (bottom) components of radiative flux at the surface, computed with respect to the CERES EBAF dataset.

Albedo for the free ocean in PlaSim is represented by the parameter $albsea$, whose default value is 0.069 (black marker and line in Fig. 3.5). To identify the relationship between the global near-surface air temperature T and $albsea$, I have performed other two 2000 year long runs using $albsea = 0.059$ and $albsea = 0.079$ respectively. Figure 3.5 shows the near-surface air temperature as a function of the ocean albedo.

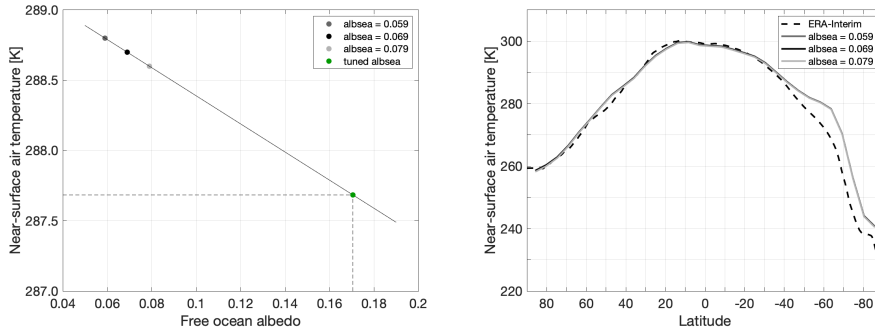


Figure 3.5: Relationship between global mean of near-surface air temperature and *albsea* (albedo for free ocean) in PlaSim-LSG (left). Zonal mean of near-surface air temperature for different values of *albsea*.

From the linear regression I have obtained the following relationship:

$$T = -10 \text{ albsea} + 289.39 \quad (3.3)$$

According to this equation, the ocean albedo in PlaSim-LSG should be increased to 0.171 to have the same global mean temperature as the ERA-Interim reanalysis. This value is too high compared to the range of ocean albedo indicated in the literature. Furthermore the zonal mean of near-surface air temperature in Fig. 3.5 shows that changing the ocean albedo does not correspond to a significant difference in the Southern Ocean. Therefore also this parameter has to be discarded in this study to reduce the warm bias in PlaSim-LSG.

3.3.3 Cloud albedo parameter

In PlaSim, the effect of clouds on shortwave radiative fluxes can be implemented using the parameterization following Stephens (1984) or prescribed cloud properties (Lunkeit et al., 2011). In the parameterization of Stephens (1984), which is the default setup, there is only cloud scattering in the spectral range of visible and ultraviolet (range 1), while in the near infrared (range 2) both cloud scattering and absorption are parameterized. The backscatter coefficient in range 1 depends on the parameter *tswr1*, which allows a tuning of cloud albedo and by default is 0.077. As cloud albedo increases, a bigger amount of shortwave radiation is reflected and less radiation reaches the surface, whose warming is smaller. In order to explore the role of the parameter *tswr1* in the model, I have performed two 2000 year long runs increasing *tswr1* to 0.08 and 0.085 respectively, and identified the relationship between near-surface air temperatures and *tswr1* (see Fig. 3.6):

$$T = -102.04 \text{ tswr1} + 296.60 \quad (3.4)$$

From this equation can be derived $tswr1 = 0.087$, needed to obtain the global mean temperature of ERA-Interim. Therefore I have performed a new simulation with this value and represented the zonal mean of near-surface air temperatures in Fig. 3.6. The parameter $tswr1$ is not suitable for reducing the warm bias in the Southern Ocean: its change has decreased the global mean temperature uniformly at all latitudes, decreasing the warm bias between 40 and 90°S but introducing a new bias, of opposite sign, between the Tropics and at the North Pole. This is due to the fact that $tswr1$ acts on model clouds in all atmospheric levels, while it may be more interesting to isolate the effect of clouds in the warm bias region.

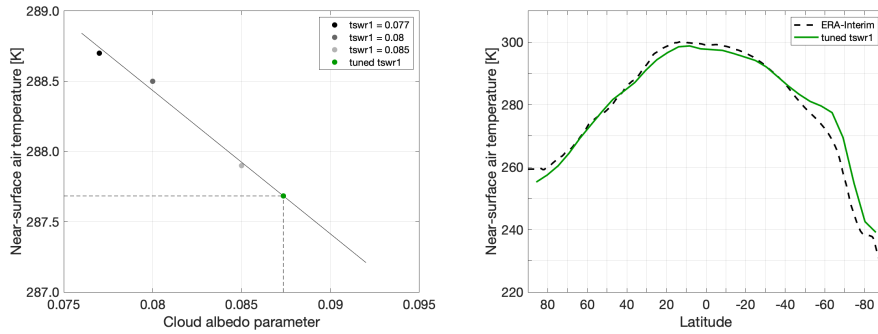


Figure 3.6: Relationship between global mean of near-surface air temperature and $tswr1$ (tuning of cloud albedo in spectral range 1) in PlaSim-LSG (left). Zonal mean of near-surface air temperature for different values of $tswr1$.

PlaSim has low clouds in vertical levels 7-10, medium clouds in levels 5-6 and high clouds in levels 1-4, which are distributed on Earth as shown in Fig. 3.7. The latitudinal band between 40 and 90°S mainly includes medium clouds and (to a lesser extent) low clouds. I have made two simulations increasing the parameter $tswr1$ by 25% in levels 5-6 (medium clouds) and 7-10 (low clouds), respectively. Also with this method the impact on the Southern Ocean temperatures is negligible (not shown): modifying the albedo of medium clouds, for example, the near-surface air temperature decreases only by 0.5 K in the SH but 2 K in the NH. Therefore, if $tswr1$ were further increased it would lead to lower temperatures outside the Southern Ocean.

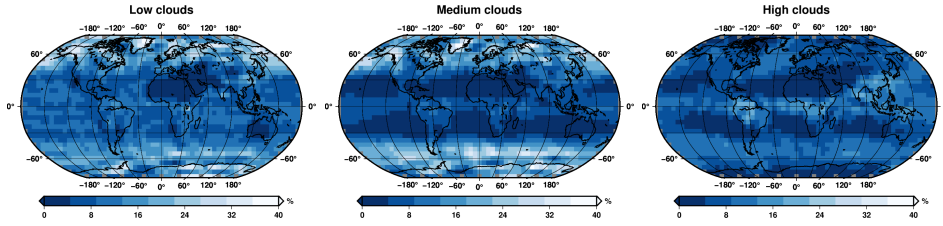


Figure 3.7: Distribution of low (levels 7-10), medium (levels 5-6) and high (levels 1-4) clouds in PlaSim-LSG.

3.3.4 Prescribed cloud properties

The other parameterization for the effect of clouds on shortwave radiation is represented by prescribed cloud properties, which in the simple parameterization used in PlaSim provide fixed values for albedo and absorption coefficient in each spectral range and depending on the atmospheric level. Figure 3.8 shows the difference in the zonal means of near-surface air temperatures between the parameterization of Stephens (1984) with $tswr1 = 0.087$ (see Subsection 3.3.3) and the prescribed cloud properties. The two different implementations generate small temperature deviations from the ERA-Interim reanalysis at all latitudes except in the Southern Ocean. Although prescribed cloud properties seem to work better in the tropical zone, the differences are small enough to maintain the default parameterization, following Stephens (1984).

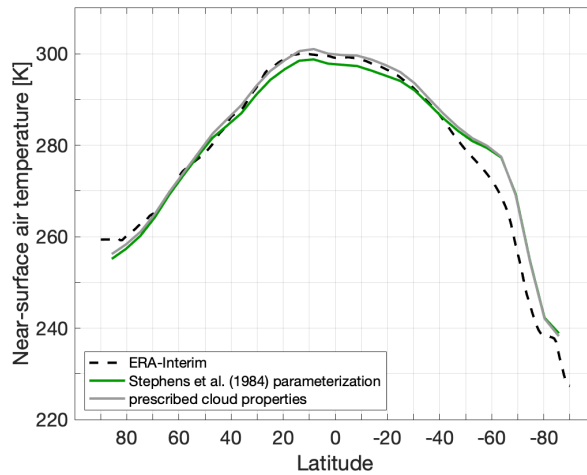


Figure 3.8: Zonal mean of near-surface air temperature for different parameterization of the effect of clouds on shortwave radiation.

3.4 Concluding remarks

The preliminary tuning has allowed to determine the optimal values for the horizontal diffusion coefficient in PlaSim-ML and for the vertical diffusion coefficient in PlaSim-LSG, which in the default version do not allow to obtain realistic zonally-averaged near-surface temperature profiles. The main problem that remains unresolved concerns the overestimation of temperatures in the latitudinal band between 40 and 90°S in PlaSim-LSG. The methods tested so far to reduce temperature bias in the ocean near the South Pole have led to poor results, because in PlaSim-LSG the sensitivity of temperature to the explored parameters is very weak. Similar issues have also been found in some more complex global climate models (Schneider and Reusch, 2016) and solutions are still under investigation. Recent studies show that improvements in the representation of cloud microphysics and aerosol-cloud feedbacks are required to tackle this bias (Hyder et al., 2018). In PlaSim techniques involving parameterizations of atmospheric aerosol cannot be applied as it does not contain an explicit representation of them. There are also complicated indirect feedback associated with clouds that are not included even in more complex models. Another possibility to reduce the Southern Ocean bias may be related to the modification of ozone concentration, which in PlaSim is prescribed using an annual cycle with latitudinal dependence which is based on the ozone distribution by Green (1964). However, some preliminary experiments have shown that the model has a very small sensitivity to large variations of ozone (not shown). More unrealistic methods could be tested, such as modifying the albedo of all the clouds (not only medium or low) present in the critical latitudinal band. However, in this PhD thesis I have not explored further possibilities of temperature bias correction. The reference configuration of PlaSim-LSG, which I have used for studies presented in the next chapters, includes only one fundamental difference compared to the default version of the model: the vertical oceanic diffusion coefficient A_v (between $0.45 \cdot 10^{-4} \text{ m}^2\text{s}^{-1}$ at the surface and $1.3 \cdot 10^{-4} \text{ m}^2\text{s}^{-1}$ at the bottom of the ocean). It is important to keep in mind that the tuning of this model configuration still provides an unresolved problem, which causes too warm temperatures and absence of sea ice in the latitudinal band between 40 and 90°S.

Chapter 4

Model climate

The preliminary analysis of oceanic parameters described in Chapter 3 has allowed to define and tune three configurations of the model. The first configuration consists of PlaSim coupled with the ML ocean, run at T21 spatial resolution and with two different horizontal oceanic diffusion coefficients, for the NH ($K_h = 10^5 \text{ m}^2\text{s}^{-1}$) and for the SH ($K_h = 10^4 \text{ m}^2\text{s}^{-1}$). The second configuration is similar to the first one but the spatial resolution is finer (T42) and with a different horizontal diffusion oceanic coefficient in the SH ($K_h = 3 \cdot 10^4 \text{ m}^2\text{s}^{-1}$). In the third model set-up PlaSim is dynamically coupled with LSG and the vertical diffusion coefficient A_v in the ocean is described by the function plotted in the first panel of Fig. 3.2 (black line) and spans from $1.3 \cdot 10^{-4} \text{ m}^2\text{s}^{-1}$ at the ocean bottom to $0.45 \cdot 10^{-4} \text{ m}^2\text{s}^{-1}$ at the ocean surface. The characteristics of the mean climate under these configurations have been explored and are presented in this chapter.

4.1 Poleward heat transport

The choice of oceanic parameters can be further justified by comparing, in terms of poleward heat transport, the tuned configurations defined in Chapter 3 with their respective reference configurations (available in the current version of the model or suggested by literature). The reference configurations of PlaSim-ML use a default value of horizontal diffusion in the ML ocean ($K_h = 10^3 \text{ m}^2\text{s}^{-1}$, see Chapter 3 Section 3.1) for NH and SH. The reference configuration of PlaSim-LSG uses the vertical diffusion profile in LSG suggested in literature by Bryan and Lewis (1979), which describe an arctan-shaped profile ranging from $0.3 \cdot 10^{-4} \text{ m}^2\text{s}^{-1}$ at the top to $1.3 \cdot 10^{-4} \text{ m}^2\text{s}^{-1}$ at the bottom of the ocean (see Chapter 3 Section 3.2). Figure 4.1 shows the oceanic and atmospheric heat transport for all these configurations. For comparison, an oceanic heat transport estimate using the ERA-Interim reanalysis dataset is also included. Simulations performed using tuned oceanic parameters (solid lines) reproduce the oceanic heat transport

from reanalysis (black line) better than simulations with default parameters (dashed lines). In particular, a remarkable improvement is observed in PlaSim-ML, suggesting that the default horizontal diffusion coefficient is too small to represent oceanic transport correctly. Using the new vertical diffusion profile, the simulated transport in PlaSim-LSG is more similar to the ERA-Interim transport in the NH and the difference compared to the Bryan and Lewis (1979) profile can be attributed to the heat transported by the AMOC (see Chapter 3 Section 3.2). The largest differences between the model and the reanalysis occur in the SH, in particular between 30 and 50°S. The atmospheric transport simulated using reference configurations is bigger, therefore in a better agreement with the reanalysis, because it balances the insufficient oceanic transport (which is almost absent in PlaSim-ML). Instead new configurations simulate an atmospheric heat transport in general too small. However, even when using default oceanic parameters, the atmospheric transport is not perfectly reproduced in the NH, where it is too high between 0 and 40°N.

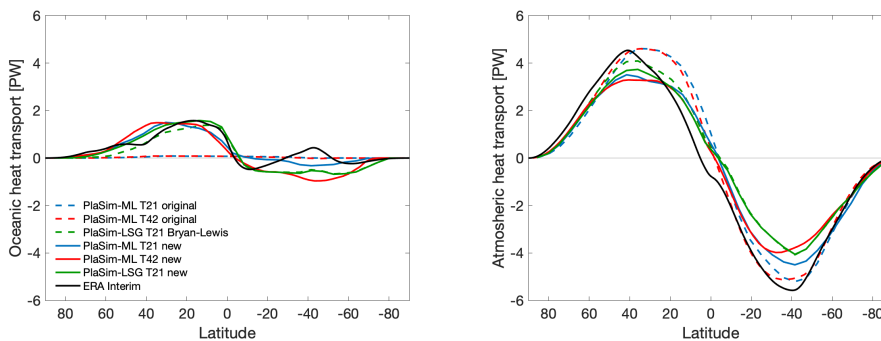


Figure 4.1: Zonally-averaged annual mean oceanic and atmospheric heat transport as a function of latitude for reference (dashed lines) and tuned (colored solid lines) coupled configurations of PlaSim. The reference configuration of PlaSim-ML is the original version with default horizontal diffusion coefficient, the reference configuration of PlaSim-LSG has the vertical diffusion profile suggested by Bryan and Lewis (1979). The ERA-Interim values are the black lines.

4.2 Simulated climate

Figure 4.2 compares near-surface air temperature, sea surface temperature, sea ice cover, precipitation and TOA net radiation anomalies of PlaSim-ML and PlaSim-LSG against satellite observations and the ERA-Interim reanalysis dataset, as summarized in Table 4.1. In particular the average over the last 30 years of the perennial simulation for PlaSim-ML and over

the last 1000 years for PlaSim-LSG was compared with the average over the period 2005-2015 for the observational and reanalysis datasets.

Table 4.1: Observational and reanalysis datasets used in this paper.

Variable	Dataset	Period	Horizontal resolution [°]
Near-surface air temperature	ERA-Interim (Dee et al., 2011)	2005-2015	0.75
Sea surface temperature	HadISST (Rayner et al., 2003)	2005-2015	1
Sea ice cover	HadISST (Rayner et al., 2003)	2005-2015	1
Precipitation	GPCP (Adler et al., 2003)	2005-2015	2.5
Radiation	ERA-Interim (Dee et al., 2011)	2005-2015	0.75
AMOC	Literature	-	-

In general, simulated near-surface air temperatures are warm biased over the land pixels and cold biased over the ocean pixels. Near-surface air temperatures simulated with PlaSim-ML at T21 are warm biased in Canada and Greenland and cold biased in the Barents Sea, while Antarctica shows both cold and warm anomalies. These anomalies are smaller using the T42 resolution. With PlaSim-LSG the cold anomaly over the Barents Sea increases and a large warm bias (up to 20 K in some pixels) over the Southern Ocean is a very clear feature in this simulation. A similar pattern is observed in sea surface temperature anomalies, which show too warm temperatures on the western coast of America and Africa. Temperature anomalies in the polar regions are consistent with the simulated sea ice cover. Using PlaSim-ML at T21, the model simulates too little sea ice over the Arctic Ocean and too much sea ice over most of the Southern Ocean. With PlaSim-ML at T42 sea ice is underestimated in both hemispheres but it is overestimated in the Barents Sea. Finally, PlaSim-LSG leads to a strong negative sea ice anomaly in the Southern Ocean, where sea ice is almost completely absent due to the warm bias. The simulated precipitation has a relatively good agreement with the observational data, except for the positive anomaly (about 10 mm/day) in the equatorial region using the model with the ML ocean. PlaSim-LSG better correlates with the observed precipitation than PlaSim-ML. Finally, TOA net fluxes show a negative anomaly in the tropics and subtropics, where the upward radiation is overestimated, and a positive anomaly in the mid-latitude and polar zones, where the upward radiation is underestimated. Furthermore, a positive anomaly of net radiation is observed on the western coast of America and Africa, consistently with the warm biased near-surface air temperatures.

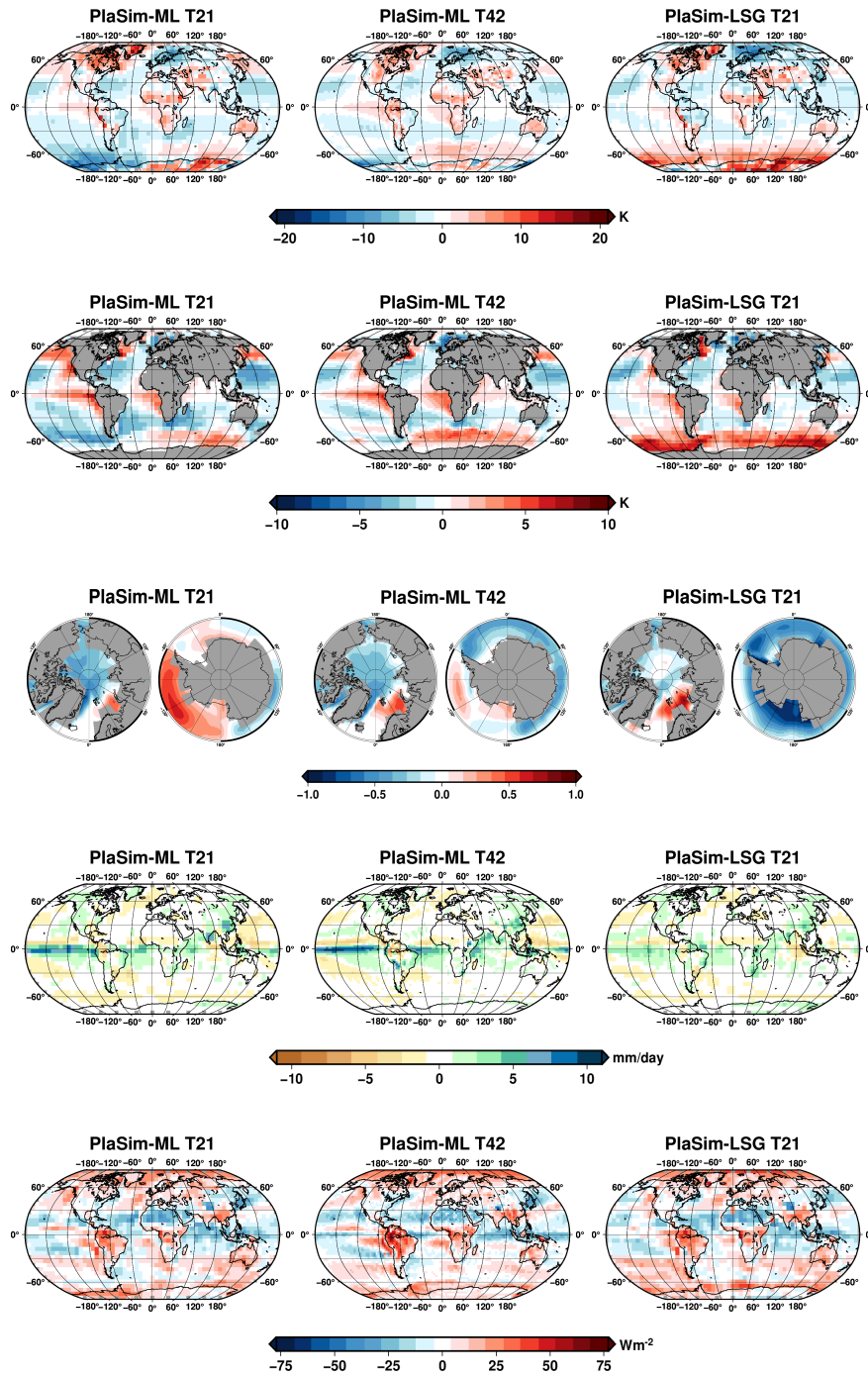


Figure 4.2: Difference between simulated and observed near-surface air temperature, sea surface temperature, sea ice cover, precipitation and TOA net radiation for the three selected configurations of the model: PlaSim with the ML ocean and T21 (left), PlaSim with the ML ocean and T42 (middle), PlaSim with the LSG ocean and T21 (right).

4.3 Energy balance

For any coupled climate model to reach a stationary stable state, the TOA and the surface energy balances should be close to zero (neglecting geothermal heating) since the model should present no significant internal energy sources or sinks. Table 4.2 compares the global energy balance resulting from our simulations (performed using new oceanic parameters defined in Chapter 3) with estimates from Stephens et al. (2012). While the former are the results of perennial model simulations with PlaSim, the latter refers to an observed climatology calculated over the time period 2000-2010 during a period of climate change, so it presents positive TOA and surface radiative net fluxes.

Table 4.2: TOA and surface energy fluxes in Wm^{-2} . Latent heat flux also includes the snow contribution. Precipitation-evaporation (P-E) imbalance is reported as latent heat.

	PlaSim-ML T21	PlaSim-ML T42	PlaSim-LSG T21	Stephens et al. (2012)
TOA net shortwave	231.5	235.8	232.8	240.2
TOA net longwave	-232.3	-236.0	-232.9	-239.7
TOA energy budget	-0.76	-0.11	-0.14	0.6
Surface net shortwave	163.2	169.4	164.1	165
Surface net longwave	-62.8	-62.4	-63.0	-52.4
Sensible heat flux	-18.9	-20.8	-18.3	-24
Latent heat flux	-82.0	-86.5	-82.7	-88
Surface energy budget	-0.52	-0.23	0.06	0.6
TOA-surface net	-0.24	0.12	-0.20	0
P-E imbalance	$-2.6 \cdot 10^{-3}$	$-2.3 \cdot 10^{-3}$	$-1.9 \cdot 10^{-3}$	-

The second-to-last row of Table 4.2 shows the difference between the TOA and the surface net fluxes (which should be zero on average), indicating that none of the three PlaSim configurations conserves energy perfectly in the atmosphere. PlaSim-ML (with T21 resolution) and PlaSim-LSG configurations provide a negative balance indicating that the model atmosphere presents an internal energy source corresponding to 0.24 and 0.20 Wm^{-2} , respectively. The PlaSim-ML (T42) configuration, on the other hand, gives rise to a positive balance (there is a consumption of energy, corresponding to 0.12 Wm^{-2} , in the model atmosphere). We tested if this imbalance is caused by a missing conservation of water mass in the model atmosphere (possibly to transport errors), but the absolute value of the global average freshwater flux P-E is smaller than 10^{-4} mm/day, equivalent to a very small latent heat flux smaller than $2.6 \cdot 10^{-3}$ Wm^{-2} for all tested PlaSim configurations, indicating that water is well conserved in the PlaSim atmosphere. Also, all ML simulations present a negative net energy flux at the surface, suggesting some non-conservation of energy (equivalent to an energy production) in the ML ocean. Both the TOA-surface imbalance and the net surface flux bias are reduced in the T42 ML simulation, suggesting that these biases may be resolution-dependent. Overall these energy imbalances are small

compared to those reported for CMIP5 and CMIP3 models (which could exceed 1 W/m^2 in magnitude at TOA (Mauritsen et al., 2012)).

4.4 Historical runs and future projections

After examining some characteristics of the simulated present climate and verified that most variables are well reproduced, the three PlaSim configurations have been used to perform transient simulations from 1850 to 2100, consistently with similar studies on the CMIP5 models and EMICs that are presented in the AR5 of IPCC (2013), with the aim of assessing the ability of the model to reproduce the past and future climate. In these experiments, the CO_2 forcing is prescribed as a time series of global mean concentration. This CO_2 concentration is based on measured values for past years and on several Representative Concentration Pathways (RCPs) for future projections, i.e. possible trajectories of carbon dioxide which have been used for climate modeling and research in the IPCC AR5. Left panel in Fig. 4.3 shows the global mean of near-surface air temperatures anomaly (computed with respect to 1961-1990), which is obtained with the three configurations of PlaSim using for the future two scenarios related to an increase in radiative forcing of 4.5 Wm^{-2} (RCP 4.5) and 8.5 Wm^{-2} (RCP 8.5). Temperatures simulated by PlaSim from 1850 to the present-day have been compared with the HadCRUT observational dataset (Morice et al., 2012), whose values are represented by the black line. The configurations with the ML ocean start from lower pre-industrial temperatures and have a larger temperature increase than those observed in the HadCRUT dataset or simulated with PlaSim-LSG. This last configuration is the one that best reproduces temperature anomalies, despite being characterized by an overestimation of temperatures in the SH, as described in this chapter. Future projections can instead be compared with temperature anomalies (relative to the same period 1961-1990) which are obtained from experiments with CMIP5 models for four possible CO_2 concentration scenarios, including 4.5 and 8.5 (right panel in Fig. 4.3). Also in this case, the PlaSim-LSG configuration provides more compatible results with other climate simulations than the configurations of PlaSim with the ML ocean, which give too fast temperature increase for both scenarios, with anomalies almost double with respect to those of CMIP5 models at the end of this century. In the PlaSim-ML configurations, the ocean is represented by a shallow layer with a small heat capacity: for this reason, the mixed-layer ocean reacts more quickly to changes in boundary conditions (such as increased CO_2) than a deep ocean like LSG or the real ocean. In this way, the system rapidly reaches an equilibrium state, contributing to the fast temperature increase that characterizes the PlaSim-ML configurations. Furthermore, the fast warming of a shallow ocean has an impact on the sea-ice feedback, which is amplified and further contributes to

the temperature increase.

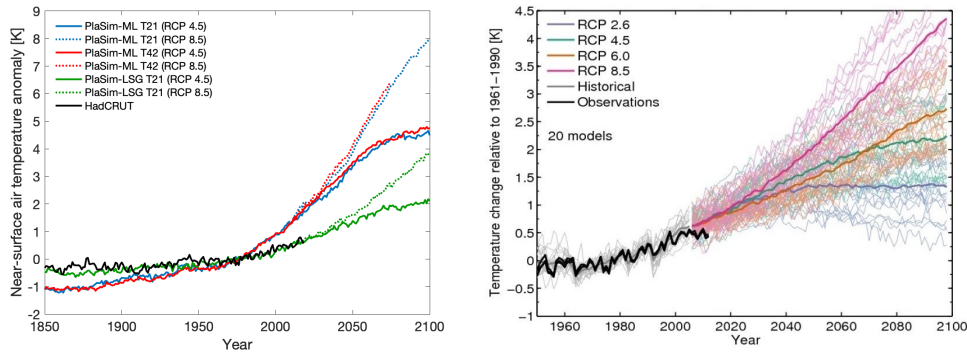


Figure 4.3: Near-surface air temperature anomalies relative to the 1961-1990 mean, obtained using for each of the three PlaSim configurations two different Representative Concentration Pathways, RCP 4.5 (solid line) and RCP 8.5 (dotted line). The black line represents the HadCRUT observational dataset (left). Global mean annual temperature anomalies computed with respect to the period 1961-1990, obtained from experiments using CMIP5 models for four different possible CO_2 concentration scenarios, including RCP 4.5 and RCP 8.5 (right; image processed by Ed Hawkins, University of Reading, <https://www.climate-lab-book.ac.uk>.)

The amount of global surface warming that occurs in response to an increase of atmospheric CO_2 concentration is linked to the notion of climate sensitivity. In the study of climate models, there are several methods for estimating their climate sensitivity. The main measures of how the system responds to a specific forcing change are the equilibrium climate sensitivity (ECS), the amount of warming that follows an abrupt CO_2 doubling, and the transient climate response (TCR), the amount of warming that occur when the CO_2 is gradually doubled with an increase of 1% each year. In the following chapter, the PlaSim response to an increase in CO_2 forcing is estimated using the definition of ECS.

The results of this section are in line with those obtained and analysed in Chapter 5, which demonstrates that the ECS value in the PlaSim-ML configurations is higher than the value estimated in PlaSim-LSG. These considerations should be taken into account when using PlaSim for future climate simulations, especially in the study of exoplanetary climates for which the ML ocean can only be used because the LSG ocean is specific for the representation of the terrestrial dynamics.

Chapter 5

Equilibrium climate sensitivity

5.1 The Gregory method

Equilibrium climate sensitivity (ECS) is defined as the equilibrium change in global mean surface air temperature after an instantaneous doubling of atmospheric CO₂ relative to pre-industrial levels (IPCC, 2013). Climate sensitivity can be diagnosed following the approach by Gregory et al. (2004) and here I have applied this method to PlaSim-ML and PlaSim-LSG simulations. When a radiative forcing R (Wm⁻²) is applied to the model, the model responds with a change in the net TOA radiative flux ΔF (Wm⁻²) and, in order to restore the radiative equilibrium, the global mean near-surface air temperature, ΔT , changes, until ΔF is returned to zero. R , ΔF and ΔT are related by the following equation:

$$\Delta F = R - \lambda \Delta T \quad (5.1)$$

where λ (Wm⁻²K⁻¹) is referred to as climate feedback parameter. If ΔF is assumed to be a linear function of ΔT , both the radiative forcing and the feedback parameter can be diagnosed by linear regression: R is the intercept at $\Delta T = 0$ and λ is the slope (multiplied by -1). The equilibrium temperature change can be estimated extrapolating the heat balance to equilibrium, that is $\Delta F = 0$ and $\Delta T^{\text{eq}} = R/\lambda$. If the forcing is a doubling of CO₂, ΔT^{eq} is the equilibrium climate sensitivity by definition.

I have performed a first set of simulations using dynamic sea ice (subscript d in subsequent text): the first part of each simulation is a perennial run with pre-industrial boundary conditions, so the CO₂ concentration in the atmosphere is set to 285 ppm (1xCO₂); the second part is a perennial run in which the CO₂ concentration is instantaneously increased at 1.5, 2, 3 or 4 times the value of the pre-industrial simulation. These simulations were made with the three tuned configurations of PlaSim (whose oceanic parameters

are defined in Chapter 3). Each half-simulation is 100 years long when using PlaSim-ML and 2000 years long when using PlaSim-LSG. The yellow and the red lines in Fig. 5.1 show the change in net TOA radiative flux versus the change in global mean near-surface air temperature for each dynamic-ice simulation with doubled ($2\times\text{CO}_2$) and quadrupled ($4\times\text{CO}_2$) atmospheric CO_2 . Changes are computed with respect to the corresponding $1\times\text{CO}_2$ part of the simulation.

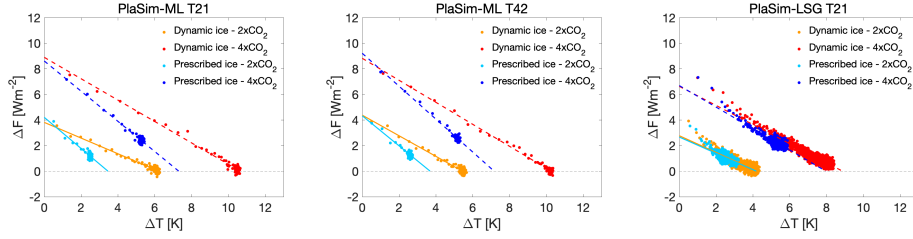


Figure 5.1: Relationships between ΔF , the change in net TOA radiative flux, and ΔT , the change in global mean near-surface air temperature, after an instantaneous doubling and quadrupling of CO_2 , using dynamic or prescribed sea ice. Data points are global and annual means simulated with PlaSim-ML T21, PlaSim-ML T42 and PlaSim-LSG T21. Lines represent ordinary least squares regression fits.

Table 5.1: Key values derived from simulations performed using the tuned configurations of PlaSim (defined in Chapter 3) and four different CO_2 level increase factor: climate feedback parameter λ_d , radiative forcing R_d , equilibrium temperature ΔT_d^{eq} , pre-industrial (I_d^{PI}) and final (I_d) sea ice area at equilibrium for the dynamic-ice simulations; climate feedback parameter λ_p , radiative forcing R_p , equilibrium temperature ΔT_p^{eq} and sea ice area for the prescribed-ice simulations; sea ice feedback parameter λ_i , computed as the difference between λ_d and λ_p . The reported uncertainties are standard deviations.

PlaSim config.	CO_2 factor	λ_d [$\text{Wm}^{-2}\text{K}^{-1}$]	R_d [Wm^{-2}]	ΔT_d^{eq} [K]	I_d^{PI} [10^{12}m^2]	I_d [10^{12}m^2]	λ_p [$\text{Wm}^{-2}\text{K}^{-1}$]	R_p [Wm^{-2}]	ΔT_p^{eq} [K]	I_p [10^{12}m^2]	$\lambda_i = \lambda_d - \lambda_p$ [$\text{Wm}^{-2}\text{K}^{-1}$]
ML T21	1.5	0.58 ± 0.16	2.10 ± 0.55	3.64 ± 0.20	29.81	15.64	1.08 ± 0.62	2.22 ± 0.85	2.05 ± 0.40	29.65	-0.50 ± 0.64
	2	0.61 ± 0.10	3.82 ± 0.56	6.23 ± 0.19	29.81	8.40	1.22 ± 0.36	4.22 ± 0.89	3.46 ± 0.32	29.65	-0.60 ± 0.38
	3	0.71 ± 0.07	6.47 ± 0.39	9.16 ± 0.16	29.81	3.24	1.20 ± 0.22	6.87 ± 0.91	5.73 ± 0.33	29.65	-0.49 ± 0.23
	4	0.84 ± 0.06	8.91 ± 0.64	10.65 ± 0.13	29.81	1.99	1.18 ± 0.17	8.62 ± 0.90	7.31 ± 0.33	29.65	-0.34 ± 0.19
ML T42	1.5	0.79 ± 0.19	2.55 ± 0.59	3.23 ± 0.13	18.15	8.61	1.18 ± 0.56	2.55 ± 0.83	2.16 ± 0.32	18.06	-0.39 ± 0.59
	2	0.81 ± 0.11	4.39 ± 0.60	5.45 ± 0.13	18.15	4.12	1.18 ± 0.33	4.34 ± 0.85	3.69 ± 0.34	18.06	-0.37 ± 0.35
	3	0.81 ± 0.07	6.90 ± 0.61	8.51 ± 0.13	18.15	0.80	1.17 ± 0.21	7.13 ± 0.87	6.08 ± 0.34	18.06	-0.36 ± 0.22
	4	0.86 ± 0.06	8.83 ± 0.62	10.26 ± 0.12	18.15	0.39	1.29 ± 0.18	9.22 ± 0.90	7.17 ± 0.30	18.06	-0.43 ± 0.19
LSG T21	1.5	0.59 ± 0.07	1.58 ± 0.16	2.68 ± 0.06	11.42	6.92	0.49 ± 0.11	1.32 ± 0.15	2.71 ± 0.28	11.44	0.10 ± 0.13
	2	0.65 ± 0.05	2.78 ± 0.17	4.26 ± 0.06	11.42	5.86	0.64 ± 0.11	2.68 ± 0.27	4.19 ± 0.31	11.44	0.02 ± 0.12
	3	0.70 ± 0.03	4.96 ± 0.19	7.07 ± 0.06	11.42	3.55	0.77 ± 0.09	4.91 ± 0.36	6.35 ± 0.27	11.44	-0.07 ± 0.10
	4	0.75 ± 0.03	6.64 ± 0.20	8.88 ± 0.06	11.42	1.58	0.84 ± 0.07	6.70 ± 0.39	7.97 ± 0.25	11.44	-0.09 ± 0.08

I have derived the estimates of R_d (intercept) and λ_d (slope multiplied by -1) through ordinary least squares regression and I have computed $\Delta T_d^{\text{eq}} = R_d/\lambda_d$ for all the PlaSim configurations (Table 5.1). The confidence intervals are obtained as standard deviation on the parameter estimates and error propagation. The resulting ECS for dynamic sea ice is 6.23 K using PlaSim-ML T21, 5.45 K using PlaSim-ML T42 and 4.26 K using PlaSim-LSG T21, using the results from the CO₂ doubling experiments. In Fig. 5.2 these results are compared with values from other models. In particular, the grey boxplots give an indication of the distribution of CMIP5 values (the whiskers extend to the highest and lowest data) discussed in Andrews et al. (2012). Radiative forcing and climate feedback values of PlaSim are within the range estimated for CMIP5 models, but only the PlaSim-LSG coupled model gives an equilibrium climate sensitivity within the CMIP5 range (2.1-4.7 K), though close to the upper limit. The orange boxplot represents the ECS values found in other EMICs (Pfister and Stocker, 2017), which are in good agreement with CMIP5 models but have a wider range of values (1.5-5.5 K). Finally, the blue boxplot shows the most recent range of ECS for CMIP6 models (1.8-5.6 K) (Zelinka et al., 2020).

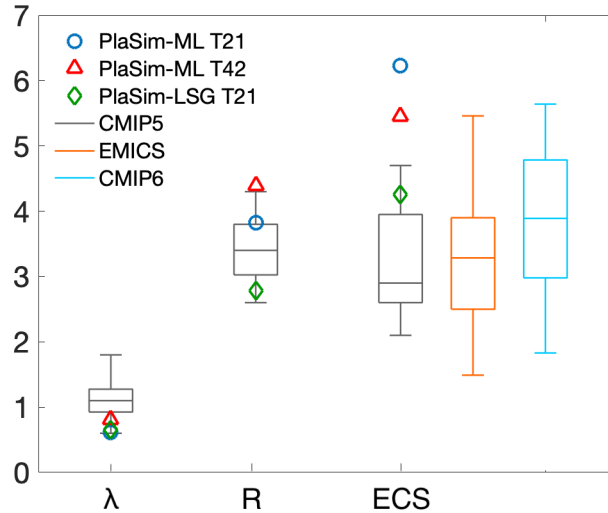


Figure 5.2: Radiative forcing R , climate feedback λ and equilibrium climate sensitivity ECS (in Wm^{-2} , $\text{Wm}^{-2}\text{K}^{-1}$ and K, respectively) values for PlaSim-ML (T21 and T42) and for PlaSim-LSG (T21). Boxplots show the corresponding ranges of values found in CMIP5 models (Andrews et al., 2012) and estimates of ECS values from EMICs (Pfister and Stocker, 2017) and CMIP6 models (Zelinka et al., 2020).

With respect to CMIP5, some components of CMIP6 models have been improved, for example low clouds and shallow convection are better represented (Voldoire et al., 2019) or a more advanced treatment of aerosol is

included (Wyser et al., 2020), and stronger positive cloud feedbacks from decreasing extra-tropical low cloud coverage and albedo have contributed to increased ECS in some of them (Zelinka et al., 2020; Meehl et al., 2020). Since PlaSim does not include such a level of accuracy (for example, it has no parameterization for aerosol-cloud feedbacks as seen in Chapter 3 Section 3.3), its high climate sensitivity cannot be related to these processes. These results can also be compared with an ECS estimate for a modified PlaSim-ML configuration at T21 in Ragone et al. (2016), where the very high value of 8.1 K was reported and attributed to the removal of the diurnal and seasonal cycles in the model. Please notice also that, while EMIC ECS values reported in Fig. 5.2 were obtained, like for PlaSim, from CO₂ doubling experiments, the reported CMIP5 and CMIP6 results were obtained dividing by two the results from 4xCO₂ experiments. As shown in Table 5.1 for PlaSim and as also reported in Pfister and Stocker (2017) for other EMICS, the ECS values obtained from quadrupling experiments may be lower than those obtained from doubling experiments, although often used without distinction as estimates of ECS in the literature.

The difference between the two PlaSim-ML configurations and the PlaSim-LSG configuration can partly be explained by features of the ocean circulation. Using PlaSim-LSG, the AMOC is active (about 20 Sv) in the pre-industrial and 1.5xCO₂ runs, but it collapses (less than 5 Sv) in the 2xCO₂, 3xCO₂ and 4xCO₂ simulations. As shown in Fig. 3.2, global average temperatures are affected significantly by the state of AMOC, with a cooling of up to 1 K in runs with a shutdown of AMOC. As a consequence, the equilibrium climate sensitivity in such runs is smaller than it would be if the AMOC had remained active. Unlike PlaSim-LSG and CMIP models, the PlaSim-ML configurations does not include an AMOC representation, so it cannot weaken and this could contribute to the reported higher ECS.

5.2 The role of sea ice and ocean heat transport

The relatively high values of ECS found for PlaSim are related to low values of the feedback parameter λ_d . I have determined that an important contribution can be traced also to elevated values in magnitude of the ice-feedback parameter, as I have assessed following the approach of Caldeira and Cvijanovic (2014). To this end, I have performed a second set of simulations, similar to the first one but with prescribed sea ice (subscript p): twelve climatological monthly ice extents were derived from the pre-industrial dynamic-ice simulation and were prescribed in the model. The cyan and the blue lines in Fig. 5.1 show the change in net TOA radiative flux versus the change in global mean near-surface air temperature for each prescribed-ice simulation with doubled and quadrupled CO₂ concentration. Using prescribed sea ice, the change in TOA radiative flux at equilibrium is not

zero (see Fig. 5.1) because some energy has to be removed from or added to the system in order to maintain the climatological sea ice thickness (Caldeira and Cvijanovic, 2014). Also in this case, I have computed λ_p (slope multiplied by -1) through ordinary linear least squares regression for all the PlaSim configurations (Table 5.1). The sea ice feedback parameter λ_i (last column of Table 5.1) is negative in my sign convention and is obtained subtracting the feedback parameter of dynamic-ice simulations from that of prescribed-ice simulations. These results can be compared with the slab-ocean experiments performed by Caldeira and Cvijanovic (2014) with the National Center for Atmospheric Research’s Community Earth System Model (CESM): they report a λ_i of $-0.21 \pm 0.19 \text{ Wm}^{-2}\text{K}^{-1}$ in the doubling CO_2 experiments and $-0.30 \pm 0.06 \text{ Wm}^{-2}\text{K}^{-1}$ in the quadrupling CO_2 experiments. The feedback parameter of sea ice in the PlaSim-ML configurations is significantly higher in absolute value than in CESM, suggesting that sea ice plays an important role in determining the ECS of the model. However, this contribution also depends on the extent of sea ice either in the pre-industrial climate (see I_d^{PI} in Table 5.1) or in the future climates (see I_d). Indeed, the sea ice area is very different in the three configurations of PlaSim. For example, in the PlaSim-ML model at T42 the pre-industrial sea ice area is less extended than in the PlaSim-ML model at T21, so the sea ice contribution to ECS is smaller. Furthermore, I recall that sea ice is almost completely absent in the Southern Ocean using PlaSim-LSG, therefore the sea ice contribution to ECS is reduced compared to the configurations with the ML ocean. A factor which also contributes to the low values of λ_i in the PlaSim-LSG configuration is the fact that, in the pre-industrial simulation with prescribed sea ice, the AMOC in the LSG ocean model collapses to very low values after about 1000 years, while using the dynamic sea ice treatment the AMOC is strong in the pre-industrial climate. The AMOC collapse in the prescribed-ice simulation makes the pre-industrial global temperature lower (as reported above), the slope λ_p smaller and the difference λ_i closer to zero than it would be with an active AMOC. Therefore in the PlaSim-LSG model the feedback parameter λ_i , obtained subtracting dynamic-ice from prescribed-ice simulations, includes not only the sea ice contribution but also the AMOC effect, which is positive in this sign convention.

The high impact of sea ice related feedbacks in the model cannot be linked to a too high sea ice albedo in PlaSim: in fact I have compared the average sea ice albedo of PlaSim and that of EC-Earth, a global state-of-the-art climate model with higher complexity and spatial resolution (Hazeleger et al., 2012; Döscher et al., 2021), which has an ECS of 4.3 K in the newer model version (Wyser et al., 2020). The average sea ice albedo of PlaSim-ML T21 is 0.58 for pixels with more than 99% area coverage, lower than the average sea ice albedo of EC-Earth (0.80). Since a smaller sea ice albedo weakens the ice-albedo feedback, I can conclude that the strong impact of dynamic sea ice in PlaSim is not likely due to the ice albedo parameterization employed in

the model. In fact, I have performed a series of climate sensitivity runs with PlaSim (not shown) in which I have modified maximum sea ice albedo and its dependence on temperature, without finding significantly lower values of the ECS.

A confusing factor between the different model configurations is the fact that they are all characterized by different average sea ice extents in the starting pre-industrial experiments. To better compare the impact of the sea ice feedback, I have used the same approach as Caldeira and Cvijanovic (2014), comparing the dynamic-ice and prescribed-ice simulations, to define a measure of the radiative forcing associated with changes in sea ice area. An equivalent formulation with new symbols is:

$$\Delta F_{\text{ice}} = \lambda_p \left(\Delta T_d^{\text{eq}} - \Delta T_p^{\text{eq}} \right) \quad (5.2)$$

which represents a measure of the radiative forcing that should be provided to prescribed-ice experiments in order to undergo the same global mean near-surface air temperature change as in dynamic-ice experiments. Figure 5.3 shows the sea ice radiative forcing versus the relative sea ice area (computed as the difference between I_p and I_d , see Table 5.1): the coupled configurations of PlaSim with tuned oceanic parameters (blue, red and green lines) are compared with CESM, used in Caldeira and Cvijanovic (2014) (black dashed line).

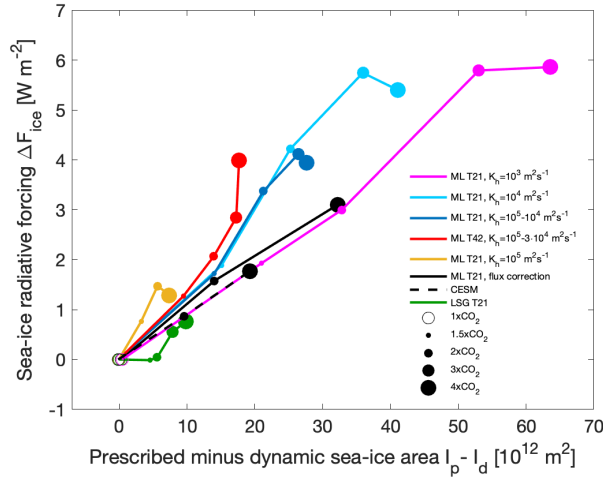


Figure 5.3: Sea ice radiative forcing (see Eq. 5.2) as a function of the relative sea ice area (prescribed-ice area minus dynamic-ice area, see Table 5.1). Values are obtained by estimating the radiative forcing that should be provided to prescribed-ice experiments in order to undergo the same global mean near-surface air temperature change as in dynamic-ice experiments.

The configurations of PlaSim with the ML ocean, in which the oceanic transport is parameterized by a horizontal diffusion term, show a radiative forcing associated with changes in sea ice area which is significantly higher than CESM, consistent with the higher absolute value of λ_i which I have reported above. One important difference between PlaSim experimental results and the CESM results is that the latter experiments used a ML ocean with a prescribed ocean heat flux (Q-flux). In order to verify the role played by the specific parameterization of oceanic transport, I have also performed a series of CO₂ increase experiments with dynamical and prescribed ice, using PlaSim-ML T21 with a Q-flux correction instead of horizontal diffusion in the ML ocean. The Q-flux was derived by the model from present-day Atmospheric Model Intercomparison Project (AMIP) experiment forced with observed sea surface temperatures. The ECS of this configuration is 3.62 K, which is similar to the value of CESM (3.42 K) and smaller than the ECS of PlaSim-ML T21 with horizontal diffusion (6.23 K) and the ECS of PlaSim-LSG (4.26 K). These results are consistent with Danabasoglu and Gent (2009), who found that the ECS of the Community Climate System Model version 3 (CCSM3) using the full-depth ocean model is slightly higher than using the mixed-layer ocean model with a monthly varying heat flux transport, constructed to produce a realistic sea surface temperature. Also Danabasoglu and Gent (2009), however, highlight that the reduction in sea ice resulting from increased CO₂ is important in determining the mixed-layer ocean and full-depth ocean estimates of ECS. Figure 5.3 shows that the configuration of PlaSim-ML T21 with the flux correction (black solid line) gives similar results to CESM in terms of ice forcing, suggesting that the specific choice of parameterization of oceanic heat transport affects the sea ice radiative forcing and as a consequence the ECS of the model. To further explore this point, Fig. 5.3 also shows three additional simulations which use a single horizontal diffusion coefficient for both the hemispheres, $K_h = 10^5 \text{ m}^2\text{s}^{-1}$ (yellow line), $K_h = 10^4 \text{ m}^2\text{s}^{-1}$ (cyan line) and $K_h = 10^3 \text{ m}^2\text{s}^{-1}$ (magenta line). The first and the second coefficient are those used for the NH and the SH in the PlaSim-ML (T21) tuned configuration (see Chapter 3 Section 3.2). We can notice that PlaSim-LSG and PlaSim-ML with the lowest diffusion coefficient ($K_h = 10^3 \text{ m}^2\text{s}^{-1}$) have a slope similar to CESM, while using a higher ocean diffusion, the effective changes in radiative forcing associated with changes in sea ice area increase for increasing horizontal oceanic diffusion. Therefore ultimately the equilibrium climate sensitivity of the PlaSim-ML model using a diffusive term to represent heat transport, depends crucially also on the choice of K_h .

5.3 Concluding remarks

Climate sensitivity experiments with PlaSim have revealed that details of the oceanic heat transport play a fundamental role in determining the ECS of the model. The first important factor is that the configuration of PlaSim with the ML does not include an AMOC parameterization, so it cannot weaken or collapse with a cooling effect. Furthermore, when using a diffusive term in the ML with values of the horizontal diffusion parameter which allow for a realistic meridional temperature distribution in present-day experiments, changes in average sea ice area have a much stronger radiative impact compared to very low values of the diffusion coefficient or to using a Q-flux approach to represent transport. This fact reveals that sea ice feedbacks may be overestimated in the configurations using a ML with a diffusive transport parameterization. Since using a diffusive term may be preferable to a fixed flux correction in some cases for studying climate responses far from present-day conditions (such as paleoclimatic or exoplanetary studies), this impact may have to be taken carefully into account.

Chapter 6

Atlantic MOC variability

The Atlantic Meridional Overturning Circulation (AMOC) is one of the major ocean currents in the Atlantic Ocean. It transports warm and salty water from the tropics northward in the upper layers, balanced by a southward transport of cooler and deep water. Paleoclimate data and model simulations show that AMOC is continuously evolving and its regime transitions have a significant impact on the European and global climate. Recently, there has been an increasing interest in the study of the AMOC following the hypothesis that it has slowed down in the last century, a theory supported by paleoclimatic reconstructions (Rahmstorf et al., 2015) and recent direct observations (Robson et al., 2014). Therefore, climate research is currently focusing on the future behaviour of the AMOC and on the existence of associated tipping points, whose crossing could lead to abrupt and irreversible climate change. In some regions, particularly Europe, the impacts of AMOC decline have been recently analysed in a simulation ensemble from CMIP5 and CMIP6 and discussed in (Bellomo et al., 2021), a study in which I participated during my PhD period. In Section 3.2 I have explored some values of the oceanic vertical diffusion coefficient in PlaSim-LSG and showed how the model AMOC assumes different regimes depending on the chosen value (see Fig. 3.2). The model constitutes a simplified version of the real world, in which ocean phenomena such as thermohaline circulation and turbulent motions are represented by parameterizations. However, although the behaviour of the AMOC is determined by much more complex mechanisms in the real world, it may be useful for their understanding to identify the mechanisms linking the regimes of this part of the ocean circulation with other model variables.

6.1 AMOC regimes in PlaSim-LSG

To extend the results obtained in Section 3.2, I have explored the dependence of AMOC regimes on two parameters of PlaSim-LSG, the vertical oceanic

diffusion coefficient A_v and the atmospheric CO_2 concentration, analysing two sets of 2000-year simulations (Fig. 6.1): in the first set the atmospheric CO_2 is fixed to 285 ppm (pre-industrial level) and each run has a different A_v , which is varied only at the surface in the range from $0.1 \cdot 10^{-4} \text{ m}^2\text{s}^{-1}$ to $1.3 \cdot 10^{-4} \text{ m}^2\text{s}^{-1}$ (it is fixed to $1.3 \cdot 10^{-4} \text{ m}^2\text{s}^{-1}$ at the ocean bottom). In the second set the surface diffusion coefficient is fixed to $A_v = 0.8 \cdot 10^{-4} \text{ m}^2\text{s}^{-1}$ while the CO_2 concentration changes in the range from 114 ppm ($0.4x\text{CO}_2$) to 1140 ppm ($4x\text{CO}_2$). Different AMOC regimes for the same A_v or CO_2 value have been obtained starting from different initial conditions.

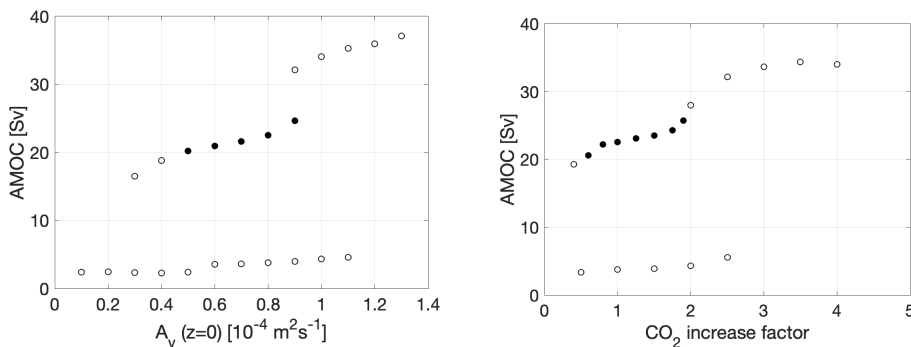


Figure 6.1: Different AMOC regimes in the PlaSim-LSG configuration as a function of the vertical oceanic diffusion coefficient A_v and of the atmospheric CO_2 concentration. Filled circles indicate the presence of AMOC oscillations.

Both sets of simulations show three different branches that correspond to very different AMOC regimes: a “weak” and flat branch lower than 5 Sv, an intermediate branch between 15 and 25 Sv, characterized by oscillations up to 10 Sv of amplitude and a multicentennial period, and a “strong” branch without oscillations, with values higher than 30 Sv. Among these three regimes, the intermediate one is certainly the most interesting because it recalls AMOC oscillations that have emerged from paleoclimatic studies and climatic simulations performed with other models. Therefore in Section 6.3 I have explored the AMOC oscillations in PlaSim-LSG in order to identify the mechanism from which they originate.

6.2 AMOC oscillations in paleoclimate data and model simulations

Mechanisms driving the low-frequency AMOC oscillations are of great scientific interest for our understanding of past and future climate. Paleoclimate records reveals phenomena of AMOC oscillations mainly associated to climate fluctuations that occurred during the Last Glacial Period and named

Dansgaard-Oeschger events (Dansgaard et al., 1993), which represent one of the most enigmatic examples of abrupt climate change. These events were characterized by rapid warming and more gradual cooling, with recurrence on a millennial scale. Given the lack of direct observations of AMOC over long timescales, its variability at climate timescales has been explored in several climate models. Models of various degrees of complexity, from simple box models to GCMs, simulate multiple timescale AMOC fluctuations, which can be generated spontaneously or driven with forcing fields. Mikolajewicz and Maier-Reimer (1990) found a 320-year timescale variability in the Large Scale Geostrophic (LSG) Ocean GCM in response to a freshwater forcing, with the strongest effect located around Antarctica. Broecker et al. (1990) introduced the salt oscillator hypothesis to explain the paleoclimatic Dansgaard-Oeschger events, proposing that the periodic shift between a strong and a weak thermohaline circulation in the Atlantic Ocean is controlled by the salt budget. Furthermore Birchfield and Broecker (1990) suggested that the proximity of melt water production to the North Atlantic Deep Water (NADW) region plays an important role in the salt oscillator. The mechanism observed in Mikolajewicz and Maier-Reimer (1990) was reconsidered in Winton and Sarachik (1993), who introduced the term *loop oscillator* and proposed that centennial oscillations are due to the interaction between the overturning circulation and the salinity boundary conditions. Pierce et al. (1995) used the same configuration of LSG described in Mikolajewicz and Maier-Reimer (1990) and found that a similar fluctuation in the Southern Ocean can be observed when random fluctuations are added to the freshwater flux that forces the model, but even with no imposed noise. More recently, Peltier and Vettoretti (2014) explored asymmetric oscillations of the AMOC which occur in the Community Earth System Model version 1 (CESM1; Gent et al. (2011)) under glacial climate conditions. The authors explained the Dansgaard-Oeschger events with the *kicked salt oscillator*, in which a Heinrich event (natural phenomenon in which groups of icebergs break off from glaciers, traverse the North Atlantic (NA) and melt, altering the thermohaline circulation) is seen as providing the “kick” which induces the oscillatory behaviour. The proposed mechanism is of relaxation oscillator form, where the fast rise of AMOC is followed by a slow relaxation back toward glacial conditions, based on changes of the meridional salinity gradient between the subtropical gyre of the NA and the region beneath the sea ice lid. This mechanism was further explored in Vettoretti and Peltier (2018), who demonstrated that the Dansgaard-Oeschger events involve a displacement of sea ice from the Arctic and the associated freshwater input as it reaches the NA. Although it is clear that salinity transport plays a crucial role in generating AMOC oscillations, geographical regions involved in salinity exchanges remain uncertain. Some studies argued that salinity anomalies are produced in the subtropical zone (Vellinga and Wu, 2004; Peltier and Vettoretti, 2014) or suggested a connection between NA and Southern Ocean (Park and Latif,

2008; Delworth and Zeng, 2012). Other papers demonstrated that salinity anomalies are originated in the Arctic Ocean and then advected to the NA (Jungclaus et al., 2005; Jiang et al., 2021). In particular, Jiang et al. (2021) investigated centennial AMOC variability emerging in the Institute Pierre Simon Laplace (IPSL; Boucher et al. (2020)) atmosphere-ocean model and showed that oscillations are driven by sea ice transport from the Arctic to the NADW region, where it melts. Similar oscillations are observed in pre-industrial simulations in the Earth-system model EC-Earth 3 (Döscher et al., 2021), which has the same oceanic component (Nucleus for European Modelling of the Ocean, NEMO; Madec and Team (2012)) as IPSL. Given the great interest in AMOC oscillations, it is useful to explore them also in PlaSim-LSG to clarify the mechanisms involved, bearing in mind that they may be specific for this model.

6.3 AMOC oscillations in PlaSim-LSG

The AMOC oscillations have been explored in a 4000 year long run with PlaSim-LSG T21, using dynamic sea ice and the vertical diffusion coefficient profile suggested by Sciascia (2008), with a surface value of $A_v = 0.8 \cdot 10^{-4} \text{ m}^2\text{s}^{-1}$ and a bottom value of $A_b = 1.3 \cdot 10^{-4} \text{ m}^2\text{s}^{-1}$ (for reference, see Table 3.1 and green lines in Fig. 3.2). A pre-industrial atmospheric CO_2 concentration has been fixed (this is the only difference from the run 3 described in Section 3.2). Figure 6.2 shows the time series of the maximum AMOC computed between $46\text{-}66^\circ\text{N}$ and below 700 m for this simulation, where the black line represents a moving mean calculated over a sliding window of length 31 years and superimposed to the original output in grey. After about 1000 years, the model presents AMOC oscillations, rather symmetric and regular, with a mean amplitude of 2.3 Sv and a mean period of 265 years.

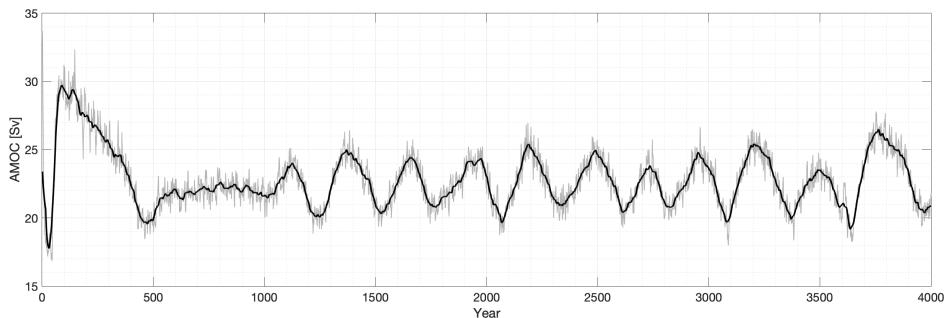


Figure 6.2: AMOC oscillations obtained with the PlaSim-LSG model under a certain range of parameters.

In order to investigate the geographic area where oscillations are generated, I have also analysed the maximum of thermohaline circulation in the SH (30°S), respectively in the Atlantic and Pacific basin (not shown). In the Atlantic Ocean oscillations are still present but with a small amplitude, while in the Pacific Ocean this AMOC multicentennial variability is absent, confirming that the observed phenomenon is mainly located in the NA. This result will be confirmed by the following analyses and allows to neglect the role of the Southern Hemisphere and Antarctic sea ice in the description of the oscillation, as well as the concept of *bipolar seesaw*. This mechanism is the most likely hypothesis regarding the Dansgaard-Oeschger events and consists of an anti-phase relationship between the Greenland and the Antarctic temperatures (Knutti et al., 2004). Figure 6.3 compares the near-surface air temperature in the Arctic and Antarctic regions and confirms that there is no correlation ($\rho = 0.24$) between the two time series, thus excluding a typical Dansgaard-Oeschger mechanism. Bearing in mind the results of Chapter 4 on the PlaSim-LSG configuration, maybe a bipolar seesaw in this model cannot take place due to incorrect representation of temperature and sea ice in the SH.

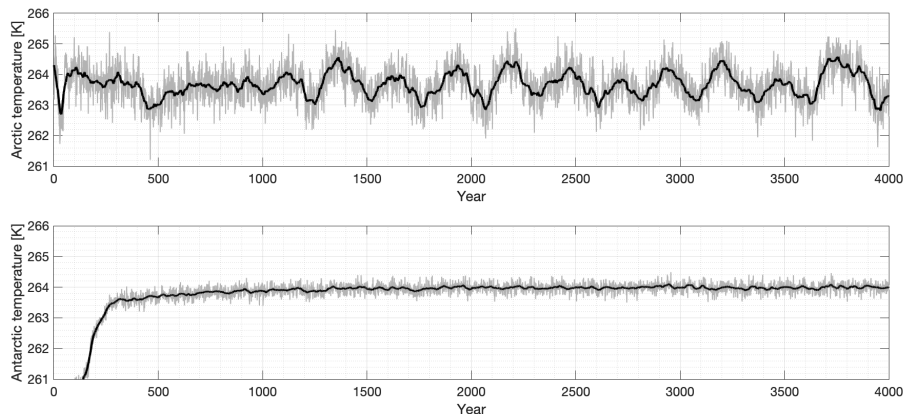


Figure 6.3: Time series of near-surface air temperature in the Arctic (60-90°N) and Antarctic (60-90°S) regions. The black lines represent a moving mean calculated over a sliding window of length 31 years and superimposed to the original output in grey.

The following analyses have been carried out on the ten complete oscillations between years 1250-3971 and for each oscillation four phases of arbitrary length of 11 years have been identified: the minimum of AMOC (phase 1), the phase of increase in which the AMOC assumes an intermediate value between the previous minimum and the following maximum (phase 2), the maximum of AMOC (phase 3) and the phase of decrease, computed as the average value of the AMOC between the previous maximum and the

following minimum (phase 4). To understand the mechanism associated with AMOC oscillations, I have started from the analysis of salinity, which in previous studies has been shown to be directly involved in the variability of the NA. Following Peltier and Vettoretti (2014), Fig. 6.4 shows for each phase sections of composite zonally-averaged salinity anomalies, computed with respect to the mean over the whole simulation (ten oscillations) and averaged over all the years belonging to the specific phase. Anomalies have been computed by selecting the Atlantic and Arctic oceanic basins and the salinity climatology has been superimposed on the anomalies. The stippling indicates areas where more than 80% of the oscillations agree on the sign of the change, following the IPCC Technical Summary (Solomon et al., 2007) method with a lower percentage due to the small number of members. During phase 1, most of the ocean at high latitudes is characterized by a negative salinity anomaly, with the lowest values located at the surface between 55 and 65°N. During phase 2, the Arctic basin is characterized by a positive salinity anomaly that is distributed rather uniformly at all depths. In phase 3 and phase 4 the anomalies are reversed with respect to phase 1 and phase 2, respectively. The uniform vertical distribution of anomalies can be attributed to the very high vertical diffusion coefficient when compared to that suggested by Bryan and Lewis (1979). Another important aspect that emerges from this figure is the role of bathymetry, which between 60 and 70°N is an obstacle for the diffusion of salinity in the deeper layers.

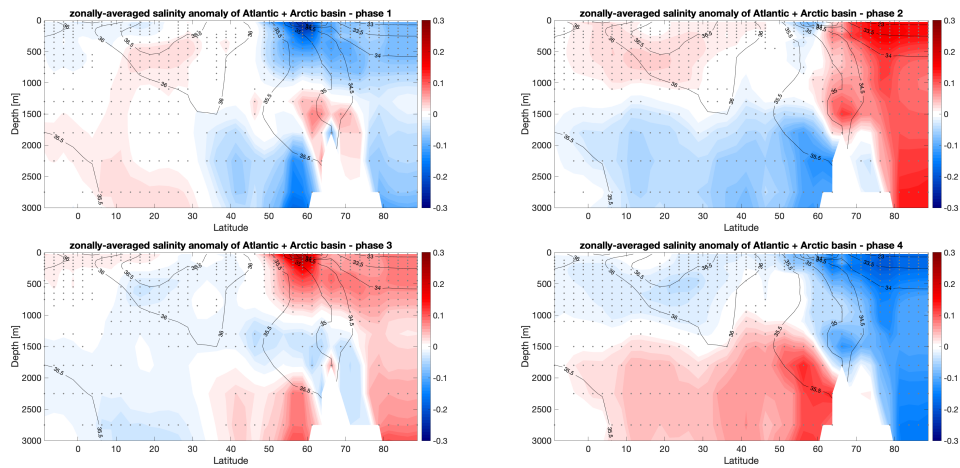


Figure 6.4: Zonally-averaged salinity anomalies (in psu) of the Atlantic and Arctic basin for different phases of AMOC oscillations, computed as the deviation from the time mean between years 1250 and 3971 of the simulation. The stippling indicates areas where more than 80% of the oscillations agree on the sign of the change.

Additional information on the horizontal distribution of the anomalies can be obtained from Fig. 6.5, which shows the climatology of surface salinity, sea ice cover and evaporation and the respective anomalies associated with the four phases of the oscillations. When AMOC is at minimum (phase 1), the NA and the Arctic have a lower than average salinity, with the minimum located south of Greenland, the sea ice cover is high and the evaporation is reduced especially in the Labrador Sea (where the model never forms sea ice, as observed from the climatology) and south of Greenland. The reduced evaporation is associated with a negative temperature anomaly in that area due to weak AMOC bringing less heat from the equator towards the pole. When the AMOC is increasing (phase 2), some areas are still characterized by anomalies similar to those in phase 1, while other areas already show anomalies of opposite sign. In particular, in the Labrador Sea and south of Greenland, salinity and evaporation are increasing (although still below the average) and therefore are in phase opposition with AMOC. On the contrary, in the region between Iceland, United Kingdom and Scandinavian Peninsula, salinity and evaporation anomalies are at maximum, and therefore not in phase with AMOC. This region is located at the edge of sea ice, whose extent is reduced from phase 1 to phase 2: a portion of the ocean previously covered by ice remains uncovered, therefore the evaporation increases. As a result, salinity increases and spreads rapidly to surrounding areas, especially in the Arctic Sea. When AMOC is maximum (phase 3), all variables show a pattern of anomalies similar to that of phase 1 but with opposite sign: salinity is maximum especially south of Greenland, both for local effects associated with AMOC and for diffusion from high latitudes, while west of the Scandinavian Peninsula the salinity has started to decrease again due to the increase of ice inhibiting evaporation. During the weakening of AMOC (phase 4), the sea ice cover west of the Scandinavian Peninsula reaches its peak, evaporation is hindered by the presence of ice and therefore a region of freshwater is formed, which spreads rapidly throughout the Arctic.

The most curious feature that emerges from this figure is the phase opposition between salinity and sea ice cover. The model seems not to respect the relationship between these two variables related to brine rejection, the process that occurs when salt is expelled as a result of sea ice formation, making the underlying water saltier. This phenomenon plays a fundamental role in the oscillations of AMOC in IPSL (Jiang et al., 2021), where salinity anomalies instead have the same sign as sea ice anomalies. The current version of PlaSim-LSG contains a parameterization for brine rejection that is not used by default. By adding the brine rejection to the model (not shown) the oscillations have a smaller amplitude but the mechanism described in Fig. 6.5, in which sea ice formation prevents evaporation and thus salinity decreases, still prevails. This may indicate an incorrect or insufficient description of brine rejection in PlaSim-LSG.

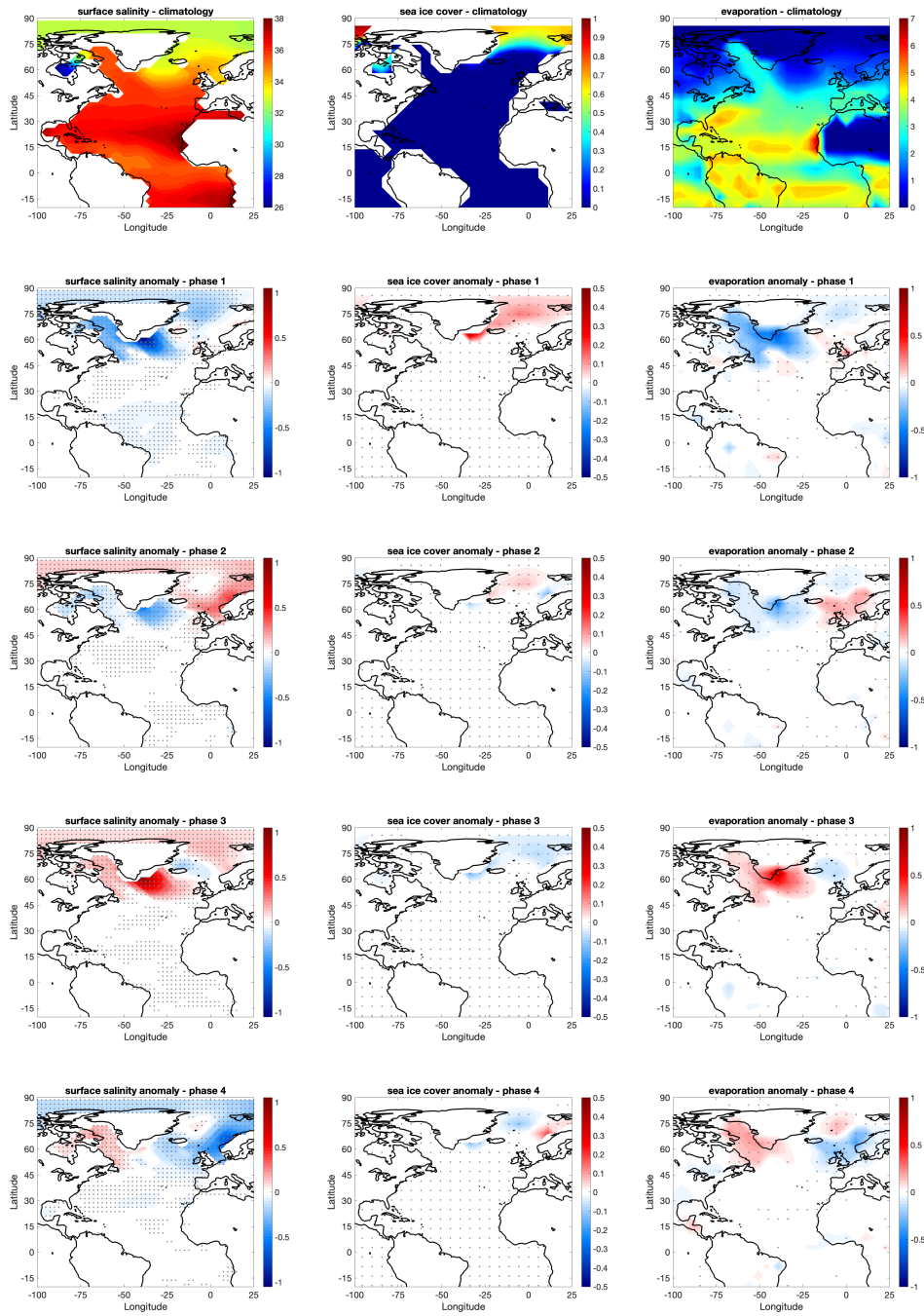


Figure 6.5: Surface salinity (in psu), sea ice cover and evaporation (in mm/day) climatology and anomalies for different phases of AMOC oscillations. The stippling indicates areas where more than 80% of the oscillations agree on the sign of the change.

To investigate variations in time, I have analysed Hovmöller diagrams for sea ice cover, salinity and potential temperature anomalies as functions of time and latitude averaged over the longitudinal band of the Atlantic Ocean and over the first 1000 m of depth (Fig. 6.6). All the variables show an oscillatory pattern where positive and negative anomalies alternate with the same period of AMOC, as already observed in Fig. 6.5, although the Hovmöller diagrams do not allow to highlight the anomalies of opposite sign that coexist between 50 and 70°N in phases 2 and 4 because they include zonal averages. Fig. 6.6 provides further evidence that the Tropics are not significantly involved in this mechanism because anomalies between 50 and 90°N are stronger than those at low latitudes. The fundamental role of the Arctic Ocean is clearly revealed by the shift of salinity anomalies from high to mid-latitudes in a few decades (from phase 2 to phase 3 and from phase 4 to phase 1), indicating a transport of more or less salty water from north to south. The Hovmöller diagram of potential temperature has a less regular pattern of anomalies than sea ice cover and salinity.

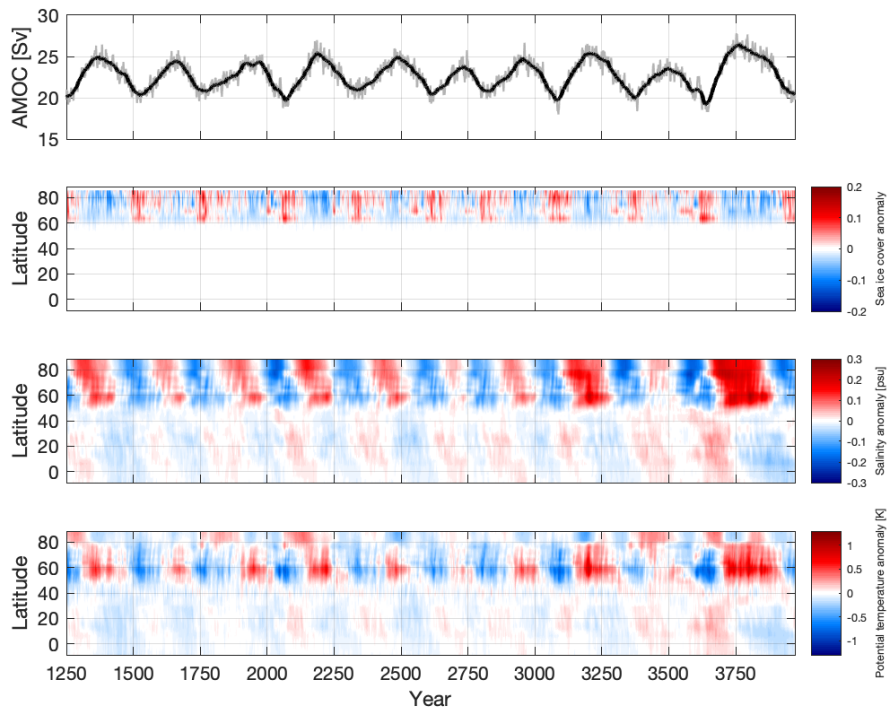


Figure 6.6: Maximum AMOC computed between 46-66°N and below 700 m (grey line) and moving average of AMOC over a sliding window of 31 years (black line). Time versus latitude Hovmöller diagram of sea ice cover, salinity (in psu) and potential temperature anomaly (in K), averaged over the longitudinal band corresponding to the Atlantic Ocean and over the first 1000 m of depth.

The fundamental role of the Arctic Ocean in the mechanism that generates the AMOC oscillations can be better understood in Fig. 6.7, which shows the lagged regression maps on AMOC (for some representative lags) of surface salinity, sea ice volume (computed as the product of sea ice cover and thickness), sea ice cover, evaporation and near-surface air temperature. Please notice that the polar projection provides a more complete spatial representation of the Arctic than Fig. 6.5 and 6.6, where anomalies are represented up to 90°N only in the longitudinal band of the Atlantic Ocean. Maximum of AMOC occurs at lag 0 years, while minima at about lag -130 and +130 years. As noted above, the variables in the region south of Greenland are perfectly in phase with AMOC: at lag 0 years we observe a maximum of surface salinity, evaporation and temperature and a minimum of sea ice. The signs are opposite in correspondence of the AMOC minima. In the Arctic basin and in the region between Iceland and Scandinavian Peninsula, however, the salinity maximum and the sea ice minimum occur at about lag -30 years, anticipating the maximum of AMOC by about 30 years. This means that when AMOC is still increasing between lag -30 and lag 0, the salinity at high latitudes already starts to decrease and the sea ice starts to increase. The regression maps also clearly show the movement of salinity anomalies already described in the previous figures: at lag -120 the positive salinity anomaly occupies only the portion of the Arctic Ocean between Europe and Greenland, in the following lags this salt water spreads throughout the Arctic and south of Greenland, superimposing to the local formation.

Based on these figures and on the previous observations, it is possible to make an hypothesis on the mechanism generating the oscillations in PlaSim-LSG. Please consider the situation of phase 3 (see Fig. 6.4 and 6.5) and lag 0 years (see Fig. 6.7). This phase corresponds to a maximum of AMOC, so the heat transport from the equator to the poles is very intense, therefore the temperatures in the NA and in the Arctic Ocean are high and the sea ice cover is below the average value. At this point, the classical self-regulation mechanism of AMOC is triggered: the pole-to-equator temperature gradient is low and therefore the AMOC starts to weaken. It is important to notice that the sea ice in the Arctic basin does not reach the minimum when the AMOC is at maximum (lag 0 years) but at previous lags (at about lag -30 years): when the AMOC reaches the maximum, sea ice has already started to increase again. Although the sign of the anomaly is still negative, from lag -30 to lag 0 years sea ice increases, covering an increasingly larger area of the oceanic region between Russia, Norway and Greenland. The presence of sea ice prevents evaporation, which decreases especially between Iceland and the Scandinavian Peninsula. Consequently, the reduction of evaporation causes an increase in freshwater, which is observed east of Greenland from lag -30 to lag 0 years. At following lags, this salinity anomaly begins to spread in the surrounding areas, superimposing to local effects. When the freshwater

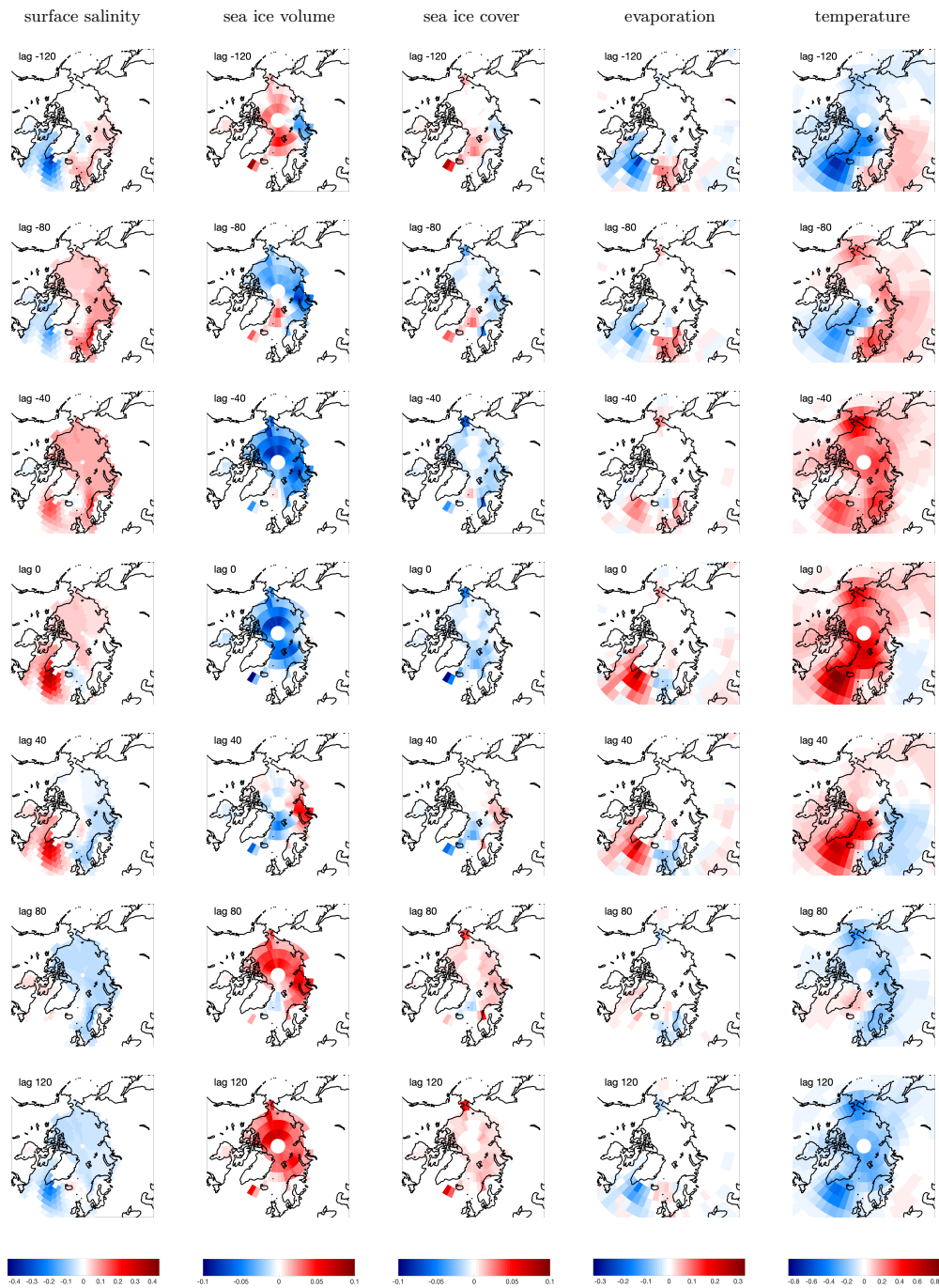


Figure 6.7: Regression on AMOC of surface salinity anomaly (in psu), sea ice volume (in m) and cover, evaporation (in mm/day) and near-surface air temperature (K). The lag is positive when the AMOC leads.

anomaly reaches the region of NADW formation south of Greenland, it provides an additional "kick" to the AMOC that was already decreasing by self-regulation. Therefore the AMOC exceeds the equilibrium state (where it would stop if the feedback associated to temperature gradient was the only mechanism involved) and reaches the minimum (phase 1 in Fig. 6.4 and 6.5, lag +130 years in Fig. 6.7). At this point the mechanism is repeated with opposite sign: the high pole-to-equator temperature gradient leads to a strengthening of AMOC, increased temperatures and sea ice melting. The reduction of sea ice facilitates evaporation and a positive salinity anomaly is formed in the Arctic Ocean. The salinity anomaly reaches the NADW region after a few decades and leads to a further strengthening of the AMOC, which overcomes its equilibrium state and reaches the maximum.

6.4 Concluding remarks

The AMOC oscillations in PlaSim-LSG presented in this chapter show very different characteristics compared to those in the IPSL model recently analysed in Jiang et al. (2021). The first fundamental difference in the two models is the relationship between sea ice and salinity in the Arctic basin, as described in Section 6.3: in IPSL the respective anomalies have the same sign because they are linked by the process of brine rejection, while in PlaSim the mechanism involves evaporation, which determines a phase opposition between sea ice and salinity. As a consequence, an important aspect that differentiates the two models is the phase relationship between salinity and AMOC: in IPSL, when AMOC reaches its maximum, the Arctic sea ice area and salinity are at a minimum while salinity around Greenland has just started to decrease (see Fig. 6.8 from Jiang et al. (2021)); in PlaSim-LSG, the maximum of AMOC corresponds to a maximum of salinity south of Greenland while in the Arctic salinity has already started to decrease and the sea ice to increase. These observations are sufficient to understand that the mechanisms governing AMOC oscillations in IPSL and PlaSim-LSG are deeply different, although with some similarities such as the fundamental role of the freshwater holding capacity of the Arctic basin (the ability to maintain the salinity anomaly instead of dispersing it) and delayed exchanges with the NA. However, even in this aspect there seems to be a fundamental difference: while in IPSL salinity anomalies propagate from the Arctic to the NA through transport of sea ice, which melts and releases freshwater when moving towards lower latitudes, in PlaSim-LSG a direct advection of salt from the Arctic to the NADW formation region occurs (the default version of the model does not contain sea ice motion). More work is still needed to further investigate the formation of salinity anomalies and their transport from high to middle latitudes in PlaSim-LSG, for example by means of salinity budgets in some oceanic regions. The period of oscillation is determined by the time

required for exchanges between the Arctic basin and the NA: in IPSL, the first 1000 years show a variability with a period of about 200 years and the last 1000 years have a less regular variability, while in PlaSim-LSG the oscillations are regular with an average period of 265 years. This chapter has revealed that the formation and melting of Arctic sea ice play a fundamental role in the oscillatory phenomenon simulated by the model. This result is confirmed by simulations with a fixed sea ice cover that have been described in Chapter 5. In fact, when Arctic sea ice is prescribed and therefore it does not depend on temperature changes, the AMOC of the model does not exhibit oscillations. Based on this idea, several simulations can be performed by turning off a component or a process, in order to study its contribution to the mechanism of the oscillations. Intermediate complexity models like PlaSim are an ideal tool for performing this type of experiments, because they involve a simplified parameterization of the climate system and allow to separate the role of the different components in a simpler way than GCMs. In the study of AMOC oscillations it is important to be cautious and consider that they may be specific mechanisms of some climate models, which may not be reflected in reality. In the case of PlaSim-LSG, the over-simplistic bathymetry must be taken into account: due to the coarse resolution, for example, the Canadian Arctic Archipelago is represented by a continuous strip of land connecting Canada with Greenland, therefore the Arctic and Atlantic Oceans only communicate east of Greenland. Furthermore, as we have seen at the beginning of this chapter, the oscillations in PlaSim-LSG occur only for a certain range of parameters that often, as in the case of the vertical oceanic diffusion coefficient, are very simplified representations of the real physical phenomenon. However, it is important to explore and document this mechanism which, although occurring in an EMIC such as PlaSim-LSG, has several aspects in common with similar studies involving more complex climate models and types of variability that have characterized past climate.

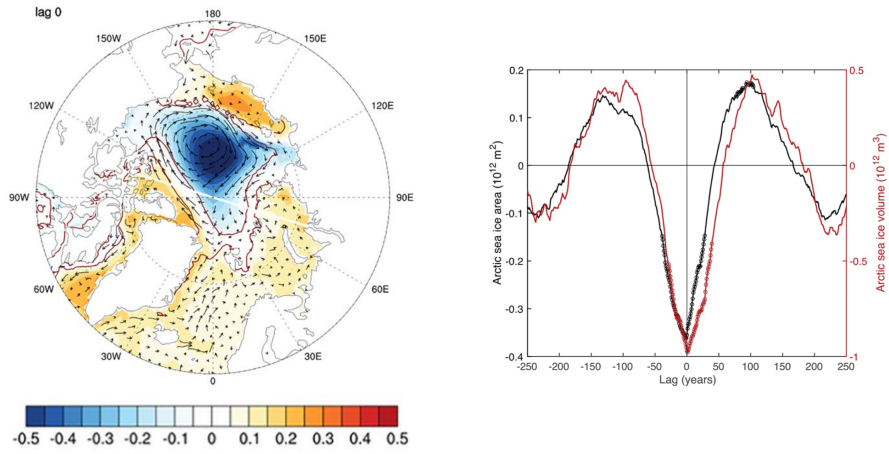


Figure 6.8: Regression on AMOC low frequency first component of the top 150 m salinity (colors, in psu) at lag 0 and lagged regression of Arctic sea ice area and volume in IPSL (Jiang et al., 2021).

Chapter 7

The ENSO teleconnection to the North Atlantic

In Chapter 6 I have explored the centennial-scale variability that emerges for a certain range of parameters in the PlaSim-LSG model and that mainly affects the North Atlantic (NA) region. This chapter instead presents a study of the variability on a shorter (interannual) timescale: the extra-tropical response to El Niño-Southern Oscillation (ENSO) in PlaSim, also in this case with a focus on the NA region. Observational datasets show that the strongest extra-tropical signal related to ENSO has been detected in the North Pacific, however in the NA a modest ENSO signal in late winter (January, February, March - JFM) has been found (Brönnimann, 2007). Since the sea level pressure (SLP) pattern generated by the NA response to ENSO is similar to that associated with the North Atlantic Oscillation (NAO), the two variability patterns could be associated. However, Mezzina et al. (2020) have shown that the atmospheric response to ENSO in the NA region and the NAO originate from different dynamics and they are not physically connected. For completeness of information, before presenting the study carried out with PlaSim to explore the extra-tropical response to ENSO, I have decided to include a section presenting the signal related to the NAO in the model.

7.1 The leading mode of variability in the North Atlantic: the NAO

The North Atlantic Oscillation is the most evident and recurrent pattern of atmospheric variability in the middle and high latitudes of the NH, especially during the boreal winter. It consists of an atmospheric mass exchange between the Icelandic Low and Azores High, where large variations in wind speed and direction, heat and humidity transport occur (Hurrell et al., 2003). The NAO is mainly an internal mode of atmospheric variability, as demonstrated

by climate simulations that do not include variations in SST, sea ice or land surface. Among several ways to define and calculate the NAO, the most used is the empirical orthogonal functions (EOFs) technique. Using this approach, the NAO is defined as the leading eigenvector of the autocovariance matrix of SLP.

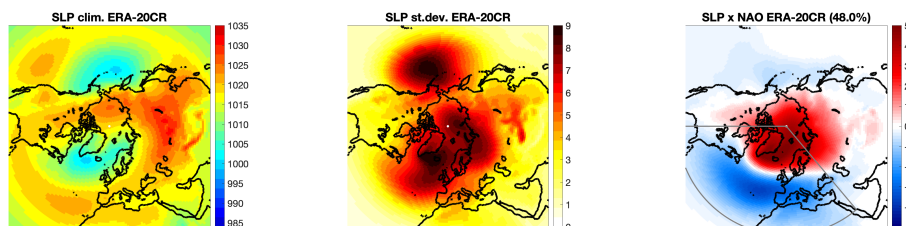


Figure 7.1: Maps in JFM using ERA-20CR (1900-2010): sea level pressure climatology and standard deviation (in hPa), sea level pressure regressed onto the NAO index (in hPa).

The first two panels in Fig. 7.1 show the climatology and the standard deviation of SLP computed for late winter (JFM) from the ERA-20CR reanalysis dataset (Poli et al., 2016). The choice of the months has been based on the purpose of this section of the thesis, that is to show and compare the main pattern of variability in the NA with the response to ENSO, which is particularly robust in late winter over this region (Brönnimann, 2007). The climatology shows the mean state of SLP which allows to identify the semi-permanent pressure systems at high and middle latitudes of the NH: the Siberian and Azores high-pressure centres, the Aleutian and Icelandic low-pressure centres. In the NA sector, the counterclockwise air flows associated with the low-pressure system and the clockwise air flows associated with the high-pressure system are linked to the position of the “jet stream”. The middle panel of Fig. 7.1 shows zones of high variability, among which three maxima can be identified near the Aleutian Low, the Icelandic Low and north of Siberia. The NAO spatial signature is obtained by computing the linear regression of SLP onto the NAO index. The NAO index is defined as the first principal component (PC) of SLP calculated over the sector 20°-90°N / 90°W-40°E (gray lines in Fig. 7.1) and it is shown here for the negative phase of the NAO. This reanalysis dataset shows that the NAO contributes for 48% to the total variability of SLP in the NA. The NAO is characterized by a dipole of SLP anomalies in the north-south direction: in the negative phase, the combination of a positive anomaly in the Arctic region and a negative anomaly south of 50°N is related to a decrease in the meridional pressure gradient and consequently a weakening of surface westerlies. The positive phase of the NAO, on the contrary, strengthens the semi-permanent pressure systems in the NA, generating stronger surface westerlies at mid-latitudes. Spectral analysis studies have shown that NAO variability is observed over a

wide range of timescales.

The representation of the NAO in PlaSim has been analysed using two simulations that have been originally performed for the study of the ENSO teleconnection and therefore will be presented also in the next Section (7.2). They consist of two 505 year-long atmosphere-only simulations performed with the two horizontal resolutions of the model (T21 and T42), in which the boundary conditions have been defined by prescribing a climatology of SSTs and sea ice cover relative to the period 1981-2010 (HadISST2.2; Titchner and Rayner (2014)). The atmospheric CO₂ level has been fixed at the 1990 value, as described above for model tuning experiments. The top panels of Fig. 7.2 show the SLP climatology averaged over the last 500 years of each simulation (the first 5 years were not considered to ensure the removal of spin-up), while the bottom panels show the differences in SLP between PlaSim and the reanalysis, which was shown in the first panel of Fig. 7.1.

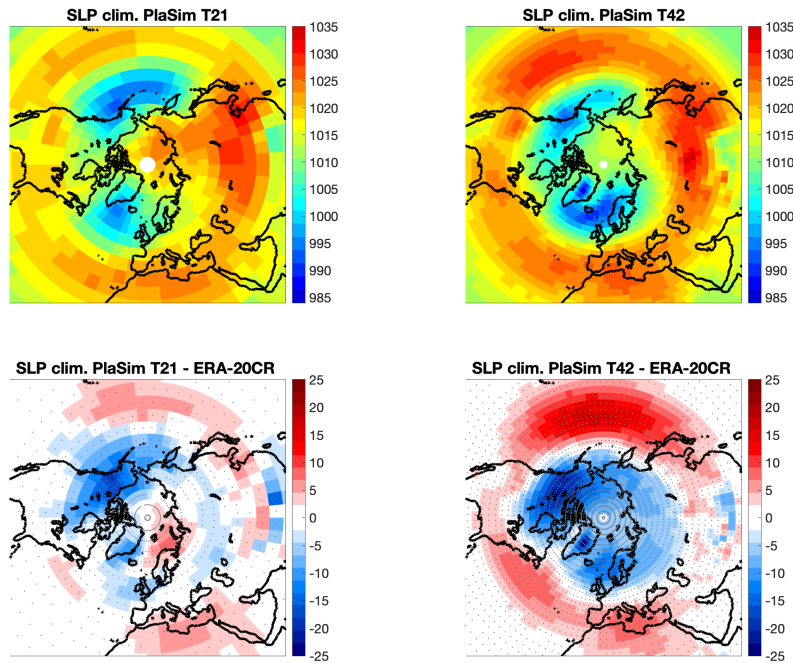


Figure 7.2: Sea level pressure climatology (in hPa) in JFM using T21 and T42 resolution, respectively (top panels). Sea level pressure difference in JFM with respect to ERA-20CR (1900-2010) (bottom panels). Stippling indicate statistically significant areas at 95% confidence level.

From the comparison between the first panel of Fig. 7.1 and Fig. 7.2 we can notice that in general the SLP climatology is better reproduced using the resolution T21, both in terms of intensity and location of the pressure centres. In particular, T42 tends to amplify the maxima and minima of SLP. Maps of SLP differences (Fig. 7.2, bottom) show overall more cyclonic circulation at high latitudes, especially over Alaska and west of Canada, and more anticyclonic circulation at mid-latitudes, particularly in PlaSim T42. In this model configuration, the low-pressure system in the Pacific Ocean is located further north than the Aleutian Low in the reanalysis, while around 40°N there is a high-pressure center almost as strong as the Siberian high-pressure system, much less developed in reanalysis and in PlaSim T21. In the Atlantic Ocean, the meridional pressure gradient is more intense in PlaSim (especially at T42 resolution) and therefore the surface westerlies are expected to be more intense than the observed ones. In addition to the SLP pattern, the climatology of the two resolutions of the model presents other important differences that are presented and discussed in Section 7.4. The differences in SLP at high latitudes are consistent with the strength of zonal winds (shown in Fig. 7.7) because due to geostrophic balance the westerlies are more intense where the meridional pressure gradient is larger, as in the T42 resolution.

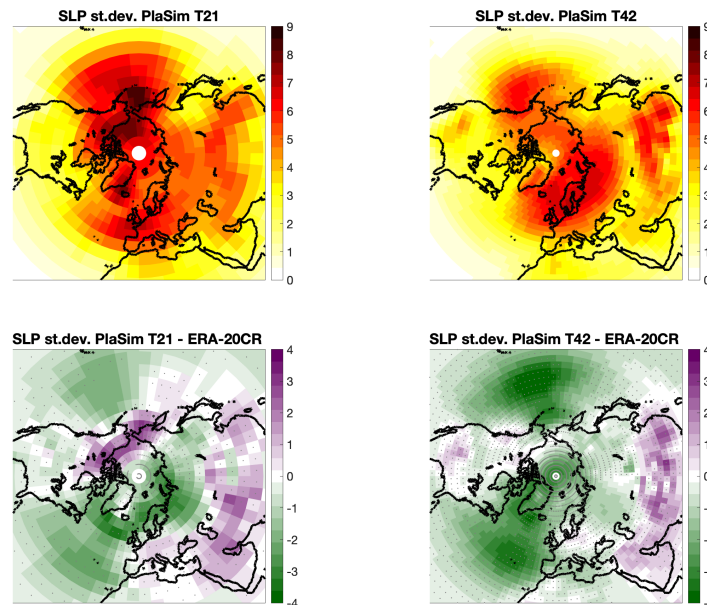


Figure 7.3: Sea level pressure standard deviation (in hPa) in JFM using T21 and T42 resolution, respectively (top panels). Difference of sea level pressure standard deviation in JFM with respect to ERA-20CR (1900-2010) (bottom panels). Stippling indicate statistically significant areas at 95% confidence level.

Figure 7.3 shows the standard deviation of SLP in PlaSim T21 and T42 (top panels) and their differences with respect to ERA-20CR (bottom panels). Comparing the Fig. 7.3 with the central panel of Fig. 7.1, it shows that the SLP variability in the model is almost everywhere smaller than the observed one, especially over the oceans, except at mid-latitudes over the Asian continent and the Bering Strait (only in PlaSim T21).

Finally, I have computed and represented in Fig. 7.4 the NAO pattern in PlaSim T21 and T42, using the same method as described above for the representation of the NAO in Fig. 7.1. The first fundamental information that emerges from the comparison between the model and the reanalysis is the difference in terms of variability associated with the NAO. In fact, not only the model has a very different percentage of variance explained by the NAO with respect to reanalysis, but it also shows a large difference between T21 resolution (60%) and T42 resolution (34%). In terms of intensity, the SLP anomalies corresponding to the negative phase of the NAO are similar to reanalysis in PlaSim T21, while in PlaSim T42 the signal is weaker. Comparing instead the location of the characteristic dipole of the NAO, we can observe that the minimum corresponding to the negative pole is located further east (closer the continent) than in the reanalysis, in both model resolutions. Instead, the location of the maximum properly corresponds to that of the observed pattern, but the positive anomaly in PlaSim T42 is limited to the portion of the Arctic between 60 and 150°W while in PlaSim T21 and ERA-20CR it is zonally distributed in a more uniform way.

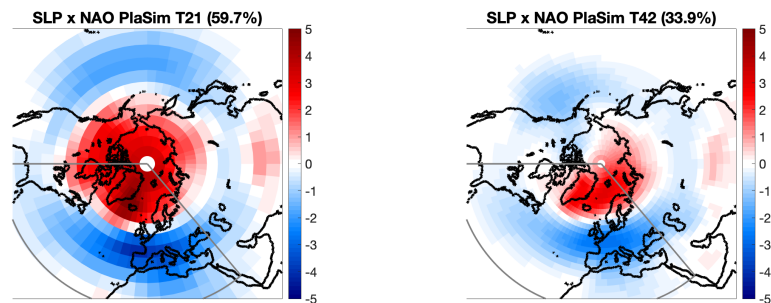


Figure 7.4: Sea level pressure regressed onto the NAO index (in hPa) in JFM in PlaSim T21 and PlaSim T42.

Therefore, in general the model is able to reproduce both the SLP field and the NAO pattern over the NA sector, although the comparison highlights some important differences between PlaSim T21 and T42, and also with respect to the observations. This analysis also provides further evidence that the existence of the NAO is independent on the atmosphere-ocean interaction, since its pattern of variability is observable even in simulations involving only the atmospheric module of PlaSim.

7.2 The leading mode of variability of the tropical ocean-atmosphere system: the ENSO phenomenon

El Niño-Southern Oscillation (ENSO) is a variability mode of the tropical ocean-atmosphere system in the Pacific Ocean and coupled to the global circulation (Hartmann, 2016). The term “El Niño” refers to the ENSO phase characterized by positive SST anomalies, which have been first recorded at irregular intervals on the west coast of South America during the Christmas period by fishermen, starting from the seventeenth century. Consequently, the opposite ENSO phase, characterized by negative SST anomalies in the same region, is conventionally called “La Niña”. The term “Southern Oscillation” refers instead to the atmospheric component of ENSO, characterized by a see-saw of SLP between the tropical central Pacific and the Indonesian Archipelago. Due to the strong interaction between the ocean and the atmosphere in the tropics, El Niño/La Niña and the Southern Oscillation are strongly coupled.

Under normal conditions, the coupled atmosphere-ocean system in the tropical Pacific Ocean is described by the middle panel of Fig. 7.5 from Hartmann (2016). The depth of the thermocline is higher in the west, where the mixed layer is warmer, and lower in the east, where the thin mixed layer is colder due to the upwelling that carries cold water to the surface. This zonal difference is mainly maintained by easterly winds in the equatorial Pacific, which are supported by upward convective motions over Indonesia and downward motions around 60°W. The atmospheric circulation is then closed by an eastward atmospheric flow in the upper troposphere and the resulting zonal circulation is called “Walker circulation”. This circulation is characterized by irregular SLP fluctuations between the western and eastern tropical Pacific.

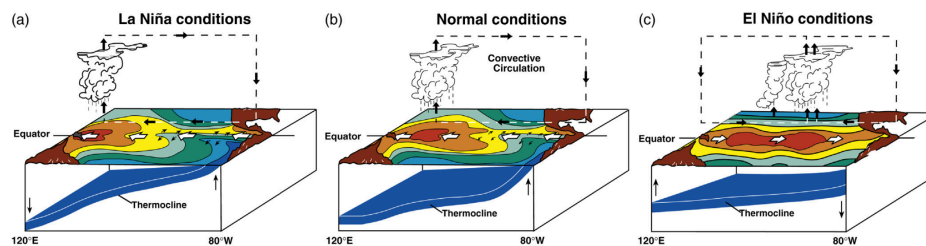


Figure 7.5: Schematic diagram showing the atmospheric and oceanic conditions along the equator in (a) La Niña, (b) normal, and (c) El Niño conditions (Hartmann, 2016).

The so-called La Niña phase (represented in the first panel of Fig. 7.5) consists of an intensification of the normal conditions described above: the slope of the thermocline in the equatorial Pacific is higher, the zone of strong convection and the maximum of SSTs are located more to the west while temperatures in the eastern Pacific are lower. On the contrary, the El Niño phase (last panel in Fig. 7.5) is characterized by a flatter thermocline and a smaller zonal gradient of SSTs: positive anomalies in central and eastern Pacific can reach up to 5°C locally, the convection zone is shifted further east and easterly winds are weaker than normal conditions. In this phase, a positive feedback first described by Bjerknes plays a fundamental role: when warm water flows towards the eastern Pacific and consequently the zonal gradient of SSTs is reduced, for example due to a decrease in the slope of the thermocline, the easterly winds weaken and further amplify the initial perturbation. Anomalies continue to increase until a negative feedback, such as that related to the thermocline depth adjustment, overwhelms the positive feedback. These negative feedbacks have a delayed response with respect to the initial perturbation related to SSTs and wind, and this allows the development of irregular oscillations characterizing the phenomenon (Goosse et al., 2010). The main consequences of El Niño events include droughts in Indonesia and Australia and increased rainfall in the central Pacific, the Gulf of Mexico and the equatorial coast of South America between November and March, while from May to September there is a reduction in summer monsoons in India. The opposite impacts are typically observed during La Niña events. Generally, the periodicity of ENSO is estimated by analysing the power spectrum of the so-called Niño-3 index, computed as the average of the SST anomalies over the region 5°S - 5°N / 90° - 150°W . From the power spectrum it emerges that the dominant range for the ENSO period is around 3 to 5 years, but significant variability extends from 2 to 20 years.

7.3 The impact of ENSO on the Northern Hemisphere

The ENSO effects are transmitted to other regions of the world through large-scale atmospheric circulation changes, with significant impacts on climate and ecosystems (Deser et al., 2017). The dynamical processes governing the extra-tropical response to ENSO have been and are still under investigation because its predictability has important environmental, economic and social consequences. The main difficulties in studying this response are due to the presence of an unpredictable internal atmospheric variability, which exists even in absence of ENSO and generates large differences in pattern and amplitude between individual ENSO events. However, it has been shown that if the number of analysed ENSO events is sufficiently large, the noise associated with this internal variability can be minimized, the interevent

variability decreases and the forcing associated with ENSO emerges (Deser et al., 2017). The ENSO teleconnection can be simply explained as follows: SST anomalies in the tropical Pacific are associated with anomalous diabatic heating in deep convection, which is reflected in a divergence anomaly in the upper troposphere. This represents a forcing of Rossby waves that propagate towards the pole and are influenced by interaction with the mean flow, which determines their path. In addition, coupling between the troposphere and the stratosphere can also play a role. The ENSO-driven circulation pattern modifies the atmospheric fields (e.g. temperature, humidity, distribution of clouds) even far from the equatorial Pacific, which in turn have an effect on the ocean (e.g. temperature, salinity, mixed-layer depth) (Deser et al., 2010). The extra-tropical response to ENSO in the NH consists of an anomalous regional pattern over the North Pacific-America that extends into the North Atlantic-Europe, including changes in the location and amplitude of subtropical and mid-latitude jet streams. During El Niño events, a similar (but not identical) pattern to that of the negative phase of the NAO develops in the NA, with a positive anomaly of high pressure at high latitudes and a negative anomaly of low pressure at mid-latitudes, as well as a shift of the storm track. However, it is incorrect to identify the extra-tropical response to ENSO with the NAO, as demonstrated by Mezzina et al. (2020). As reported by Brönnimann (2007), the literature suggests that the most appropriate period to study the NA and European response to ENSO is between January and March (JFM, late winter). The “canonical” El Niño late-winter signal in Europe is represented in Fig. 7.6 by means of composite anomaly maps of SLP, temperature and precipitation for strong El Niño events. The main features of this canonical signal are (top panel) positive SLP anomalies from Iceland to Scandinavia and negative SLP anomalies over central and western Europe, (middle panel) lower temperatures in northern Europe, (bottom panel) increased precipitation over part of the Mediterranean and decreased precipitation over Iceland and Scandinavia. The canonical ENSO signal is not unanimously identified and accepted by all authors. The first reason for this disagreement is the use of different statistical technique, ENSO indices and datasets. In addition, nonlinearity plays an important role, since La Niña effects can be non-symmetric with respect to El Niño effects, which furthermore can lead to important differences between one and another event.

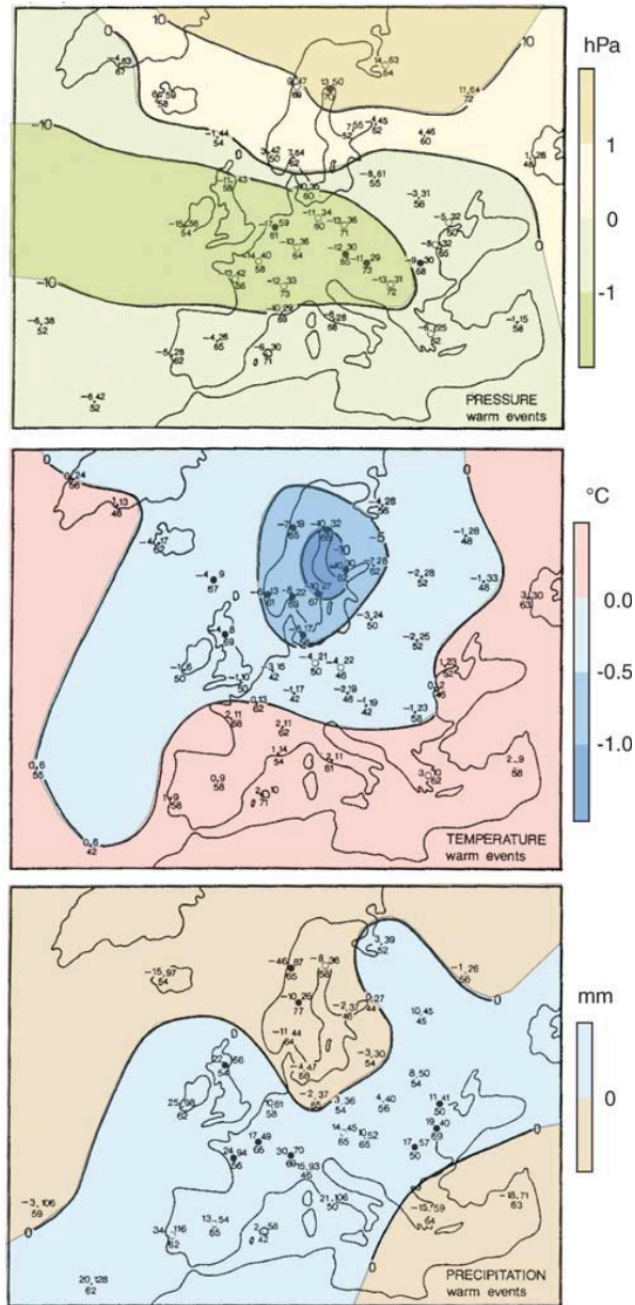


Figure 7.6: Composite anomaly maps of (top) surface pressure, (middle) temperature, and (bottom) rainfall based on station data for twenty-six ENSO warm events from 1880 to 1988 (Brönnimann, 2007).

7.4 Late-winter North Atlantic response to ENSO in PlaSim

The aim of this section is to investigate the extra-tropical response, with a focus on the NA sector, to El Niño and La Niña in an intermediate complexity model such as PlaSim, to make a comparison with observations and the response simulated by more complex, state-of-the-art models. The main advantage of using a climate model of intermediate complexity is the possibility to perform unprecedentedly long simulations with very short computational time, in order to reduce the noise associated with internal atmospheric variability and highlight the extra-tropical response to ENSO (Deser et al., 2017). Therefore, the experimental set-up presented in this section has been first tested by performing “short” 55 year long simulations (50 years after removing the spin-up), which have been subsequently integrated up to 505 years (500 after removing the spin-up) only for the most interesting experiments (“long” simulations).

Before exploring the ability of the model to simulate the ENSO teleconnection, it is useful to analyse the model climatology under normal conditions (see middle panel of 7.5) starting from two control simulations (mentioned in Section 7.1). In the control simulations (CTL) the atmospheric CO₂ level has been kept fixed to the 1990 value and the climatology of SSTs and sea ice cover of the period 1981-2010 has been used as boundary conditions for the atmospheric module of PlaSim. Figure 7.7 presents the ensemble mean of the 500 late winter (JFM) from the two “long” CTL simulations, which differ only in resolution (T21 and T42), and their difference.

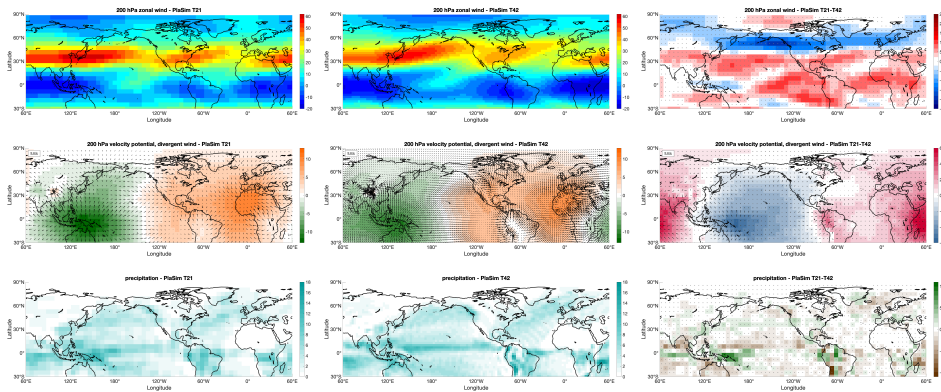


Figure 7.7: Results of CTL simulations with PlaSim. Maps of zonal wind (in ms^{-1}) at 200 hPa in JFM using T21 and T42 resolutions and the difference between them (top panels). Velocity potential (in $10^6 \text{ m}^2 \text{ s}^{-1}$) and divergent wind (in ms^{-1}) at 200 hPa (middle panels). Precipitation (in mm day^{-1} ; bottom panels). Stippling indicate statistically significant areas at 95% confidence level.

All the analyses presented in this section have been carried out on the late-winter season (JFM), which is the most appropriate for studying the extra-tropical response to ENSO, as suggested by Brönnimann (2007). The diagnostics shown in Fig. 7.7 have been chosen to represent the key variables illustrating the development of ENSO teleconnection (see Section 7.3): precipitation (bottom panels) as a proxy for deep convection, velocity potential and wind divergent at 200 hPa (middle panels), showing the divergence and convergence in the upper troposphere, and zonal wind at 200 hPa (top panels), determining the pathway followed by Rossby waves.

The two model resolutions show clear differences in all variables. The maximum of precipitation (and, therefore, of deep convection) in the equatorial Pacific is located east of Indonesia in T21, similarly to what observational datasets show, while in T42 it is shifted north of the equator and has a larger longitudinal extension. The Walker cell, delimited in the upper troposphere (200 hPa) by the zone of maximum divergence (minimum velocity potential) in the west and maximum convergence (maximum velocity potential) in the east, is located further west in T42 compared to T21, as can be seen by noting the position of the grid points with zero velocity potential. Finally, also the mean flow has important differences between the two resolutions especially at mid-latitudes: the jet stream, a westerly flow that forms at the boundary between the low-pressure system at high latitudes and the high-pressure system at subtropical latitudes, is more tilted northward, and therefore more realistic, in the simulation with T42 resolution. These important differences in climatology, which depend on resolution, can be attributed to several factors, including a more realistic representation of the orography using T42. In addition, the model code includes some differences depending on the resolution, as a result from the atmospheric tuning of PlaSim. For example, a tuning parameter for evaporation of precipitation employs two different values using T21 or T42. Since the aim of this chapter is to study the response to ENSO I have not explored further the differences between the two resolutions in CTL and their origin. However, it is important to keep them in mind for later considerations.

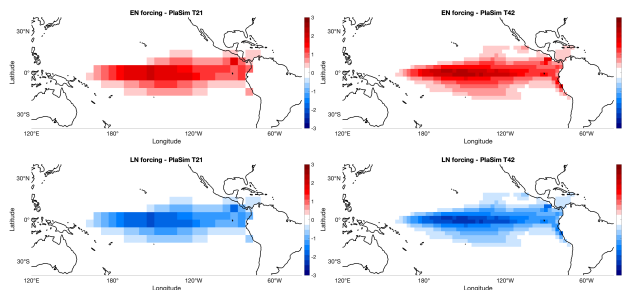


Figure 7.8: SST anomalies in JFM prescribed in EN and LN simulations with PlaSim.

El Niño and La Niña simulations have been performed following the experimental set-up described in Mezzina et al. (2021) using both PlaSim resolutions, T21 and T42. The El Niño simulations (EN) have been performed by superimposing a positive anomaly of SSTs, which reproduces a strong El Niño event in the tropical Pacific, to the climatology used for CTL (top panels of Fig. 7.8). These monthly SST anomalies have been obtained from a linear regression of detrended monthly SST anomalies onto the DJF Niño-3.4 index (area-averaged SST anomalies over 5°S - 5°N / 170° - 120°W) in late winter (JFM) with the same climatological period (1981-2010). Then SST anomalies have been restricted to the region between 20°S and 20°N and increased to reach a maximum of 2.4°C in JFM to realistically reproduce strong El Niño events. For La Niña simulations (LN) the same method has been applied, changing the sign of the SST anomalies with respect to those used for EN (bottom panels of Fig. 7.8). Also in this case the level of atmospheric CO_2 has been kept fixed to the 1990 value and the simulations have been initially integrated for 50 years after the first 5 years of spin-up.

As described in Section 7.3, the first direct consequence of the SST anomalies, which characterize El Niño and La Niña events in the tropical Pacific, is an anomalous diabatic heating associated with deep convection in this region. What determines the development of tropical convection (i.e. precipitation in Fig. 7.9 as a proxy) is the amount of heat supplied to the system: a temperature of at least 27°C (indicated by the yellow line in Fig. 7.9) is representative to have deep convection (Mezzina et al., 2021).

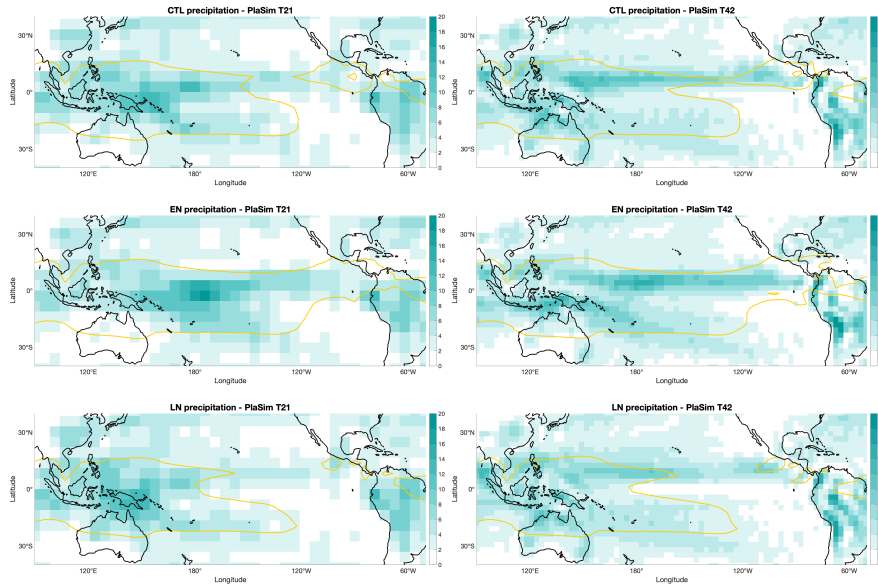


Figure 7.9: Ensemble-mean precipitation (shading) and SST at 27°C (yellow line) for CTL (top), EN (middle) and LN (bottom) experiments using T21 and T42 resolutions.

This condition occurs in CTL mainly in the western part of the ocean basin for both resolutions, albeit with some differences already highlighted in Fig. 7.7. The effect of ENSO in PlaSim is as described in Section 7.2: in EN, the threshold of 27°C is reached all over the tropical Pacific and the maximum of precipitation is shifted eastward, while in LN the convection zone and the maximum of precipitation are located westward with respect to normal conditions. This figure thus shows a first model response to the typical El Niño and La Niña forcing: although the SST anomalies are symmetric, the convection is weaker in LN than in EN.

The extra-tropical propagation of the Rossby wave train forced by El Niño and La Niña is conventionally represented with the geopotential height at 200 hPa (Z200). The upper panels of Fig. 7.10 and 7.11 show the Z200 response to EN and LN with respect to CTL (“short” simulations) for T21 and T42 resolutions, respectively. In the tropical Pacific, the model realistically simulates the Gill-type response, the classical response of the tropical atmosphere to diabatic heating (Gill, 1980). It is more intense in EN than in LN, in agreement with the amplitude of convection explored above, and shows a westward shift in T42 compared to T21, reflecting the differences in the position of the Walker cell between the two resolutions. In EN, the sequence of Z200 minima and maxima that constitute the wave train clearly emerges: the first centre of action in the North Pacific, which corresponds to the (reinforced) Aleutian Low at the surface, the second centre of action located over Canada and the third over the eastern coast of North America.

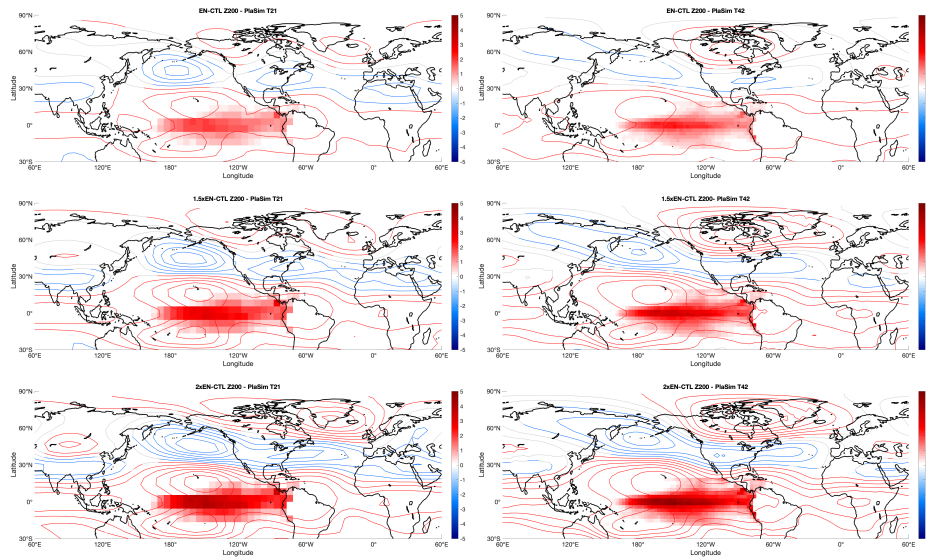


Figure 7.10: Z200 anomalies (in m, contour lines) in EN simulations with respect to CTL simulations for different values of SST anomalies (in K, shading). The interval of contours is 20 m and non-significant values are plotted with grey contours.

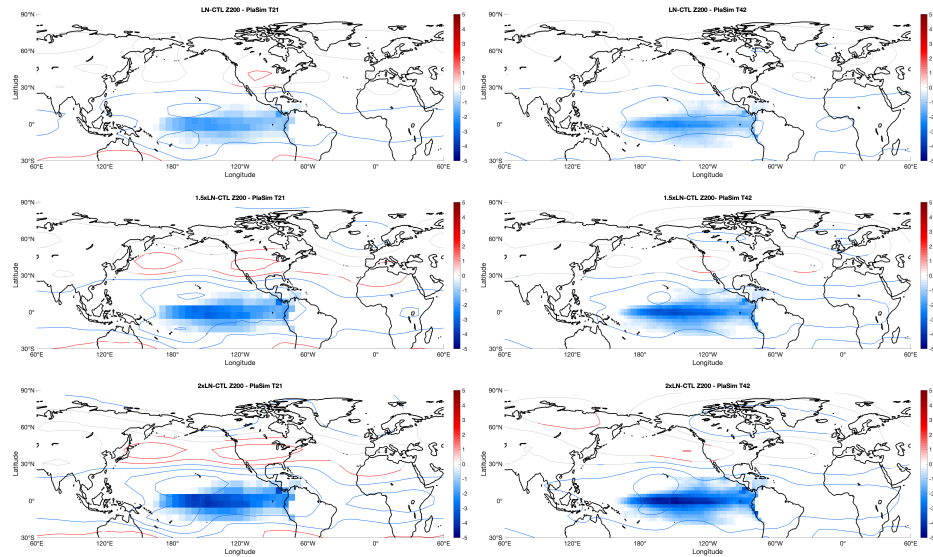


Figure 7.11: Z200 anomalies (in m, contour lines) in LN simulations with respect to CTL simulations for different values of SST anomalies (in K, shading). The interval of contours is 20 m and non-significant values are plotted with grey contours.

Also in terms of the extra-tropical response to El Niño the model presents important differences between the two resolutions: the signal is more intense and statistically significant around the Aleutian Low using T21, while anti-cyclonic circulation at high latitudes is stronger in T42. Other remarkable differences are the shape of the centres of action, which are more elongated in T42, and the presence of a maximum and a minimum respectively over Iceland and the Mediterranean Sea only in T21. In LN, the extra-tropical response is very weak and not statistically significant, so it shows a large asymmetry compared to EN.

Top panels of Fig. 7.10 and 7.11 can be compared with Fig. 7.12 from Mezzina et al. (2021). The authors have performed idealized experiments similar to those described above using three state-of-the-art models. In Fig. 7.12 the contours show the Z200 response to EN and LN with respect to CTL (all their simulations have 50 ensemble members) in the EC-Earth3.2 model, with horizontal resolution T255 (about 80 km) and 91 vertical levels (Davini et al., 2017; Haarsma et al., 2020). The comparison between PlaSim and EC-Earth shows that the former, being an intermediate complexity model, is able to reproduce in a realistic way the tropical and extra-tropical pattern associated with El Niño, albeit with weaker amplitude. Unlike EC-Earth, however, the model is unable to reproduce the extra-tropical response to La Niña. This can be attributed to a weaker tropical response of the model and consequently to a lower amount of energy propagating from the tropics to

the extra-tropics. This model issue emerges especially in LN, which is itself associated with a weaker response, as it is observed also in Fig. 7.12.

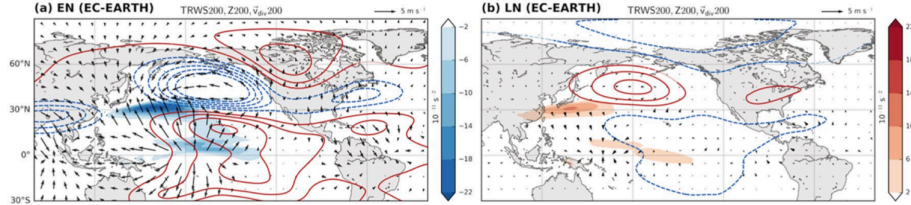


Figure 7.12: Ensemble-mean 200-hPa Tropical Rossby Wave Source (shading), divergent wind (arrows) and Z200 (contours; interval = 30 m) anomalies for EN and LN in JFM in the EC-Earth climate model (Mezzina et al., 2021).

In order to verify that the dynamics involved in the ENSO teleconnection in PlaSim is realistic and the differences with respect to observations and more complex climate models are due to differences in sensitivity, I have analysed the response associated with an arbitrary and absolutely unrealistic increase in the forcing. For each resolution, I have performed four new “short” simulations (two EN, shown in Fig. 7.10, and two LN, in Fig. 7.11) in which the SST anomalies were multiplied by 1.5 and 2, before superimposing them to the climatology. Z200 anomalies indicate that PlaSim responds to increased surface energy in the tropics with a larger amplitude in the upper troposphere, including the extra-tropics, again with a strong asymmetry between EN and LN. In addition, the model with T42 resolution has a very weak and not statistically significant extra-tropical response even in simulations with increased forcing, while using T21 a higher sensitivity emerges. To obtain a signal in the North Pacific as strong as that of EC-Earth in EN simulations, it is necessary to at least double the forcing and thus to impose temperature anomalies in the equatorial Pacific with a maximum of almost 5°C, which are unrealistic.

Following these considerations, I have decided to focus on the response in the NA sector only to El Niño events. I have performed two EN “long” simulations, one for each resolution, integrated for 500 years after the spin-up. Figure 7.13 shows EN anomalies with respect to CTL in JFM in terms of SST (the forcing imposed as boundary condition), SLP, precipitation and Z200. The larger number of ensemble members allows to minimize the internal atmospheric variability and increase the statistical significance of the El Niño response, as suggested by Deser et al. (2017). The centres of action in the upper troposphere, already identified in Fig. 7.10 and previously described, are associated with SLP anomalies located further east. This westward tilt with height is an intrinsic feature of the Rossby waves and constitutes a fundamental difference from the signal related to the NAO, in which the anomalies are essentially barotropic (Mezzina et al., 2021). The NA sector is

affected at the surface, showing two centres of action: a positive SLP anomaly centered over Iceland, more intense at T42, and a negative SLP anomaly centered over the ocean at mid-latitudes, further west at T21. Note that this is the canonical late-winter signature of ENSO. In the upper troposphere, the anticyclonic circulation at high latitudes has two well-separated centres of action with T21, one located between Iceland and Greenland, while with T42 there is mainly one centered over Canada. Also the cyclonic circulation over the Atlantic Ocean is located further west in T21 than in T42, in agreement with the surface signal.

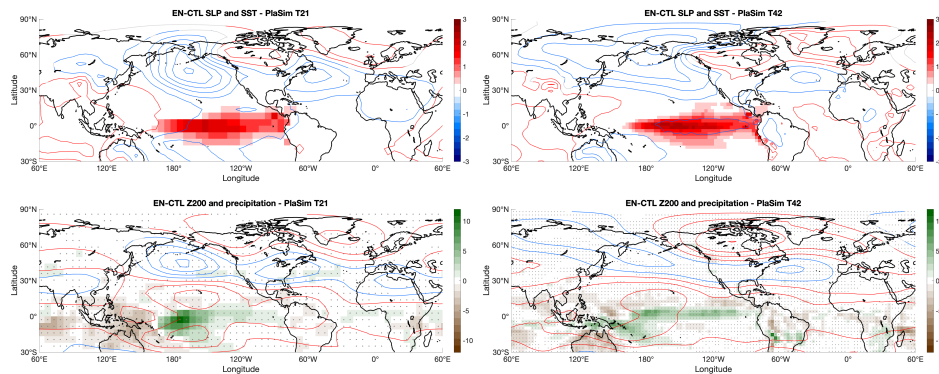


Figure 7.13: Anomalies for EN simulations with respect to CTL simulations. (Top panels) SST (in K, shading) and SLP (in hPa, contours with interval of 0.5 hPa) anomalies in JFM for T21 (left) and T42 (right) resolution. (Bottom panels) precipitation (in mm day⁻¹, shading) and geopotential height at 200 hPa (in m, contours with interval of 20 m). Stippling indicate statistically significant areas at 95% confidence level for shading, non-significant values for contours are plotted in grey.

Another fundamental factor that determines the ability of a model to reproduce the atmospheric circulation associated with ENSO is its interannual variability, i.e. how much the system oscillates around its mean value. The model range of variability constitutes a limit to the amplitude of the characteristic ENSO signature in the extra-tropics. Figure 7.14 compares the standard deviation of SLP computed in PlaSim T21 and T42 with values obtained from four reanalysis datasets, NOAA-20CR (1900-2010; Compo et al. (2006)), ERA-20CR (1900-2010; Poli et al. (2016)), ERA-Interim (1979-2019; Dee et al. (2011)), NCEP/NCAR (1948-2019; Kalnay et al. (1996)). The variability has been studied at the main semi-permanent pressure systems, the Aleutian Low in the Pacific Ocean, the Azores High and the Icelandic Low in the Atlantic Ocean. This analysis shows that the model variability at both resolutions is lower than observed. Therefore, the amplitude of the extra-tropical response to ENSO in PlaSim is expected to be weaker than observed or simulated by state-of-the-art models (see Fig 7.12) because of

the smaller variability of the model.

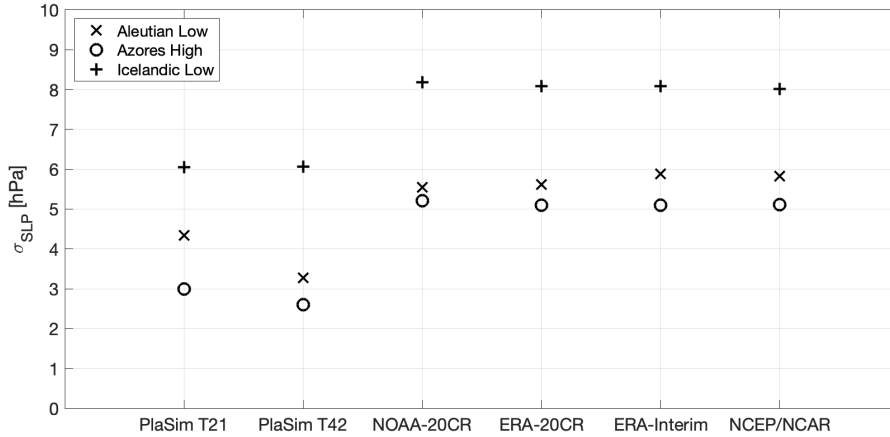


Figure 7.14: Standard deviation of SLP in JFM computed over three different regions corresponding to Aleutian Low, Azores High and Icelandic Low. PlaSim CTL simulations (T21 and T42 resolution) are compared with reanalysis datasets: NOAA-20CR, ERA-20CR, ERA-Interim, NCEP/NCAR.

7.5 Concluding remarks

El Niño-Southern Oscillation affects global climate and the occurrence of climate extremes via atmospheric or oceanic teleconnections. Due to the impact of the ENSO teleconnection on ecosystems and human societies, the comprehension of involved processes and effects is an important challenge in climate research. A hierarchy of climate models, spanning from conceptual to high-resolution Earth-system models, has enhanced the understanding of the main mechanisms generating ENSO. In this chapter, the representation of the ENSO teleconnection in the NA sector has been assessed for the first time from the perspective of an EMIC. The tropical and extra-tropical response associated with ENSO in PlaSim is similar in terms of pattern to that simulated by other more complex models: PlaSim realistically reproduces both the Gill-type response in the tropical region and the sequence of Z200 maxima and minima that constitute the Rossby wave train in the extra-tropical region up to the NA sector, although with some differences depending on the model resolution. However, the signal associated with ENSO in PlaSim is weak, and to obtain an amplitude comparable to that simulated in other models it is necessary to have an unrealistic forcing in the tropical Pacific. This problem can be attributed both to a weak tropical response and to a small range of extra-tropical variability in the model. The main

advantage of using an EMIC such as PlaSim to study the ENSO response is the possibility to perform unprecedentedly long simulations due to the reduced computational time with respect to more complex climate models. In this way, the unpredictable internal atmospheric variability is minimized and the signal associated with ENSO emerges, as shown by the comparison between significant values for Z200 in Fig. 7.10 (top panels) and Fig. 7.13 (bottom panels).

Conclusions

Earth-system Models of Intermediate Complexity (EMICs), which are presented in Chapter 1 of this PhD thesis, are in the middle of the spectrum of numerical models for climate simulation, between conceptual models, which contain a simple approximation of the Earth system, and comprehensive models, which include all components and processes and provide a detailed representation of them. EMICs also contain a rather complete description of the climate system but with simpler parameterizations compared to more complex models. The low resolution and the high number of parameterized processes included in EMICs makes them ideal for performing very long simulations and large ensembles, since the computational times are short and the required resources are limited. Therefore these models are often used as a laboratory to separately explore processes and feedbacks, to perform sensitivity experiments and to understand in which direction to address similar studies in more complex models, which require considerably greater resources. In this thesis, different configurations of the Planet Simulator (PlaSim) EMIC have been initially explored to evaluate its ability to simulate past, present and future climate. The model has been then used to investigate climate variability on different timescales. The main features of PlaSim are presented in Chapter 2. PlaSim consists of the Portable University Model of Atmosphere (PUMA) atmospheric module, which can be forced with a climatology of sea surface temperatures (SSTs) or coupled to an ocean module. This thesis, configurations of PlaSim coupled with a simple mixed-layer (ML) ocean or with a global model of ocean circulation, the Large Scale Geostrophic (LSG) ocean have been explored. Sea ice can be prescribed by a climatology or simulated by a thermodynamic sea ice model. There are also other components that can be implemented, such as the SimBA vegetation module, but they have not been used in this thesis. The use of this model has required an initial tuning of some oceanic parameters presented in Chapter 3, since the chosen configurations of PlaSim have been poorly explored and documented in the literature and the currently available version of the model presents several problems related to the values of these parameters. The chosen configurations are PlaSim-ML T21, with mixed-layer ocean and coarse resolution (about 600 km), PlaSim-ML T42, equal to the first configuration but with finer resolution (about 300 km), and PlaSim-LSG T21, in which

the atmospheric model is coupled to the more complex ocean model and the resolution is the coarser one. All configurations use dynamic sea ice. In order to parameterize the ocean transport in the ML ocean, horizontal diffusion has been activated, which controlled by the horizontal diffusion coefficient K_h . This choice is due to the fact that the alternative to horizontal diffusion, i.e. the flux correction that is the most used parameterization when coupling the model with the ML ocean, is specific for present climate and may not be suitable for climate studies under conditions very far from the present one. Therefore it may be useful to explore an alternative parameterization of ocean transport to flux correction. A preliminary analysis with the aim of obtaining a realistic zonally-averaged near-surface air temperatures profiles has suggested the use of two different values for K_h , one in the NH and another in the SH. In particular, in the PlaSim-ML T21 configuration the optimal coefficients are $K_h = 10^5 \text{ m}^2\text{s}^{-1}$ in the NH and $K_h = 10^4 \text{ m}^2\text{s}^{-1}$ in the SH. In the PlaSim-ML T42 configuration the optimal coefficients are $K_h = 10^5 \text{ m}^2\text{s}^{-1}$ in the NH and $K_h = 3 \cdot 10^4 \text{ m}^2\text{s}^{-1}$ in the SH. The use of these values represents a significant improvement with respect to the default value for both terrestrial hemispheres, $K_h = 10^3 \text{ m}^2\text{s}^{-1}$, which is not appropriate to give a realistic representation of the temperature distribution. In the PlaSim-LSG T21 configuration, several sets of parameters constituting the the vertical oceanic diffusion profile A_v , which is a parameterization of turbulent motions, have been explored. In fact, both the default set of parameters in the model and those suggested in the literature (Bryan and Lewis, 1979) cause a collapse of the Atlantic Meridional Overturning Circulation (AMOC) and consequently the NH is too cold. A compromise between a robust AMOC and the presence of sea ice in the SH has led to an optimal profile of A_v ranging from $0.45 \cdot 10^{-4} \text{ m}^2\text{s}^{-1}$ at the top to $0.8 \cdot 10^{-4} \text{ m}^2\text{s}^{-1}$ at the bottom of the ocean. Since the model in this configuration has a warm bias in the Southern Ocean, some model parameters have been explored in an attempt to reduce it. Although these analyses have not allowed to identify a method to reduce the warm bias, they have made it possible to exclude some hypotheses and explore some aspects of the model. The latest evidence reveals that in more complex models the warm bias in the Southern Ocean can be reduced by including the cloud micro-physics or by the vertical mixing of ocean temperatures in that region. These possibilities could also be explored in PlaSim in the future. The choice of these oceanic parameters has been further investigated in Chapter 4, which presents a comparison between some surface variables simulated in the model and several observational and reanalysis datasets. The values obtained from the model tuning can also be justified by the fact that for all configurations the simulated ocean transport is in better agreement with the reanalysis than the transport obtained with the default values of the model. Most of the climate variables are well simulated but the model does not provide a perfect energy balance in any of the explored configurations.

Some problems can be attributed to the coarse resolution of the model, in fact using the finer T42 resolution some anomalies computed with respect to observations are reduced and a smaller imbalance is obtained. These imbalances are small compared to those reported in the literature for other climate models. However, as demonstrated in the following analysis on the interannual variability, the finer resolution does not always correspond to climatic variables more similar to those observed. The model evaluation has been finally extended to the representation of past and future climate in the model by performing transient simulations from 1850 to 2100. The CO₂ concentration has been varied in the model according to the historical evolution from the pre-industrial to the present condition and then according to two different scenarios, one of emission stabilization and another one of high emissions, for the future. The simulated time series of temperature has been compared with the observed values for the past years and with the results of models belonging to CMIP5 for future projection. It emerges that the PlaSim-LSG T21 configuration is the one that best reproduces both the historical series and the future evolution of climate. Another possibility to explore the ability of a model in simulating climate change in the future is the estimation of its Equilibrium Climate Sensitivity (ECS), defined as the equilibrium change in global mean surface air temperature after an instantaneous doubling of atmospheric CO₂ relative to pre-industrial levels. The ECS of the three configurations of PlaSim has been computed by applying the Gregory method (Gregory et al., 2004) and is presented in Chapter 5. The ECS of the model is particularly high in configurations with ML ocean, with 6.23 K using PlaSim-ML T21 and 5.45 K using PlaSim-LSG T42, when compared to 4.26 K using PlaSim-LSG. These values have been then compared with the values obtained for other state-of-the-art EMICs, CMIP5 and CMIP6 models. Only the ECS of PlaSim-LSG is within the CMIP5 range, although close to the upper limit. The EMICs and CMIP6 models have a wider range of ECS and therefore also the PlaSim-ML T42 configuration is within these values, even if close to the upper limit also in this case. An important factor contributing to the higher ECS in PlaSim-ML compared to PlaSim-LSG is the lack of AMOC in the simple mixed-layer ocean, which therefore cannot weaken or collapse with a cooling effect on global mean temperatures. The high ECS in PlaSim-ML is also related to elevated values in magnitude of the sea ice feedback parameter, which has been obtained by comparing simulations with prescribed sea ice and dynamic sea ice. The ECS experiments have revealed that the details of oceanic heat transport play an important role in determining the sea ice feedback parameter and consequently the ECS model. When using the horizontal diffusion in the ML ocean with K_h values that provide a realistic distribution of present-day temperatures, changes in sea ice area have a much stronger radiative impact than using low K_h values or a flux-correction approach. Another relevant factor in determining the model ECS is the sea ice extent in pre-industrial

and future conditions: since the sea ice feedback has a significant impact, the almost total absence of sea ice in the SH in PlaSim-LSG contributes to the low ECS of this configuration compared to PlaSim-ML configurations. These results are presented in the paper Angeloni et al. (2020), currently available on GMDD. During the study of the vertical oceanic diffusion coefficient in PlaSim-LSG, it was found that the model shows different AMOC regimes, including one characterized by regular multicentennial oscillations with an amplitude of several Sverdrups. Currently there is a lot of interest in the use of PlaSim for paleoclimatic studies because it allows to simulate tens of thousands of years in a short time thanks to the reduced computational times. For this reason, a study that clarifies the stability conditions of the model and explores the oscillation mechanisms of AMOC may be of interest to understand possible future uses of the model in this setting. Further, there is significant interest for the study of tipping points in the climate system and for the stability of AMOC. Chapter 6 therefore explores the dependence of AMOC regimes on two model parameters, the vertical diffusion coefficient A_v , and the atmospheric CO_2 concentration, and then investigates the mechanism generating the oscillations. The analyses have revealed that a fundamental role is played by the formation and melting of Arctic sea ice and by the accumulation of surface salinity anomalies at high latitudes, which takes several decades to reach the North Atlantic Deep Water (NADW) formation region and to strengthen the AMOC trend. In fact, when AMOC is in a phase of increase due to the high pole-equator temperature gradient, sea ice begins to melt due to rising temperatures at high latitudes. This melting leaves a larger part of the ocean uncovered so evaporation is enabled, resulting in increased salinity in the Arctic basin. This salinity anomaly reaches the sinking zone with a certain delay, with the effect of further intensifying the AMOC, which therefore never reaches the equilibrium state. When the AMOC is maximum and the pole-equator gradient very low, the self-regulating mechanism is triggered so that the AMOC begins to weaken, the sea ice cover increases and the process repeats with opposite signs, until the minimum of oscillation is reached. The mechanism associated to AMOC oscillations, although with global impacts, therefore originates from salinity or freshwater exchanges between the Arctic basin and the North Atlantic. This work is converging in a paper in preparation, Angeloni et al. (2022). The impacts of AMOC decline in CMIP5 and CMIP6 4x CO_2 experiments has been explored in the paper Bellomo et al. (2021), to which I have participated. Finally, Chapter 7 presents a study of the variability of the model on shorter, interannual timescales, also in this case with a focus on the North Atlantic sector. After presenting the signal associated with the North Atlantic Oscillation (NAO) in the model, sensitivity experiments performed with PlaSim with a prescribed SST forcing mimicking El Niño (EN) or La Niña (LN) events have been analysed, with the aim of studying the extra-tropical atmospheric response and comparing it with the results

of the global state-of-the-art model EC-Earth. The advantage of using an EMIC such as PlaSim in a study of this type is the possibility to simulate a large ensemble of typical El Niño-Southern Oscillation (ENSO) events, which allows to reduce the atmospheric variability not associated with the ENSO response and to bring out the signal of interest. Although the forcing is symmetric for EN and LN experiments, the model shows a strong asymmetry in the extra-tropical atmospheric response. The variability pattern associated with EN is realistically reproduced in PlaSim, albeit with lower intensity than EC-Earth. On the contrary, the extra-tropical response associated with LN is very weak and not statistically significant. Some analyses with and increased forcing have shown that, in order to obtain an extra-tropical signal comparable in terms of intensity with that simulated in EC-Earth, it is necessary to increase the SST anomalies to values that have never been observed in the real world for EN and LN events. These results show that the dynamics involved in the ENSO teleconnection is correctly described in PlaSim, but the atmospheric response is weak and therefore there is not enough energy transfer from the tropics to the extra-tropics. Moreover, the variability of PlaSim is small compared to the variability computed from some reanalysis datasets, thus representing a limit for the amplitude of the ENSO signature in the extra-tropics. In addition, a strong dependence on the resolution of model has been shown, which can be traced to differences at several levels (characteristics and position of deep convection, divergence in upper troposphere and mean flow) that are also found in control runs where there is no signal associated with ENSO.

The studies presented in this thesis fill some gaps in the available literature on the PlaSim EMIC. In fact, so far no work has been documented that explores in detail the configuration of PlaSim coupled with a mixed-layer ocean with horizontal diffusion and the configuration of PlaSim coupled to the LSG ocean. This thesis provides reference values for some oceanic parameters that are not properly calibrated in the default version and that can be used as a starting point for future studies with this model. In addition to the presentation of average climatology, the response of PlaSim has been also shown in terms of ECS, in terms of variability at a centennial timescale, which gives rise to AMOC oscillations, or at interannual timescale, such as that characterizing the extra-tropical response to ENSO. This study demonstrates that despite its simplicity and limitations, a model such as PlaSim does not contain a trivial dynamic and is flexible enough to answer interesting scientific questions. Therefore, it can be used as a complementary tool to simpler and more complex models, to maximize the possibilities that the broad spectrum of climate models can provide.

Bibliography

- Adler RF, Huffman GJ, Chang A, Ferraro R, Xie PP, Janowiak J, Rudolf B, Schneider U, Curtis S, Bolvin D, Gruber A, Susskind J, Arkin P, Nelkin E (2003) The Version-2 Global Precipitation Climatology Project (GPCP) Monthly Precipitation Analysis (1979–Present). *J Hydrometeor* 4(6):1147–1167, DOI [https://doi.org/10.1175/1525-7541\(2003\)004<1147:TVGPCP>2.0.CO;2](https://doi.org/10.1175/1525-7541(2003)004<1147:TVGPCP>2.0.CO;2)
- Andres HJ, Tarasov L (2019) Towards understanding potential atmospheric contributions to abrupt climate changes: characterizing changes to the North Atlantic eddy-driven jet over the last deglaciation. *Clim Past* 15(4):1621–1646, DOI <https://doi.org/10.5194/cp-15-1621-2019>
- Andrews T, Gregory JM, Webb MJ, Taylor KE (2012) Forcing, feedbacks and climate sensitivity in CMIP5 coupled atmosphere-ocean climate models. *Geophys Res Lett* 39(9), DOI <https://doi.org/10.1029/2012GL051607>
- Angeloni M (2018) Tuning di un modello climatico a complessità intermedia per riprodurre una risposta realistica alla forzante climatica antropogenica, Dissertation, University of Turin
- Angeloni M, Palazzi E, von Hardenberg J (2020) Climate sensitivity of the PlaSim Earth-system model coupled with ocean model components of different complexity. *Geosci Model Dev Discuss* [preprint] DOI <https://doi.org/10.5194/gmd-2020-245>
- Angeloni M, Bellomo K, Pasquero C, von Hardenberg J (2022) Salinity-driven centennial oscillations of amoc in an earth-system model of intermediate complexity (in preparation)
- Arakawa A, Lamb VR (1977) Computational Design of the Basic Dynamical Processes of the UCLA General Circulation Model. In: Chang J (ed) *Methods in Computational Physics: Advances in Research and Applications, General Circulation Models of the Atmosphere*, vol 17, Elsevier, pp 173–265, DOI <https://doi.org/10.1016/B978-0-12-460817-7.50009-4>

- Asselin R (1972) Frequency Filter for Time Integrations. *Mon Weather Rev* 100(6):487–490, DOI [https://doi.org/10.1175/1520-0493\(1972\)100<0487:FFFTI>2.3.CO;2](https://doi.org/10.1175/1520-0493(1972)100<0487:FFFTI>2.3.CO;2)
- Bellomo K, Angeloni M, Corti S, von Hardenberg J (2021) Future climate change shaped by inter-model differences in Atlantic meridional overturning circulation response. *Nat Commun* 12(1):3659, DOI <https://doi.org/10.1038/s41467-021-24015-w>
- Birchfield GE, Broecker WS (1990) A salt oscillator in the glacial Atlantic? 2. A “scale analysis” model. *Paleoceanography* 5(6):835–843, DOI <https://doi.org/10.1029/PA005i006p00835>
- Boucher O, Servonnat J, Albright AL, Aumont O, Balkanski Y, Bastrikov V, Bekki S, Bonnet R, Bony S, Bopp L, Braconnot P, Brockmann P, Cadule P, Caubel A, Cheruy F, Codron F, Cozic A, Cugnet D, D’Andrea F, Davini P, Lavergne Cd, Denvil S, Deshayes J, Devilliers M, Ducharne A, Dufresne JL, Dupont E, Éthé C, Fairhead L, Falletti L, Flavoni S, Foujols MA, Gardoll S, Gastineau G, Ghattas J, Grandpeix JY, Guenet B, Guez L E, Guilyardi E, Guimberteau M, Hauglustaine D, Hourdin F, Idelkadi A, Joussaume S, Kageyama M, Khodri M, Krinner G, Lebas N, Levavasseur G, Lévy C, Li L, Lott F, Lurton T, Luyssaert S, Madec G, Madeleine JB, Maignan F, Marchand M, Marti O, Mellul L, Meurdesoif Y, Mignot J, Musat I, Ottlé C, Peylin P, Planton Y, Polcher J, Rio C, Rochetin N, Rousset C, Sepulchre P, Sima A, Swingedouw D, Thiéblemont R, Traore AK, Vancoppenolle M, Vial J, Vialard J, Viovy N, Vuichard N (2020) Presentation and Evaluation of the IPSL-CM6A-LR Climate Model. *J Adv Model Earth Syst* 12(7), DOI <https://doi.org/10.1029/2019MS002010>
- Broecker WS, Bond G, Klas M, Bonani G, Wolfli W (1990) A salt oscillator in the glacial Atlantic? 1. The concept. *Paleoceanography* 5(4):469–477, DOI <https://doi.org/10.1029/PA005i004p00469>
- Bryan K, Lewis LJ (1979) A water mass model of the World Ocean. *J Geophys Res* 84(C5):2503–2517, DOI <https://doi.org/10.1029/JC084iC05p02503>
- Brönnimann S (2007) Impact of El Niño-Southern Oscillation on European climate. *Rev Geophys* 45, DOI <https://doi.org/10.1029/2006RG000199>
- Caldeira K, Cvijanovic I (2014) Estimating the Contribution of Sea Ice Response to Climate Sensitivity in a Climate Model. *J Clim* 27(22):8597–8607, DOI <https://doi.org/10.1175/JCLI-D-14-00042.1>
- Claussen M, Ganopolski A, Schellnhuber HJ, Cramer W, IGBP Secretariat S (2000) Earth-system models of intermediate complexity. towards a definition of the Earth system and Earth system models. *Global Change Newsletter* (41):4–6

- Claussen M, Mysak L, Weaver A, Crucifix M, Fichet T, Loutre MF, Weber S, Alcamo J, Alexeev V, Berger A, Calov R, Ganopolski A, Goosse H, Lohmann G, Lunkeit F, Mokhov I, Petoukhov V, Stone P, Wang Z (2002) Earth system models of intermediate complexity: Closing the gap in the spectrum of climate system models. *Clim Dyn* 18:579–586, DOI <https://doi.org/10.1007/s00382-001-0200-1>
- Compo GP, Whitaker JS, Sardeshmukh PD (2006) Feasibility of a 100-Year Reanalysis Using Only Surface Pressure Data. *Bull Amer Meteor* 87(2):175–190, DOI <https://doi.org/10.1175/BAMS-87-2-175>
- Dahms E, Borth H, Lunkeit F, Fraedrich K (2011) ITCZ Splitting and the Influence of Large-Scale Eddy Fields on the Tropical Mean State. *J Meteorol Soc Jpn* 89(5):399–411, DOI <https://doi.org/10.2151/jmsj.2011-501>
- Dahms E, Lunkeit F, Fraedrich K (2012) Low-frequency climate variability of an aquaplanet. *Theor Appl Climatol* 121:7932, DOI <https://doi.org/10.1007/s00704-014-1226-8>
- Danabasoglu G, Gent PR (2009) Equilibrium climate sensitivity: Is it accurate to use a slab ocean model? *J Clim* 22(9):2494 – 2499, DOI <https://doi.org/10.1175/2008JCLI2596.1>
- Dansgaard W, Johnsen SJ, Clausen HB, Dahl-Jensen D, Gundestrup NS, Hammer CU, Hvidberg CS, Steffensen JP, Sveinbjörnsdóttir AE, Jouzel J, Bond G (1993) Evidence for general instability of past climate from a 250-kyr ice-core record. *Nature* 364(6434):218–220, DOI <https://doi.org/10.1038/364218a0>
- Davini P, von Hardenberg J, Corti S, Christensen HM, Juricke S, Subramanian A, Watson PAG, Weisheimer A, Palmer TN (2017) Climate SPHINX: evaluating the impact of resolution and stochastic physics parameterisations in the EC-Earth global climate model. *Geosci Model Dev* 10(3):1383–1402, DOI <https://doi.org/10.5194/gmd-10-1383-2017>
- Dee DP, Uppala SM, Simmons AJ, Berrisford P, Poli P, Kobayashi S, Andrae U, Balsameda MA, Balsamo G, Bauer P, Bechtold P, Beljaars ACM, Berg Lvd, Bidlot J, Bormann N, Delsol C, Dragani R, Fuentes M, Geer AJ, Haimberger L, Healy SB, Hersbach H, Hólm EV, Isaksen L, Kállberg P, Köhler M, Matricardi M, McNally AP, Monge-Sanz BM, Morcrette JJ, Park BK, Peubey C, Rosnay Pd, Tavolato C, Thépaut JN, Vitart F (2011) The ERA-Interim reanalysis: configuration and performance of the data assimilation system. *Q J R Meteorol Soc* 137(656):553–597, DOI <https://doi.org/10.1002/qj.828>

- Delworth TL, Zeng F (2012) Multicentennial variability of the Atlantic meridional overturning circulation and its climatic influence in a 4000 year simulation of the GFDL CM2.1 climate model. *Geophys Res Lett* 39(13), DOI <https://doi.org/10.1029/2012GL052107>
- Deser C, Alexander MA, Xie SP, Phillips AS (2010) Sea Surface Temperature Variability: Patterns and Mechanisms. *Annu Rev Mar Sci* 2(1):115–143, DOI <https://doi.org/10.1146/annurev-marine-120408-151453>
- Deser C, Simpson IR, McKinnon KA, Phillips AS (2017) The Northern Hemisphere Extratropical Atmospheric Circulation Response to ENSO: How Well Do We Know It and How Do We Evaluate Models Accordingly? *J Clim* 30(13):5059–5082, DOI <https://doi.org/10.1175/JCLI-D-16-0844.1>
- Drijfhout SS, Maier-Reimer E, Mikolajewicz U (1996) Tracing the conveyor belt in the Hamburg large-scale geostrophic ocean general circulation model. *J Geophys Res* 101(C10):22563–22575, DOI <https://doi.org/10.1029/96JC02162>
- Döscher R, Acosta M, Alessandri A, Anthoni P, Arneth A, Arsouze T, Bergmann T, Bernadello R, Bousetta S, Caron LP, Carver G, Castrillo M, Catalano F, Cvijanovic I, Davini P, Dekker E, Doblas-Reyes FJ, Docquier D, Echevarria P, Fladrich U, Fuentes-Franco R, Gröger M, v Hardenberg J, Hieronymus J, Karami MP, Keskinen JP, Koenigk T, Makkonen R, Massonnet F, Ménégos M, Miller PA, Moreno-Chamarro E, Nieradzik L, van Noije T, Nolan P, O'Donnell D, Ollinaho P, van den Oord G, Ortega P, Prims OT, Ramos A, Reerink T, Rousset C, Ruprich-Robert Y, Le Sager P, Schmith T, Schrödner R, Serva F, Sicardi V, Sloth Madsen M, Smith B, Tian T, Tourigny E, Uotila P, Vancoppenolle M, Wang S, Wårlind D, Willén U, Wyser K, Yang S, Yepes-Arbós X, Zhang Q (2021) The EC-Earth3 Earth System Model for the Climate Model Intercomparison Project 6. *Geosci Model Dev Discuss* [preprint] DOI <https://doi.org/10.5194/gmd-2020-446>
- Eby M, Weaver AJ, Alexander K, Zickfeld K, Abe-Ouchi A, Cimadoribus AA, Cresspin E, Drijfhout SS, Edwards NR, Eliseev AV, Feulner G, Fichefet T, Forest CE, Goosse H, Holden PB, Joos F, Kawamiya M, Kicklighter D, Kienert H, Matsumoto K, Mokhov II, Monier E, Olsen SM, Pedersen JOP, Perrette M, Philippon-Berthier G, Ridgwell A, Schlosser A, Schneider von Deimling T, Shaffer G, Smith RS, Spahni R, Sokolov AP, Steinacher M, Tachiiri K, Tokos K, Yoshimori M, Zeng N, Zhao F (2013) Historical and idealized climate model experiments: an intercomparison of Earth system models of intermediate complexity. *Clim Past* 9(3):1111–1140, DOI <https://doi.org/10.5194/cp-9-1111-2013>
- Eliassen E, Machenhauer B, Rasmussen E (1970) On a numerical method for

- integration of the hydrodynamical equations with a spectral representation of the horizontal fields. DOI <https://doi.org/10.13140/RG.2.2.13894.88645>
- Fraedrich K (2012) A suite of user-friendly global climate models: Hysteresis experiments. *Eur Phys J Plus* 127(5):53, DOI <https://doi.org/10.1140/epjp/i2012-12053-7>
- Fraedrich K, Lunkeit F (2008) Diagnosing the entropy budget of a climate model. *Tellus A* 60:921–931, DOI <https://doi.org/10.1111/j.1600-0870.2008.00338.x>
- Fraedrich K, Jansen H, Kirk E, Luksch U, Lunkeit F (2005) The Planet Simulator: Towards a user friendly model. *Meteorol Z* 14:299–304, DOI <https://doi.org/10.1127/0941-2948/2005/0043>
- Gent PR, Danabasoglu G, Donner LJ, Holland MM, Hunke EC, Jayne SR, Lawrence DM, Neale RB, Rasch PJ, Vertenstein M, Worley PH, Yang ZL, Zhang M (2011) The Community Climate System Model Version 4. *J Clim* 24(19):4973–4991, DOI <https://doi.org/10.1175/2011JCLI4083.1>
- Gill AE (1980) Some simple solutions for heat-induced tropical circulation. *Q J R Meteorol Soc* 106(449):447–462, DOI <https://doi.org/10.1002/qj.49710644905>
- Goosse H, Barriat PY, Lefebvre W, Loutre MF, Zunz V (2010) Introduction to climate dynamics and climate modeling. online textbook available at <http://www.climate.be/textbook>
- Green AES (1964) Attenuation by Ozone and the Earth's Albedo in the Middle Ultraviolet. *Appl Opt* 3(2):203–208, DOI <https://doi.org/10.1364/AO.3.000203>
- Gregory JM, Ingram WJ, Palmer MA, Jones GS, Stott PA, Thorpe RB, Lowe JA, Johns TC, Williams KD (2004) A new method for diagnosing radiative forcing and climate sensitivity. *Geophys Res Lett* 31(3), DOI <https://doi.org/10.1029/2003GL018747>
- Haarsma R, Acosta M, Bakhshi R, Bretonnière PA, Caron LP, Castrillo M, Corti S, Davini P, Exarchou E, Fabiano F, Fladrich U, Fuentes Franco R, García-Serrano J, von Hardenberg J, Koenigk T, Levine X, Meccia VL, van Noije T, van den Oord G, Palmeiro FM, Rodrigo M, Ruprich-Robert Y, Le Sager P, Tourigny E, Wang S, van Weele M, Wyser K (2020) High-ResMIP versions of EC-Earth: EC-Earth3P and EC-Earth3P-HR – description, model computational performance and basic validation. *Geosci Model Dev* 13(8):3507–3527, DOI <https://doi.org/10.5194/gmd-13-3507-2020>

- Hagemann S, Botzet M, Duemenil L, Machenhauer B (1999) Derivation of global GCM boundary conditions from 1 km land use satellite data, MPI Report no. 289. Max Planck Institute for Meteorology, Hamburg URL https://mpimet.mpg.de/fileadmin/publikationen/Reports/max_scirep_289.pdf
- Hartmann DL (2016) Chapter 8 - Natural Intraseasonal and Interannual Variability. In: Hartmann DL (ed) *Global Physical Climatology* (Second Edition), Elsevier, Boston, pp 233–259, DOI <https://doi.org/10.1016/B978-0-12-328531-7.00008-6>
- Hasselmann K (1982) An ocean model for climate variability studies. *Prog Oceanogr* 11(2):69–92, DOI [https://doi.org/10.1016/0079-6611\(82\)90004-0](https://doi.org/10.1016/0079-6611(82)90004-0)
- Hazeleger W, Wang X, Severijns C, Ștefănescu S, Bintanja R, Sterl A, Wyser K, Semmler T, Yang S, van den Hurk B, van Noije T, van der Linden E, van der Wiel K (2012) EC-Earth V2.2: description and validation of a new seamless earth system prediction model. *Clim Dyn* 39(11):2611–2629, DOI <https://doi.org/10.1007/s00382-011-1228-5>
- Hertwig E, Lunkeit F, Fraedrich K (2015) Low-frequency climate variability of an aquaplanet. *Theor Appl Climatol* 121(3):459–478, DOI <https://doi.org/10.1007/s00704-014-1226-8>
- Hoskins BJ, Simmons AJ (1975) A multi-layer spectral model and the semi-implicit method. *Q J R Meteorol Soc* 101(429):637–655, DOI <https://doi.org/10.1002/qj.49710142918>
- Hourdin F, Mauritsen T, Gettelman A, Golaz JC, Balaji V, Duan Q, Folini D, Ji D, Klocke D, Qian Y, Rauser F, Rio C, Tomassini L, Watanabe M, Williamson D (2017) The Art and Science of Climate Model Tuning. *Bull Am Meteorol Soc* 98(3):589–602, DOI <https://doi.org/10.1175/BAMS-D-15-00135.1>
- Hurrell JW, Kushnir Y, Ottersen G, Visbeck M (2003) An Overview of the North Atlantic Oscillation. In: *The North Atlantic Oscillation: Climatic Significance and Environmental Impact*, American Geophysical Union (AGU), pp 1–35, DOI <https://doi.org/10.1029/134GM01>
- Hyder P, Edwards JM, Allan RP, Hewitt HT, Bracegirdle TJ, Gregory JM, Wood RA, Meijers AJS, Mulcahy J, Field P, Furtado K, Bodas-Salcedo A, Williams KD, Copsey D, Josey SA, Liu C, Roberts CD, Sanchez C, Ridley J, Thorpe L, Hardiman SC, Mayer M, Berry DI, Belcher SE (2018) Critical Southern Ocean climate model biases traced to atmospheric model cloud errors. *Nat Commun* 9(1):3625, DOI <https://doi.org/10.1038/s41467-018-05634-2>

- IPCC (2013) *Climate Change 2013: The Physical Science Basis. Contribution of Working Group I to the Fifth Assessment Report of the Intergovernmental Panel on Climate Change* [Stocker TF, Qin D, Plattner GK, Tignor M, Allen SK, Boschung J, Nauels A, Xia Y, Bex V, Midgley PM (eds.)]. Cambridge University Press, Cambridge, United Kingdom and New York, NY, USA, DOI <https://doi.org/10.1017/CBO9781107415324>
- Jiang W, Gastineau G, Codron F (2021) Multicentennial Variability Driven by Salinity Exchanges Between the Atlantic and the Arctic Ocean in a Coupled Climate Model. *J Adv Model Earth Syst* 13(3):e2020MS002366, DOI <https://doi.org/10.1029/2020MS002366>
- Jungclauss JH, Haak H, Latif M, Mikolajewicz U (2005) Arctic–North Atlantic Interactions and Multidecadal Variability of the Meridional Overturning Circulation. *J Clim* 18(19):4013–4031, DOI <https://doi.org/10.1175/JCLI3462.1>
- Kalnay E, Kanamitsu M, Kistler R, Collins W, Deaven D, Gandin L, Iredell M, Saha S, White G, Woollen J, Zhu Y, Chelliah M, Ebisuzaki W, Higgins W, Janowiak J, Mo KC, Ropelewski C, Wang J, Leetmaa A, Reynolds R, Jenne R, Joseph D (1996) The NCEP/NCAR 40-Year Reanalysis Project. *Bull Amer Meteor* 77(3):437–472, DOI [https://doi.org/10.1175/1520-0477\(1996\)077<0437:TNYRP>2.0.CO;2](https://doi.org/10.1175/1520-0477(1996)077<0437:TNYRP>2.0.CO;2)
- Kilic C, Raible C, Stocker T (2017) Multiple Climate States of Habitable Exoplanets: The Role of Obliquity and Irradiance. *Astrophys J* 844:147, DOI <https://doi.org/10.3847/1538-4357/aa7a03>
- Knutti R, Flüelicker J, Stocker T, Timmermann A (2004) Strong hemispheric coupling of glacial climate through freshwater discharge and ocean circulation. *Nature* 430(7002):851–856, DOI <https://doi.org/10.1038/nature02786>
- Kuo HL (1974) Further Studies of the Parameterization of the Influence of Cumulus Convection on Large-Scale Flow. *J Atmos Sci* 31(5):1232–1240, DOI [https://doi.org/10.1175/1520-0469\(1974\)031<1232:FSOTPO>2.0.CO;2](https://doi.org/10.1175/1520-0469(1974)031<1232:FSOTPO>2.0.CO;2)
- Lacis AA, Hansen J (1974) A Parameterization for the Absorption of Solar Radiation in the Earth’s Atmosphere. *J Atmos Sci* 31(1):118–133, DOI [https://doi.org/10.1175/1520-0469\(1974\)031<0118:APFTAO>2.0.CO;2](https://doi.org/10.1175/1520-0469(1974)031<0118:APFTAO>2.0.CO;2)
- Lenton TM, Myerscough RJ, Marsh R, Livina VN, Price AR, Cox SJ, null n (2009) Using GENIE to study a tipping point in the climate system. *Philos Trans A Math Phys Eng Sci* 367(1890):871–884, DOI <https://doi.org/10.1098/rsta.2008.0171>

- Loeb NG, Doelling DR, Wang H, Su W, Nguyen C, Corbett JG, Liang L, Mitrescu C, Rose FG, Kato S (2018) Clouds and the Earth's Radiant Energy System (CERES) Energy Balanced and Filled (EBAF) Top-of-Atmosphere (TOA) Edition-4.0 Data Product. *J Clim* 31(2):895–918, DOI <https://doi.org/10.1175/JCLI-D-17-0208.1>
- Lorenz S (2006) Coupling of Planet Simulator (atmosphere) with Large Scale Geostrophic (ocean) general circulation model: PlaSim/LSG, Internal Report, Theoretische Meteorologie, University of Hamburg
- Lunkeit F, Borth H, Böttinger M, Fraedrich K, Jansen H, Kirk E, Kleidon A, Luksch U, Paiewonsky P, Schubert S, Sielmann F, Wan H (2011) Planet Simulator Reference Manual Version 16, Technical Report, Meteorologisches Institut, University of Hamburg. URL <https://www.mi.uni-hamburg.de/en/arbeitsgruppen/theoretische-meteorologie/modelle/sources/psreferencemanual-1.pdf>
- Lyu G, Köhl A, Matei I, Stammer D (2018) Adjoint-Based Climate Model Tuning: Application to the Planet Simulator. *J Adv Model Earth Syst* 10(1):207–222, DOI <https://doi.org/10.1002/2017MS001194>
- Madec G, Team NS (2012) Nemo ocean engine (27), DOI <https://doi.org/10.5281/zenodo.1464816>
- Maier-Reimer E, Mikolajewicz U (1992) The Hamburg Large Scale Geostrophic Ocean General Circulation Model, World Data Center for Climate (WDCC) at DKRZ DOI https://doi.org/10.2312/WDCC/DKRZ_Report_No02
- Maier-Reimer E, Mikolajewicz U, Hasselmann K (1993) Mean Circulation of the Hamburg LSG OGCM and Its Sensitivity to the Thermohaline Surface Forcing. *J Phys Oceanogr* 23(4):731–757, DOI [https://doi.org/10.1175/1520-0485\(1993\)023<0731:MCOTHL>2.0.CO;2](https://doi.org/10.1175/1520-0485(1993)023<0731:MCOTHL>2.0.CO;2)
- Mauritsen T, Stevens B, Roeckner E, Crueger T, Esch M, Giorgetta M, Haak H, Jungclaus J, Klocke D, Matei D, Mikolajewicz U, Notz D, Pincus R, Schmidt H, Tomassini L (2012) Tuning the climate of a global model. *J Adv Model Earth Syst* 4(3), DOI <https://doi.org/10.1029/2012MS000154>
- Mcguffie K, Henderson-Sellers A (2014) *The Climate Modelling Primer* fourth edition
- Meehl GA, Senior CA, Eyring V, Flato G, Lamarque JF, Stouffer RJ, Taylor KE, Schlund M (2020) Context for interpreting equilibrium climate sensitivity and transient climate response from the CMIP6 Earth system models. *Sci Adv* 6(26):eaba1981, DOI <https://doi.org/10.1126/sciadv.aba1981>

- Mezzina B, García-Serrano J, Bladé I, Kucharski F (2020) Dynamics of the ENSO Teleconnection and NAO Variability in the North Atlantic–European Late Winter. *J Clim* 33, DOI <https://doi.org/10.1175/JCLI-D-19-0192.1>
- Mezzina B, García-Serrano J, Bladé I, Palmeiro FM, Batté L, Ardilouze C, Benassi M, Gualdi S (2021) Multi-model assessment of the late-winter extra-tropical response to El Niño and La Niña. *Clim Dyn* DOI <https://doi.org/10.1007/s00382-020-05415-y>
- Micheels A, Montenari M (2008) A snowball Earth versus a slushball Earth: Results from Neoproterozoic climate modeling sensitivity experiments. *Geosphere* 4(2):401–410, DOI <https://doi.org/10.1130/GES00098.1>
- Mikolajewicz U, Maier-Reimer E (1990) Internal secular variability in an ocean general circulation model. *Clim Dyn* 4(3):145–156, DOI <https://doi.org/10.1007/BF00209518>
- Morice CP, Kennedy JJ, Rayner NA, Jones PD (2012) Quantifying uncertainties in global and regional temperature change using an ensemble of observational estimates: The HadCRUT4 data set. *J Geophys Res Atmos* 117(D8), DOI <https://doi.org/10.1029/2011JD017187>
- Murante G, Provenzale A, Vladilo G, Taffoni G, Silva L, Palazzi E, Hardenberg Jv, Maris M, Londero E, Knapic C, Zorba S (2020) Climate bistability of Earth-like exoplanets. *Mon Notices Royal Astron Soc* 492(2):2638–2650, DOI <https://doi.org/10.1093/mnras/stz3529>
- Myhre G, Highwood EJ, Shine KP, Stordal F (1998) New estimates of radiative forcing due to well mixed greenhouse gases. *Geophys Res Lett* 25(14):2715–2718, DOI <https://doi.org/10.1029/98GL01908>
- Orszag SA (1970) Transform Method for the Calculation of Vector-Coupled Sums: Application to the Spectral Form of the Vorticity Equation. *J Atmos Sci* 27:890–895, DOI [https://doi.org/10.1175/1520-0469\(1970\)027<0890:TMFTCO>2.0.CO;2](https://doi.org/10.1175/1520-0469(1970)027<0890:TMFTCO>2.0.CO;2)
- Park W, Latif M (2008) Multidecadal and Multicentennial Variability of the Meridional Overturning Circulation. *Geophys Res Lett* 35, DOI <https://doi.org/10.1029/2008GL035779>
- Peltier W, Vettoretti G (2014) Dansgaard-Oeschger Oscillations Predicted in a Comprehensive Model of Glacial Climate: A “Kicked” Salt Oscillator in the Atlantic. *Geophys Res Lett* 41, DOI <https://doi.org/10.1002/2014GL061413>

- Pfister PL, Stocker TF (2017) State-Dependence of the Climate Sensitivity in Earth System Models of Intermediate Complexity. *Geophys Res Lett* 44(20):10,643–10,653, DOI <https://doi.org/10.1002/2017GL075457>
- Pierce DW, Barnett TP, Mikolajewicz U (1995) Competing Roles of Heat and Freshwater Flux in Forcing Thermohaline Oscillations. *J Phys Oceanogr* 25(9):2046–2064, DOI [https://doi.org/10.1175/1520-0485\(1995\)025<2046:CROHAF>2.0.CO;2](https://doi.org/10.1175/1520-0485(1995)025<2046:CROHAF>2.0.CO;2)
- Poli P, Hersbach H, Dee DP, Berrisford P, Simmons AJ, Vitart F, Laloyaux P, Tan DGH, Peubey C, Thépaut JN, Trémolet Y, Hólm EV, Bonavita M, Isaksen I, Fisher M (2016) ERA-20C: An Atmospheric Reanalysis of the Twentieth Century. *J Clim* 29(11):4083–4097, DOI <https://doi.org/10.1175/JCLI-D-15-0556.1>
- Ragone F, Lucarini V, Lunkeit F (2016) A new framework for climate sensitivity and prediction: a modelling perspective. *Clim Dyn* 46(5):1459–1471, DOI <https://doi.org/10.1007/s00382-015-2657-3>
- Rahmstorf S, Crucifix M, Ganopolski A, Goosse H, Kamenkovich I, Knutti R, Lohmann G, Marsh R, Mysak LA, Wang Z, Weaver AJ (2005) Thermohaline circulation hysteresis: A model intercomparison. *Geophys Res Lett* 32(23), DOI <https://doi.org/10.1029/2005GL023655>
- Rahmstorf S, Box JE, Feulner G, Mann ME, Robinson A, Rutherford S, Schaffernicht EJ (2015) Exceptional twentieth-century slowdown in Atlantic Ocean overturning circulation. *Nat Clim Change* 5(5):475–480, DOI <https://doi.org/10.1038/nclimate2554>
- Rayner NA, Parker DE, Horton EB, Folland CK, Alexander LV, Rowell DP, Kent EC, Kaplan A (2003) Global analyses of sea surface temperature, sea ice, and night marine air temperature since the late nineteenth century. *J Geophys Res* 108(D14), DOI <https://doi.org/10.1029/2002JD002670>
- Rechid D, Raddatz TJ, Jacob D (2009) Parameterization of snow-free land surface albedo as a function of vegetation phenology based on MODIS data and applied in climate modelling. *Theor Appl Climatol* 95(3):245–255, DOI <https://doi.org/10.1007/s00704-008-0003-y>
- Robert A (1981) A stable numerical integration scheme for the primitive meteorological equations. *Atmos Ocean* 19(1):35–46, DOI <https://doi.org/10.1080/07055900.1981.9649098>
- Robson J, Hodson D, Hawkins E, Sutton R (2014) Atlantic overturning in decline? *Nat Geosci* 7(1):2–3, DOI <https://doi.org/10.1038/ngeo2050>

- Roeckner E, Arpe K, Bengtsson L, Duemenil L, Esch M, Brinkop S, Ponater M, Sausen R, Kirk E, Lunkeit F, Schubert S, Windelband M, Rockel B, Schlese U (1992) Simulation of the present-day climate with the ECHAM model: Impact of model physics and resolution, Technical Report 93, Max Planck Institute for Meteorology, Hamburg URL <http://centaur.reading.ac.uk/31839/>
- Roscher M, Stordal F, Svensen H (2011) The effect of global warming and global cooling on the distribution of the latest Permian climate zones. *Palaeogeogr Palaeoclimatol Palaeoecol* 309(3):186–200, DOI <https://doi.org/10.1016/j.palaeo.2011.05.042>
- Sasamori T (1968) The Radiative Cooling Calculation for Application to General Circulation Experiments. *J Appl Meteor* 7(5):721–729, DOI [https://doi.org/10.1175/1520-0450\(1968\)007<0721:TRCCFA>2.0.CO;2](https://doi.org/10.1175/1520-0450(1968)007<0721:TRCCFA>2.0.CO;2)
- Schneider DP, Reusch DB (2016) Antarctic and Southern Ocean Surface Temperatures in CMIP5 Models in the Context of the Surface Energy Budget. *J Clim* 29(5):1689–1716, DOI <https://doi.org/10.1175/JCLI-D-15-0429.1>
- Sciascia R (2008) Un modello a complessità intermedia per la circolazione oceanica globale, Dissertation, University of Turin
- Segschneider J, Grieger B, Keller H, Lunkeit F, Kirk E, Fraedrich K, Rodin A, Greve R (2005) Response of the intermediate complexity Mars Climate Simulator to different obliquity angles. *Planet Space Sci* 53:659–670, DOI <https://doi.org/10.1016/j.pss.2004.10.003>
- Semtner AJ Jr (1976) A Model for the Thermodynamic Growth of Sea Ice in Numerical Investigations of Climate. *J Phys Oceanogr* 6:379–389, DOI [https://doi.org/10.1175/1520-0485\(1976\)006<0379:AMFTTG>2.0.CO;2](https://doi.org/10.1175/1520-0485(1976)006<0379:AMFTTG>2.0.CO;2)
- Simmons AJ, Hoskins BJ, Burridge DM (1978) Stability of the Semi-Implicit Method of Time Integration. *Mon We Rev* 106(3):405–412, DOI [https://doi.org/10.1175/1520-0493\(1978\)106<0405:SOTSIM>2.0.CO;2](https://doi.org/10.1175/1520-0493(1978)106<0405:SOTSIM>2.0.CO;2)
- Slingo A, Slingo JM (1991) Response of the National Center for Atmospheric Research community climate model to improvements in the representation of clouds. *J Geophys Res* 96(D8):15341–15357, DOI <https://doi.org/10.1029/91JD00930>
- Solomon S, Hegerl GC, Heimann M, Hewitson B, Hoskins BJ, Joos F, Jouzel J, Kattsov V, Lohmann U, Matsuno T, Molina M, Qin D, Nicholls N, Qin D, Raga G, Ramaswamy V, Ren J, Rusticucci M, Somerville R, Stocker TF, Stouffer RJ, Whetton P, Manning M, Wood RA, Wratt D, Alley RB, Berntsen T, Bindoff NL, Chen Z, Chidthaisong A, Gregory JM (2007) Technical summary. Cambridge University Press, New York, pp 19–91, num Pages: 71

- Srokosz M, Baringer M, Bryden H, Cunningham S, Delworth T, Lozier S, Marotzke J, Sutton R (2012) Past, Present, and Future Changes in the Atlantic Meridional Overturning Circulation. *Bull Am Meteorol Soc* 93(11):1663–1676, DOI <https://doi.org/10.1175/BAMS-D-11-00151.1>
- Stephens GL (1984) The Parameterization of Radiation for Numerical Weather Prediction and Climate Models. *Mon Wea Rev* 112(4):826–867, DOI [https://doi.org/10.1175/1520-0493\(1984\)112<0826:TPORFN>2.0.CO;2](https://doi.org/10.1175/1520-0493(1984)112<0826:TPORFN>2.0.CO;2)
- Stephens GL, Ackerman S, Smith EA (1984) A Shortwave Parameterization Revised to Improve Cloud Absorption. *J Atmos Sci* 41(4):687–690, DOI [https://doi.org/10.1175/1520-0469\(1984\)041<0687:ASPRTI>2.0.CO;2](https://doi.org/10.1175/1520-0469(1984)041<0687:ASPRTI>2.0.CO;2)
- Stephens GL, Li J, Wild M, Clayson CA, Loeb N, Kato S, L'Ecuyer T, Stackhouse PW, Lebsock M, Andrews T (2012) An update on Earth's energy balance in light of the latest global observations. *Nat Geosci* 5(10):691–696, DOI <https://doi.org/10.1038/ngeo1580>
- Taylor K, Williamson D, Zwiers F (2000) The sea surface temperature and sea ice concentration boundary conditions for AMIP II simulations, PCMDI Report 60, Program for Climate Model Diagnosis and Intercomparison, Lawrence Livermore National Laboratory 60, URL <https://pcmdi.llnl.gov/report/pdf/60.pdf>
- Tibaldi S, Geleyn JF (1981) The production of a new orography, land-sea mask and associated climatological surface fields for operational purpose, ECMWF Technical Memorandum 40. DOI <https://doi.org/10.21957/p68g6dnfz>
- Titchner HA, Rayner NA (2014) The Met Office Hadley Centre sea ice and sea surface temperature data set, version 2: 1. Sea ice concentrations. *J Geophys Res Atmos* 119(6):2864–2889, DOI <https://doi.org/10.1002/2013JD020316>
- Vallis G (2011) *Climate and the Oceans*. DOI <https://doi.org/10.1515/9781400840625>
- Vellinga M, Wu P (2004) Low-Latitude Freshwater Influence on Centennial Variability of the Atlantic Thermohaline Circulation. *J Clim* 17(23):4498–4511, DOI <https://doi.org/10.1175/3219.1>
- Vettoretti G, Peltier WR (2018) Fast Physics and Slow Physics in the Nonlinear Dansgaard–Oeschger Relaxation Oscillation. *J Clim* 31(9):3423–3449, DOI <https://doi.org/10.1175/JCLI-D-17-0559.1>

- Voltaire A, Saint-Martin D, Sénési S, Decharme B, Alias A, Chevallier M, Colin J, Guérémy JF, Michou M, Moine MP, Nabat P, Roehrig R, Méliá DSy, Sférian R, Valcke S, Beau I, Belamari S, Berthet S, Cassou C, Cattiaux J, Deshayes J, Douville H, Ethé C, Franchistéguy L, Geoffroy O, Lévy C, Madec G, Meurdesoif Y, Msadek R, Ribes A, Sanchez-Gomez E, Terray L, Waldman R (2019) Evaluation of CMIP6 DECK Experiments With CNRM-CM6-1. *J Adv Model Earth Sy* 11(7):2177–2213, DOI <https://doi.org/10.1029/2019MS001683>
- Weber S (2010) The utility of Earth system Models of Intermediate Complexity (EMICs). *Wiley Interdiscip Rev Clim Change* 1, DOI <https://doi.org/10.1002/wcc.24>
- Winton M, Sarachik ES (1993) Thermohaline Oscillations Induced by Strong Steady Salinity Forcing of Ocean General Circulation Models. *J Phys Oceanogr* 23(7), DOI [https://doi.org/10.1175/1520-0485\(1993\)023<1389:TOIBSS>2.0.CO;2](https://doi.org/10.1175/1520-0485(1993)023<1389:TOIBSS>2.0.CO;2)
- Wyser K, van Noije T, Yang S, von Hardenberg J, O'Donnell D, Döscher R (2020) On the increased climate sensitivity in the EC-Earth model from CMIP5 to CMIP6. *Geosci Model Dev* 13(8):3465–3474, DOI <https://doi.org/10.5194/gmd-13-3465-2020>
- Zelinka MD, Myers TA, McCoy DT, Po-Chedley S, Caldwell PM, Ceppi P, Klein SA, Taylor KE (2020) Causes of Higher Climate Sensitivity in CMIP6 Models. *Geophys Res Lett* 47(1):e2019GL085782, DOI <https://doi.org/10.1029/2019GL085782>
- Zickfeld K, Eby M, Naughten K, Weaver A, Cressin E, Fichefet T, Goosse H, Philippon-Berthier G, Edwards N, Holden P, Eliseev A, Mokhov I, Feulner G, Kienert H, Perrette M, Deimling T, Forest C, Friedlingstein P, Joos F, Zhao F (2013) Long-Term Climate Change Commitment and Reversibility: An EMIC Intercomparison. *J Clim* 26:5782–5809, DOI <https://doi.org/10.1175/JCLI-D-12-00584.1>